MULTILAYER THIN FILMS: SOL-GEL ROUTES TO ONE-DIMENSIONAL PHOTONIC AND MAGNONIC CRYSTALS

by

Michael Raymond Dahlby

A dissertation submitted to the faculty of
The University of Utah
in partial fulfillment of the requirements for the degree of

Doctor of Philosophy

Department of Chemistry

The University of Utah

December 2015

The University of Utah Graduate School

STATEMENT OF DISSERTATION APPROVAL

The dissertation of **Michael Raymond Dahlby**

has been approved by the following supervisory committee members:

Michael H. Bartl	, Chair	**May 14, 2015** Date Approved
Michael D. Morse	, Member	**May 14, 2015** Date Approved
Thanh Truong	, Member	**May 14, 2015** Date Approved
Ilya Y. Zharov	, Member	**May 14, 2015** Date Approved
Ajay Nahata	, Member	**May 14, 2015** Date Approved

and by **Cynthia J. Burrows**, Chair of

the Department of **Chemistry**

and by David B. Kieda, Dean of The Graduate School.

ABSTRACT

An in-depth analysis of the 4-step sol-gel deposition process for thin films consisting of 1) dip-coating 2) rapid solvent evaporation 3) brief thermal treatment and 4) shock-cooling was performed. Bragg stacks consisting of alternating silica and titania layers were prepared and the versatility of the process was exhibited by preparing samples of varying layer thickness with reflection bands spanning the entire visible range. Post-synthetic thermal annealing was found to increase the crystallinity of the titania films while resulting in a blue-shift of the main reflection peak due to titania layer shrinkage.

The photo-stability of these Bragg stacks was investigated by laser-induced damage threshold studies. Results obtained by optical microscopy, reflectance spectroscopy, and SEM imaging showed that Bragg stacks annealed at higher temperatures exhibit a decrease in damage threshold as a result of increased interlayer stress, suggesting that interfacial properties rather than the quality of individual layers are more important for determining stability of Bragg stacks under intense laser irradiation. This is an important result, as it shows that it is beneficial to forego the final thermal annealing step often employed when fabricating Bragg stacks, leading to a decrease in overall energy cost and an increase in throughput for the synthesis of Bragg-type optical components.

A new “additive-free” sol-gel technique featuring simple reactants and reactant conditions was developed to deposit various iron-based oxide films on silicon and quartz substrates. The reactant concentrations were carefully tuned to control the hydrolysis and

condensation rates of iron salts to synthesize a homogeneous iron oxide sol. Single-phase films including α-Fe_2O_3, YIG, $CoFe_2O_4$, and $NiFe_2O_4$ were obtained after thermal annealing and exhibited a high level of crystallinity by XRD analysis. The magnetic properties were investigated by VSM and showed very good magnetic ordering. The thickness of the deposited films was tuned by adjusting the precursor and reactant concentrations as well as repeating the deposition cycle using the same solution. Composition analysis was performed by XPS and confirmed the oxidation states and ratios of ions present in the films were in excellent agreement with the expected results.

For my grandmother, Mary Alice Meierotto.

TABLE OF CONTENTS

LIST OF FIGURES

Figure

ACKNOWLEDGEMENTS

The first thank you belongs to my advisor, Dr. Michael Bartl. I am very grateful that I was fortunate enough to be a member of Mike's group. It was evident early on during my time here that Mike is very dedicated to the success and well-being of his students. When times were tough, he was full of encouragement, insight, and advice. I have learned a lot of science during my time here, but I have also learned a lot about what it means to be a mentor.

I am also fortunate to have had a committee that always seemed interested in promoting my growth as a scientist. I would like to thank Dr. Michael Morse, Dr. Ajay Nahata, Dr. Thanh Truong, and Dr. Ilya Zharov for being demanding but fair, and encouraging me to seek greater understanding of my studies. I am especially grateful to Ilya for his guidance while Mike was on leave.

There are several people to whom I owe a huge thank you for helping me directly in performing the work to complete my dissertation, including Moussa Barhoum, Wendy Consoer, Zack Richens, Carlos Burga, Trevor Hull, Golda Hukic-Markosian, Alonzo Martinez, Dan Matthew, Ryan McLaughlin, and Andrew Simonson. All of you provided much needed assistance and I am grateful for your contributions.

I would also like to acknowledge the support staff in the department, including Jo Hoovey, who always provided a smile and words of encouragement, and Jay Ingleby and Nomi Stout who were always happy to stop and chat awhile.

I am grateful for all of the friends I have gained during my time here, including Andrew Simonson, Ashley Dunn, Dan Matthew, Eric Johnson, and Ryan Dain. Many outings consisting of bowling, hiking, and pub quizzes will always be remembered fondly for providing much needed relief and adventure.

Naturally, nobody deserves a bigger thank you than my family, especially my mom Cathy, brother Paul, and grandparents Jim and Mary Alice. It was hard moving half way across the country, but their love and support allowed me to pursue this opportunity and I could not have done it without them. I would also like to thank my uncle Ray, who helped foster my love of mountains by encouraging me to go on a ski trip back in my first year of college. Last, but certainly not least, I am most appreciative of my wife Erin for her patience and support during the many trials and tribulations of a graduate student. It is humbling to think about the serendipitous circumstance in which we met and I am forever grateful that you decided to give me a chance.

CHAPTER 1

INTRODUCTION

The overall goal of my dissertation is to build a foundation that will allow future scientists to synthesize a number of high-quality dielectric and magnetic thin films using a simple, solution-based sol-gel technique. The availability of fast and versatile methods to fabricate a wide variety of materials consisting of varying architectures and compositions will allow future endeavors to be limited by the imagination rather than the limits imposed by a particular deposition technique. The progress towards this goal will be demonstrated by the rapid, tunable fabrication of Bragg stacks, or one-dimensional (1D) photonic crystals (PCs), as well as several magnetic oxide films that will lead toward the same fabrication of a 1D magnonic crystal (MC) (**Figure 1.1**). The methods and materials developed in my doctoral studies have potential applications in the areas of photonics, magnonics, spintronics, and magneto-optics.

This first chapter will present all of the background information necessary to understand the content of my work, beginning with a description of what a thin film is, some common vapor-based fabrication techniques, and why sol-gel chemistry is a viable alternative. Then a description of the sol-gel process will be presented, beginning with a discussion of the chemical reactions involved and the film formation process. The next section will discuss the behavior of electromagnetic waves in periodic dielectric media,

including the quantum and classical descriptions of a 1D PC.

Here, the course of discussion will shift to the topic of MCs. This will begin with a discussion of the different types and origins of magnetism. Then, parallels will be drawn between photonic crystals and magnonic crystals and a brief introduction to the idea of propagating spin waves in magnetic materials will be presented.

The last section will consist of an overview of the remaining chapters of my dissertation.

Thin Films

Thin film is a term used to define a layer of material much thinner than the substrate on which it is deposited. In some cases, a thin film may consist of a single layer of atoms with a thickness of several angstroms, while other films may measure several microns. Regardless, it is nearly impossible to overstate the impact that thin film applications have had on today's society. Conducting, semiconducting, and insulating films are vital components in electronic devices[1-10]. Dielectric films have many applications in optics including reflective and antireflective coatings[11-13] and filters[14-16]. Magnetic thin films are often found in memory storage devices[17-18]. Chemically inert films can be used as protective coatings[19-21] to prevent oxidation and corrosion while mechanically robust films can be used as protection against abrasion and friction[22-24].

This plethora of applications stems from the incredibly diverse number of materials that exhibit unique properties in thin film form when compared to the same material in bulk. As well as the wide array of methods available for depositing thin films[25-32].

Vapor Deposition Methods

Vapor deposition techniques, including atomic layer deposition (ALD)[33-34], molecular beam epitaxy (MBE)[35-36], pulsed laser deposition (PLD)[37-38], chemical vapor deposition (CVD)[39-40], and sputtering[41], are the most common methods of thin film deposition in use today. Vapor deposition was first observed in the 1850s as the result of glow discharge.[42] However, it was not until the advent of high-vacuum systems in the 1960s that these techniques began to find widespread applications. High-vacuum is necessary for pure, uniform film deposition onto a substrate by vapor deposition techniques. Several advantages of these techniques include atomic-scale control over thickness, a vast number of elements and compounds that can be deposited, and high throughput in fabrication. These capabilities are necessary for large-scale production of devices that require atomic-level precision in order to function properly and consistently. However, some major disadvantages to these methods include the fact that the equipment required is complex, expensive, high-maintenance, and energy intensive.

Sol-Gel Chemistry

Sol-gel processing is an attractive alternative for the deposition of metal oxide thin films due to its simplicity, versatility, and mild synthetic conditions.[32,43-46]. The term sol-gel chemistry is typically used to describe any process where molecular precursors first form a sol, defined as a colloidal suspension of solid particles in a liquid, and then undergo a transformation to a gel, consisting of cross-linked particles. Sol-gel chemistry is a very versatile but also finicky technique that in some ways can be considered as much an art as a science. Choice of precursors, solution parameters, processing parameters, and post-

synthetic processes must be carefully tuned to synthesize a wide variety of materials, including films[43,47-53], fibers[54-58], powders[59-60], aero-/xerogels[61-63], and dense ceramics[64]. These may consist of a wide variety of compositions and length scales, from nanometer-sized particles to films with thicknesses on the micrometer scale to monoliths of centimeters in size.

The two choices of molecular precursors are metal alkoxides of the type M-OR where *M* is a metal atom and *R* is an organic group (methyl, ethyl, isopropyl, etc.) and metal salts (nitrate, chloride, etc.). Alkoxides are the more commonly used type of precursor[45]. These readily undergo hydrolysis reactions with water to form metal hydroxides[65-66]. For example, consider the case of the silica precursor used in this work, tetraethyl-orthosilicate (TEOS) in **Figure 1.2**. Nucleophilic substitution by water replaces the alkoxy group with a hydroxyl group, leaving an ethanol molecule as the byproduct. Since the precursor contains four ethoxy groups, it is considered tetrafunctional. (A functionality >2 is a requirement to form a three-dimensional gel network. Otherwise, only monomeric species or linear chains can be obtained.) Complete hydrolysis of TEOS with four water molecules would lead to the formation of a silicic acid molecule.

Once a precursor has hydrolyzed, it is able to undergo condensation with other precursor molecules to form an oxo-bridge (M – O – M). This can occur with other hydrolyzed moieties through an oxolation reaction, releasing water as a byproduct, or with unhydrolyzed ethoxy groups through an alcoxolation reaction, releasing ethanol as the byproduct. It is not necessary for a precursor to undergo complete hydrolysis before condensation takes place; in fact, they often occur concurrently. However, the process is always initiated by hydrolysis which leads to condensation of monomers to form dimeric

species. Continued condensation reactions then take place via oxolation and alcoxolation pathways to form nanometer-sized colloidal particles (a "sol").

Metal salt precursors can undergo analogous hydrolysis and condensation reactions[45,66-67]. Metal salts in pure aqueous solutions form complexes consisting of aquo (M-OH_2), hydroxo (M – OH), and oxo (M = O) ligands. In this context, hydrolysis is defined as the equilibria established when protons dissociate from ligated water molecules as a consequence of increased acidity due to charge transfer to the metal. The general formula for these precursors can be written as $[MO_NH_{2N-h}]^{(z-h)+}$ where N is the number of water molecules coordinated to the metal ion and h is the molar ratio of hydrolysis (i.e. how many protons have dissociated per water molecule). When $h = 0$ (no dissociation), the precursor is the aquo complex $[MO_NH_{2N}]^{z+}$ and for $h = 2N$ (complete dissociation), the precursor is the oxy complex $[MO_N]^{(2N-z)-}$. For values $0 < h < 2N$, the precursor is either an oxo-hydroxo complex ($h > N$), an aquo-hydroxo complex ($h < N$), or a hydroxo complex ($h = N$). Condensation reactions can occur after the formation of any hydroxo ligands and proceed by either oxolation or olation pathways, leading to oxo-bridges or hydroxy-bridges, respectively. As in the case for metal alkoxides, repeated condensation reactions lead to the formation of a sol. It should be mentioned that these reaction pathways are not limited to only pure aqueous solutions but are affected by the presence of any species that can compete for coordination to the metal ion.

After the formation of a sol, random cross-linking occurs between particles via condensation of unreacted hydroxyl groups in a process referred to as gelation, or aging. Depending on the kinetics and nature of reactivity between the particles, this process may yield a continuous, solid, three-dimensional network extending throughout the solution (a

"gel"). Alternatively, some conditions may lead to a situation where particle growth continues discretely rather than through cross-linking between particles. When this occurs unimpeded, large particles will precipitate out of solution. However, under controlled conditions, this can lead to the synthesis of monodispersed particles as in the Stöber process for silica nanospheres.[68]

The reactions involved in sol-gel processing consist of only these hydrolysis and condensation reactions. However, controlling the rates of these reactions is paramount to obtaining a desired material. The kinetics of these reactions vary significantly and are affected by a number of parameters including the nature of the metal ion, solvent, reactant concentrations, solution pH, and temperature. For example, silicon alkoxide precursors exhibit very slow rates of hydrolysis and condensation and usually require the presence of acid or base catalysts to proceed at room temperature. Titanium alkoxides, on the other hand, exhibit extremely fast and very exothermic reactions, and require significant precautions to slow down the reactions to a rate amenable to further processing techniques[69].

Additional post-synthetic processing techniques allow for conversion of the sol or gel into the desired shape or form[70]. For example, prior to gelation, fibers may be drawn from the sol, structures may be replicated through infiltration and subsequent condensation, and structure-directing agents may be added to form porous materials. After gel formation is complete, various solvent extraction processes can also lead to the formation of aerogels, xerogels, and dense powders. Lastly, thin films may be formed through spray-, spin-, or dip-coating.

The films discussed in subsequent chapters were prepared by dip-coating. At first glance, the dip-coating process may seem elementary. A substrate is lowered into a solution, or bath, and upon withdrawal, the components of the solution "stick" to the substrate. However, closer examination of the process reveals a number events that must occur in concert in order to yield a high-quality film (**Figure 1.3**)[51,71-73]. In fact, the quality and thickness of the obtained film is determined by a competition of up to six different forces[45]. The deposition process begins with the upward motion of the substrate, which creates a fluid mechanical boundary layer that carries a portion of the bath upward[45]. This boundary layer then splits, creating a division point where the outer portion of the boundary layer returns to the bath while the inner portion continues to rise with the substrate. Gravitational draining and vigorous solvent evaporation forces the initially dilute precursors into close proximity, resulting in a rapid increase in concentration. Subsequent aggregation and cross-linking of the particles increase the viscosity of the solution, leading to a porous, gel-like film. Further densification through continued evaporation, condensation, and pore collapse then give way to a solid film.

Wave Propagation in Dielectrics

Now that the sol-gel technique used to fabricate films in this dissertation has been explained, the topic of discussion will shift to electromagnetic wave propagation in 1D PCs, which are the subject matter for Chapters 2 and 3. To understand the unique features of these materials, it is important to first understand the nature of electromagnetic wave propagation in dielectric materials. In vacuum, electromagnetic waves travel at constant velocity *c*. In a dielectric material, the wave is slowed to a velocity *v* by a ratio called the

refractive index, n, where $n = c/v$. When a wave is incident on an interface between dielectrics with different refractive indices, a portion of the wave is transmitted into the new material while a portion of the wave is reflected. The portion of light that is reflected is given by equation (1.1).

$$R = \left(\frac{n_0 - n_1}{n_0 + n_1}\right)^2 \tag{1.1}$$

Here, n_0 is the refractive index of the originating medium and n_1 is the refractive index of the incident medium. (It should be noted that this equation only applies for light at normal incidence. For other angles, the $R_\parallel$ and $R_\perp$ components of the incoming light must be treated separately.) When the wave propagates from the lower index medium to the higher index medium, the reflected wave undergoes a phase change equal to π while no phase change is experienced when propagating from the high to low index medium.

Classical Description of Bragg Stacks

From this description, the behavior of light propagating through a Bragg stack may be considered as the sum of partial reflections at the many interfaces. The term "Bragg stack" was derived from an analogy of Bragg diffraction of x-rays due to the periodic lattice planes of atoms in a crystal lattice.

When the width of each bilayer is equal to $\lambda/2$, the wave reflected at the first interface will be in phase with the wave reflected at every other odd-numbered interface due to the phase shift, resulting in constructive interference. Given a sufficient number of bilayers, this constructive interference will lead to total reflectivity, which is often

estimated by equation (1.2)[74-75].

$$R = \left[\frac{n_0(n_2)^{2N} - n_s(n_1)^{2N}}{n_0(n_2)^{2N} + n_s(n_1)^{2N}}\right]^2 \quad (1.2)$$

Here, n_o, n_1, n_2, and n_s are the refractive indices of the original medium, the two dielectric materials, and the substrate, respectively, and N is the number of bilayers. This equation gives a very good estimate for calculating percent reflection of light at normal incidence of a Bragg stack consisting of materials with refractive indices smaller than 3.

Photonic Crystals

Even though the properties of Bragg stacks were first described in the 19th century, they have now become synonymous with 1D PCs after the theories of two-dimensional and three-dimensional (2D and 3D, respectively) photonic band gaps were proposed in two seminal papers published independently by Eli Yablonovitch[76] and Sajeev John[77] in 1987. A quantum description of PCs was developed by Joannopoulis and co-workers, and draws many parallels to the theory of semiconductors[78]. In fact, PCs are often nicknamed "semiconductors of light."[79-80] Where a semiconductor consists of a crystalline lattice of atoms, subjecting a propagating electron to a periodic variation of potential, a PC consists of a periodic arrangement of dielectric materials that subjects a propagating electromagnetic wave to a periodic variation in refractive index.

In some cases, the structure and properties of the periodic medium can prohibit the propagation of waves with a certain range of energies[81]. Semiconductors contain band gaps that prohibit electrons with certain energies from propagating. Similar behavior exists for

electromagnetic waves in a photonic crystal (PC)[82-88], acoustic waves in a phononic crystal[89-95], and spin waves in a magnonic crystal (MC)[96-104]. The explanation of this behavior begins with the Bloch theory of plane waves propagating through periodic media.

Wave Propagation in Periodic Media

The discovery of wave-like behavior of electrons (i.e. quantum mechanics) along with the Bloch theorem helped to describe the behavior of electrons in semiconductors. With the right symmetry, periodicity, and composition, plane waves can travel through periodic media without scattering. Such waves are called Bloch waves and are written in the form

$$\psi_{n\mathbf{k}}(\mathbf{r}) = e^{i\mathbf{k}\mathbf{r}} u_{\mathbf{k}}(\mathbf{r}) \tag{1.3}$$

where $\psi_{n\mathbf{k}}(\mathbf{r})$ is the Bloch wavefunction at position $\mathbf{r}$, $\mathbf{k}$ is the wavevector, n is the band index, $i = +\sqrt{-1}$, and $u(\mathbf{r})$ is a periodic function with the same periodicity as the propagating medium. This behavior allows for the calculation of a band diagram where for each wavevector $\mathbf{k}$ there exists an infinite set of modes with discretely spaced energies associated with $\psi_{n\mathbf{k}}$ and each band n is a set of functions $\psi_{n\mathbf{k}}$ that vary continuously with $\mathbf{k}$. If a gap exists between any two bands for a set of wavevectors, waves with energies that fall within that gap are not allowed to propagate through the medium and the medium is said to contain a band gap.

Quantum Description of PCs

Joannopoulos and co-workers developed a quantum description of the behavior of electromagnetic waves within a mixed, periodic dielectric medium that is very similar to the quantum description of electron behavior and allows for the calculation of the energies associated with the Bloch waves described above[105]. For their quantum description to hold true, the following assumptions have to be valid: 1) the electromagnetic intensities are weak so that nonlinear behavior of the dielectrics may be ignored; 2) the material is macroscopic and isotropic; 3) the dielectric constants are independent of the frequencies of interest; 4) the dielectrics are low-loss, meaning there is minimal absorption of the radiation. If these four assumptions are satisfied, the macroscopic Maxwell equations can be expressed as a linear Hermitian eigenvalue problem (analogous to the Schrodinger equation) involving only the magnetic field[106]. This yields the master equation given by equation (1.2).

$$\widehat{\Theta}\mathbf{H}(\mathbf{r}) = \left(\frac{\omega}{c}\right)^2 \mathbf{H}(\mathbf{r}) \tag{1.4}$$

Here, the eigenfunctions $\mathbf{H}(\mathbf{r})$ are the Bloch modes of the magnetic field as a function of the position (time independent) vector $\mathbf{r}$, the eigenvalues are equal to $(\omega / c)^2$ where ω is the frequency of the mode and c is the speed of light in vacuum, and the linear Hermitian operator $\widehat{\Theta}$ is defined as

$$\widehat{\Theta}\mathbf{H}(\mathbf{r}) \triangleq \nabla \times \left(\frac{1}{\varepsilon(\mathbf{r})} \nabla \times \mathbf{H}(\mathbf{r})\right) \tag{1.5}$$

where $\varepsilon(\mathbf{r})$ is the spatially dependent dielectric constant.

Equation (1.3) can be solved for a given structure of $\varepsilon(\mathbf{r})$ to find the modes $\mathbf{H}(\mathbf{r})$ and the corresponding frequencies. Then, the electronic modes can be obtained from equation (1.4).

$$\mathrm{E}(\mathbf{r}) = \frac{i}{\omega \varepsilon_0 \varepsilon(\mathbf{r})} \nabla \times \mathbf{H}(\mathbf{r}) \tag{1.6}$$

Here, $i = +\sqrt{-1}$ and ε_0 is the vacuum permittivity. This treatment, along with the variational principle and orthogonality requirement for successive modes, allows for the calculation of frequencies of the Bloch waves and the construction of band structures, or dispersion diagrams.

This treatment reveals some very convenient properties of PCs. For one, electromagnetic modes do not interact (unlike electron-electron repulsion in quantum mechanics), which allows for the master equation to be solved exactly.[106] Second, the solutions are not restricted to any certain length scale, meaning that solutions can easily be scaled up or down in length and frequency. These implications facilitate the design, characterization, and real-world application of PCs.

Physical Origin of Band Gap

Consider a 1D PC with a periodic dielectric function in the z direction and a lattice constant a so that $\varepsilon(\mathbf{r}) = \varepsilon(\mathbf{r} \pm a)$. The translational symmetry of the dielectric function allows treatment of electromagnetic waves propagating in the z-direction as Bloch waves with wavevectors $\mathbf{k}$ such that values of $\mathbf{k}$ that differ by multiples of $2\pi/a$ are identical.

Therefore, only values of **k** that fall within the 1D Brillouin zone with boundary values of $\pm \pi/a$ need to be considered.

In the case of a homogeneous dielectric function with artificial periodicity, the modes at the band edge $\mathbf{k} = \pi/a$ are degenerate (**Figure 1.4, left**) and can be written as sine and cosine functions with the same frequency. However, when a periodic dielectric medium is introduced, the modes at $\mathbf{k} = \pi/a$ have a wavelength of $2a$, twice that of the dielectric lattice constant. In this case, due to symmetry requirements, the modes must be centered in either the high-ε region or the low-ε region. The high-frequency mode becomes concentrated in the low-ε region while the low-frequency mode becomes concentrated in the high-ε region. This breaks the degeneracy and creates a band gap where there is no real solution for **k** that exists for the frequencies within the gap (**Figure 1.4, middle**). Increasing the dielectric contrast results in a wider gap (**Figure 1.4, right**).

Magnonic Crystals

Just as band-gap engineering can be performed using dielectric materials with contrasting refractive indices to create a PC, magnetic materials with contrasting magnetic properties (e.g. saturation magnetization) can be used to create a MC that prohibits the propagation of spin waves[107]. This discussion will begin with an explanation of the origin and different types of magnetism and conclude with a brief introduction to spin waves.

Magnetism

Magnetism is a property that stems from the motion of electrical charges. All forms of matter, then, are inherently magnetic due to the orbital motion and spin of electrons in

an atom. However, the manifestation of magnetic properties greatly depends on the chemical bonding and electron interactions of a material. The two basic types of magnetism are 1) induced magnetism, which manifests only in the presence of an applied field, and 2) spontaneous magnetism, which can exist without the presence of an applied field.

Induced magnetism, which includes diamagnetism and paramagnetism, arises from paired an unpaired electrons, respectively. Diamagnetism is the result of filled quantum states with paired spins and is the most basic from of magnetism. According to Lenz's law, diamagnetism manifests as a magnetic moment with a field that opposes the direction of the applied field. Paramagnetism is the result of an unpaired electron in an unfilled quantum state. Because the electron is unpaired, paramagnetism is a permanent form of magnetism; however, the spin states of the unpaired electrons show no interaction and therefore the moments are randomized by thermal motion until placed in an applied field with sufficient strength to overcome the randomization.

While many materials exhibit diamagnetism and paramagnetism, these are weak compared to spontaneous forms of magnetism, which are hallmarked by the presence of magnetization in the absence of an applied field. This phenomenon is due to exchange interactions that couple adjacent spin states and are quantum mechanical in nature. The type of interaction in a spontaneous magnet is dictated by the amount of orbital overlap in adjacent magnetic cations as well as the attractive and repulsive forces an electron experiences between adjacent nuclei and other electrons, respectively. These interactions can lead to direct, indirect, or super-exchange mechanisms. These coupling mechanisms then lead to ferromagnetic ordering, where adjacent spins are aligned in the same direction, or antiferromagnetic ordering, where adjacent spins are aligned in an antiparallel fashion.

For magnetic oxides, the magnetic cations are often too far apart for direct exchange to occur[108] and instead couple through superexchange with the oxygen dianion.

A special case of magnetism called ferrimagnetism occurs when materials such as the aptly-named ferrites, which are the subject of Chapter 4, consist of two interspersed sublattices that both align antiferromagnetically but the bulk material behaves ferromagnetically. This is due to the unequal magnitudes between the magnetic moments of the sublattices, resulting in a moment that is the net difference between them.

The magnetic properties of a material are often characterized through the collection and analysis of magnetic hysteresis curves. Various instruments and techniques for data collection exist and each can disclose different information about the sample, but generally speaking, the method of data collection is the same. An external magnet is used to vary the strength of an applied field and the response produced by the sample is measured. Important parameters can then be obtained from the different areas of the curve, including the saturation, remnance, and coercivity. The saturation magnetization (M_s) is the magnetization of the sample when the domains (collective areas where the individual magnetic moments are perfectly aligned) can align no further with the external field. The remnant magnetization (M_r) is the strength of the spontaneous magnetization of the sample in the absence of an applied field. The coercivity (H_c) is the strength of external field necessary to randomize the ordering of the domains. The squareness, S, of the curve is defined as $S = M_s/M_r$,. This is a unitless ratio used to communicate how well a sample maintains its magnetization.

Spin Waves

Magnonics is an expanding field involving the excitation, propagation, and application of spin waves (often interchangeably referred to as their unit of quantization – a magnon), which are propagating disturbances in the magnetic ordering of a material[81]. In a simple ferromagnet, the ground state has all spins aligned parallel (**Figure 1.5a**). One possible excited state is the case where one spin is reversed **Figure 1.5b**). However, the overall energy of the system can be lowered when the energy of this localized excitation is spread over several neighboring spins, resulting in slight deviations from the ground state orientation for each spin (**Figure 1.5c**). These disturbances can exhibit wave-like behavior as they propagate through the spin lattice as oscillations in the relative orientation of spins in a lattice (**Figure 1.5d and e**).

These structures have been demonstrated experimentally[98,101-102,104,109], but to date, the number of functioning examples is low and the techniques used to fabricate such MCs are cumbersome. Therefore, this area would benefit from new, efficient, and adaptable techniques to fabricate materials that will allow for the study of spin wave propagation to grow.

Dissertation Overview

Chapter 2 focuses on the optimization of the sol-gel shock-cooling technique developed in the Bartl lab. Each aspect of the process will be examined in detail, with an explanation of the necessity of each step, how it affects the overall deposition of films, and suggestions for tuning the technique for special circumstances. Because this process is amenable to the deposition of silica and titania (refractive indices of 1.5 and 2.2-2.8,

respectively), it is useful for preparing Bragg stacks. The effect of thermal annealing on the microstructure and optical properties of Bragg stacks prepared by this technique will be investigated.

A study of the photostability of thermally annealed Bragg stacks is presented in Chapter 3. Laser-induced damage threshold experiments were performed to investigate the initiation and growth of damage. The results for samples annealed at different temperatures will be compared.

Chapter 4 presents new synthesis methods for various magnetic oxide thin films. These films are prepared *via* a new "additive-free" approach and their structural and magnetic properties will be characterized. In particular, the fabrication of iron oxide, cobalt ferrite, nickel ferrite, manganese-iron oxide, and yttrium iron garnet films are described in detail. Furthermore, the challenges associated with sol-gel processing of the metal salt precursors are discussed. Film thicknesses are tuned by a combination of reactant concentration and deposition cycles and excellent magnetic properties are obtained after thermal annealing.

Finally, Chapter 5 will illustrate how magnetic films obtained by the technique presented in Chapter 4 could lead to the rapid fabrication of MC structures. In addition, suggestions for other applications of the films presented in this dissertation will be offered.

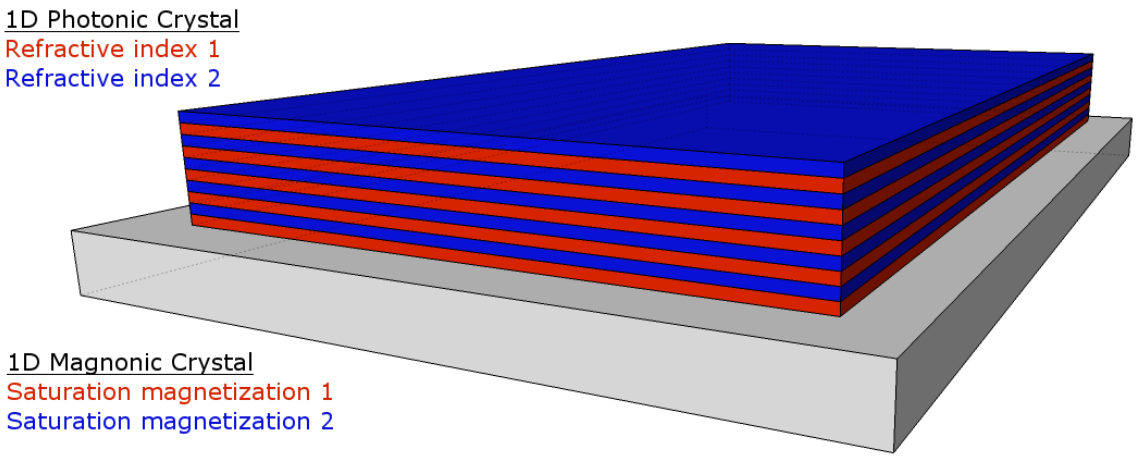

Figure 1.1 Schematic of 1D photonic crystal and magnonic crystal. In both cases, the properties of the material are homogeneous in either direction parallel to the plane of the film and alternate periodically in the direction perpendicular to the film.

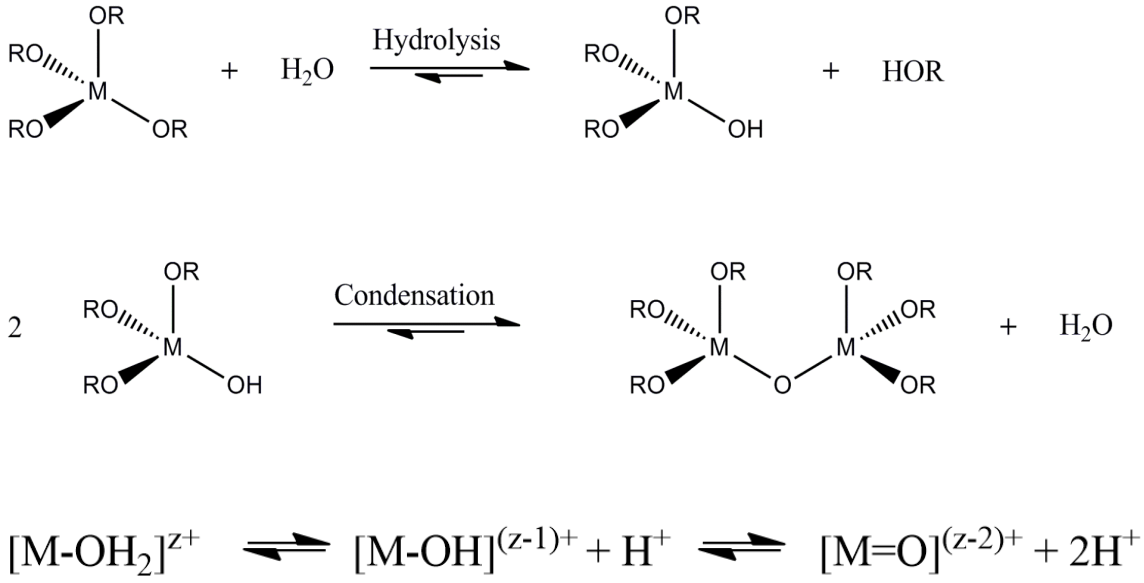

$$[M\text{-}OH_2]^{z+} \rightleftharpoons [M\text{-}OH]^{(z-1)+} + H^+ \rightleftharpoons [M{=}O]^{(z-2)+} + 2H^+$$

Figure 1.2 General reaction schemes for hydrolysis and condensation of metal alkoxides and hydrolysis of aqueous metal salts.

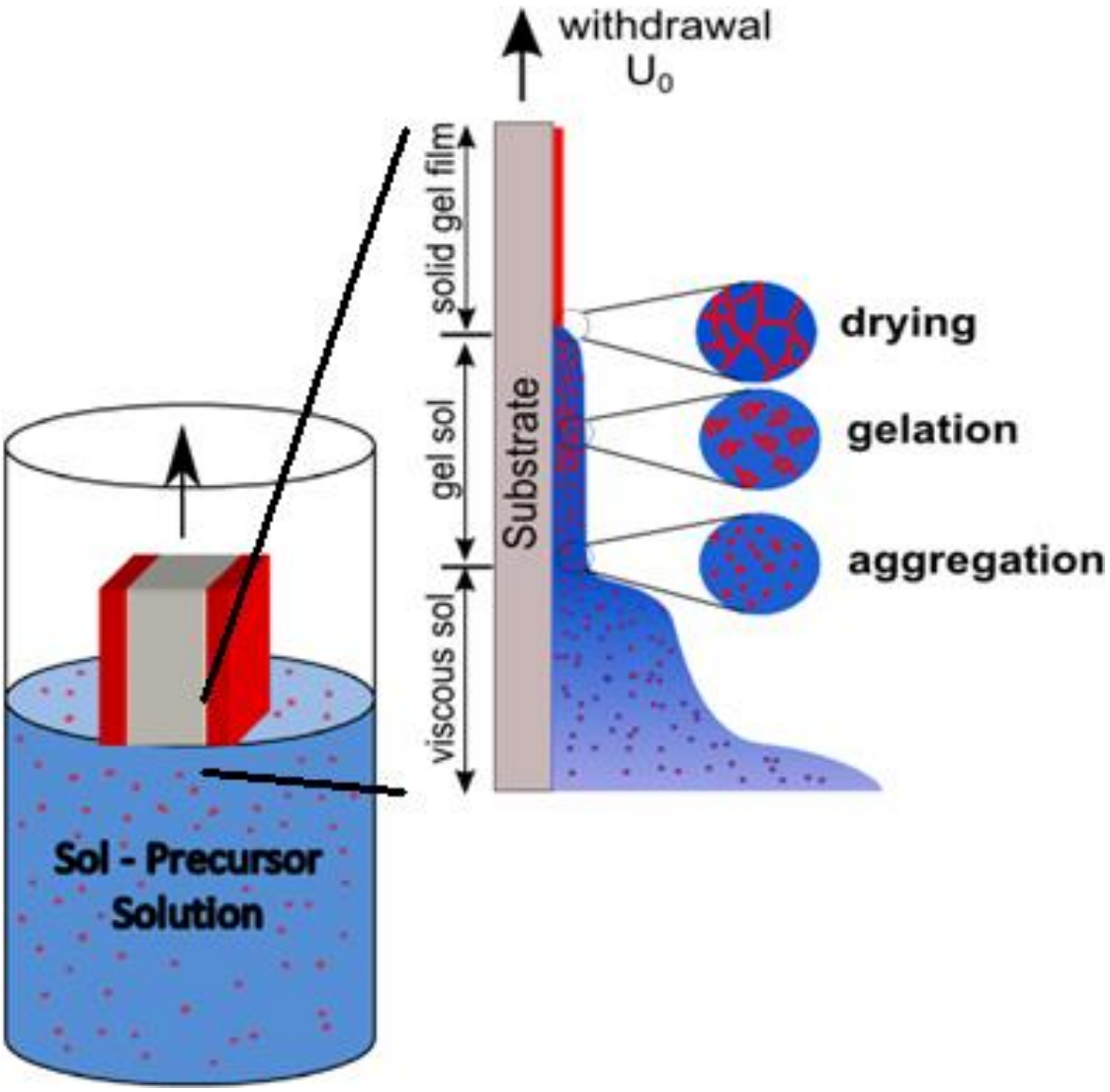

Figure 1.3 Schematic of the dip-coating process for a substrate being withdrawn at speed U_o. From Ref. [46].

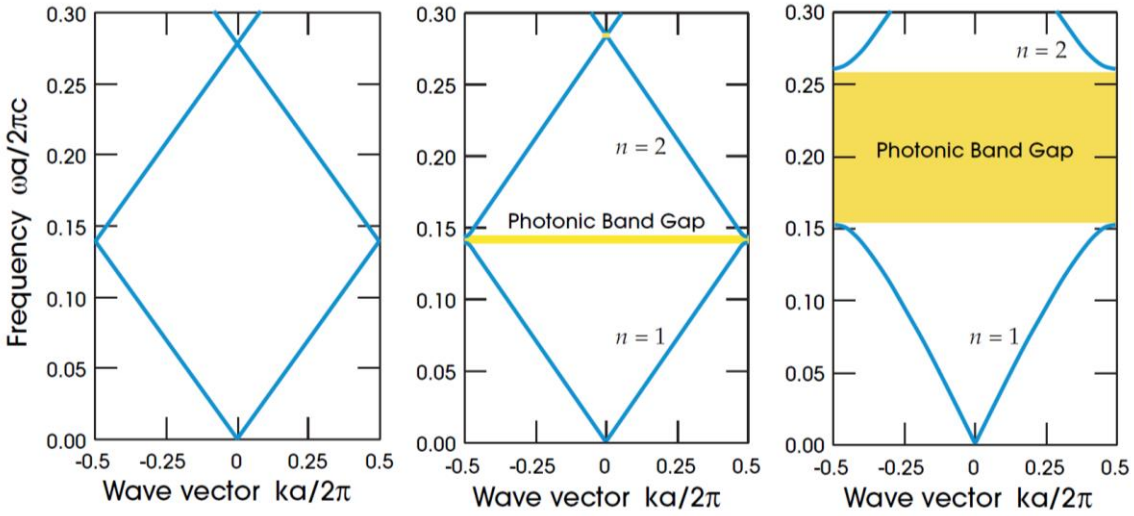

Figure 1.4 Calculated band diagrams for propagation in the direction of periodicity of a one-dimensional photonic crystal (PC) with layer thicknesses equal to half the wavelength. On the left, the PC consists of layers with the same dielectric constant. Note that the upper and lower bands are exactly equal at the band edge. In the middle, the layers have dielectric constants of 12 and 13. The small difference leads to a small band gap. On the right, the dielectric constants are 1 and 13, resulting in a much wider gap. Adapted from Ref. [106] with permission from Princeton University Press.

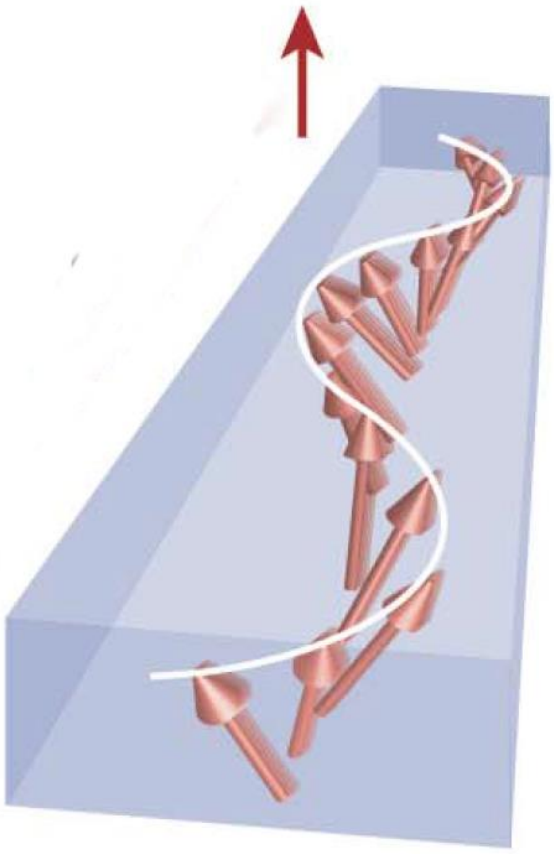

Figure 1.5 Schematic of a spin wave propagating through a material in an external field oriented in the direction of the solid red arrow. The precessing magnetic moments of neighboring spin sites (shaded red arrows) are offset by a discrete angle, resulting in wave behavior. Adapted from Ref. [110] with permission from Nature Publishing Group.

References

(1) Chang, C.-C.; Pai, C.-L.; Chen, W.-C.; Jenekhe, S. A. *Thin Solid Films* **2005**, *479*, 254.

(2) Eda, G.; Chhowalla, M. *Nano Lett.* **2009**, *9*, 814.

(3) Kirby, P. L. *Thin Solid Films* **1978**, *50*, 211.

(4) Newman, C. R.; Frisbie, C. D.; da Silva Filho, D. A.; Bredas, J.-L.; Ewbank, P. C.; Mann, K. R. *Chem. Mater.* **2004**, *16*, 4436.

(5) Nomura, K.; Ohta, H.; Ueda, K.; Kamiya, T.; Hirano, M.; Hosono, H. *Science (Washington, DC, U. S.)* **2003**, *300*, 1269.

(6) Sun, Y.; Rogers, J. A. *Adv. Mater. (Weinheim, Ger.)* **2007**, *19*, 1897.

(7) Yan, H.; Chen, Z.; Zheng, Y.; Newman, C.; Quinn, J. R.; Dotz, F.; Kastler, M.; Facchetti, A. *Nature (London, U. K.)* **2009**, *457*, 679.

(8) Collet, J.; Tharaud, O.; Chapoton, A.; Vuillaume, D. *Appl. Phys. Lett.* **2000**, *76*, 1941.

(9) Huijben, M.; Rijnders, G.; Blank, D. H. A.; Bals, S.; Van Aert, S.; Verbeeck, J.; Van Tendeloo, G.; Brinkman, A.; Hilgenkamp, H. *Nat. Mater.* **2006**, *5*, 556.

(10) Mavropoulos, P.; Papanikolaou, N.; Dederichs, P. H. *Phys. Rev. Lett.* **2000**, *85*, 1088.

(11) Kats, M. A.; Blanchard, R.; Genevet, P.; Capasso, F. *Nat. Mater.* **2013**, *12*, 20.

(12) Spinelli, P.; Verschuuren, M. A.; Polman, A. *Nat. Commun.* **2012**, *3*, 1691/1.

(13) Thomas, I. M. *Appl. Opt.* **1987**, *26*, 4688.

(14) Berger, M. G.; Arens-Fischer, R.; Thoenissen, M.; Krueger, M.; Billat, S.; Lueth, H.; Hilbrich, S.; Theiss, W.; Grosse, P. *Thin Solid Films* **1997**, *297*, 237.

(15) Frank, M.; Schallenberg, U. B.; Kaiser, N. *Opt. Eng. (Bellingham, Wash.)* **1997**, *36*, 1220.

(16) Frey, L.; Parrein, P.; Raby, J.; Pelle, C.; Herault, D.; Marty, M.; Michailos, J. *Opt Express* **2011**, *19*, 13073.

(17) Gregg, J. F.; Allen, W.; Ounadjela, K.; Viret, M.; Hehn, M.; Thompson, S. M.; Coey, J. M. D. *Phys. Rev. Lett.* **1996**, *77*, 1580.

(18) New, R. M. H.; Pease, R. F. W.; White, R. L. *J. Vac. Sci. Technol., B* **1994**, *12*, 3196.

(19) Ledermann, N.; Baborowski, J.; Muralt, P.; Xantopoulos, N.; Tellenbach, J. M. *Surf. Coat. Technol.* **2000**, *125*, 246.

(20) Zubillaga, O.; Cano, F. J.; Azkarate, I.; Molchan, I. S.; Thompson, G. E.; Cabral, A. M.; Morais, P. J. *Surf. Coat. Technol.* **2008**, *202*, 5936.

(21) Swain, G. M. *J. Electrochem. Soc.* **1994**, *141*, 3382.

(22) Amaratunga, G. A. J.; Chhowalla, M.; Kiely, C. J.; Alexandrou, I.; Aharonov, R.; Devenish, R. M. *Nature (London)* **1996**, *383*, 321.

(23) Stuber, M.; Leiste, H.; Ulrich, S.; Holleck, H.; Schild, D. *Surf. Coat. Technol.* **2002**, *150*, 218.

(24) Stueber, M.; Holleck, H.; Leiste, H.; Seemann, K.; Ulrich, S.; Ziebert, C. *J. Alloys Compd.* **2009**, *483*, 321.

(25) Elshabini-Riad, A. A. R.; Barlow, F. D. *Thin film technology handbook*; McGraw-Hill, 1998.

(26) Maissel, L. I.; Francombe, M. H. *An Introduction To Thin Films*; Gordon and Breach Science Publishers, 1973.

(27) Ohring, M. *Materials Science of Thin Films*; Elsevier Science, 2001.

(28) Ramanathan, S. *Thin Film Metal-Oxides: Fundamentals and Applications In Electronics and Energy*; Springer US, 2010.

(29) Rancourt, J. D. *Optical Thin Films: Users Handbook*; SPIE Optical Engineering Press, 1996.

(30) Voevodin, A. A.; Shtansky, D. V.; Levashov, E. A. *Nanostructured Thin Films and Nanodispersion Strengthened Coatings*; Springer, 2004.

(31) Wagendristel, A.; Wang, Y. *An introduction to physics and technology of thin films*; World Scientific Publishing Company Incorporated, 1994.

(32) Wright, J. D.; Sommerdijk, N. A. J. M. *Sol Gel Materials: Chemistry and Applications*; Taylor & Francis: London, 2001.

(33) Klaus, J. W.; Sneh, O.; Ott, A. W.; George, S. M. *Surf. Rev. Lett.* **1999**, *6*, 435.

(34) Ponraj, J. S.; Attolini, G.; Bosi, M. *Crit. Rev. Solid State Mater. Sci.* **2013**, *38*, 203.

(35) Schlom, D. G.; Haeni, J. H.; Lettieri, J.; Theis, C. D.; Tian, W.; Jiang, J. C.; Pan, X. Q. *Materials Science and Engineering: B* **2001**, *87*, 282.

(36) Schlom, D. G.; Chen, L.-Q.; Pan, X.; Schmehl, A.; Zurbuchen, M. A. *J. Am. Ceram. Soc.* **2008**, *91*, 2429.

(37) Millon, E. *Applied Surface Science* **2013**, *278*, 2.

(38) Lackner, J. M. *Vacuum* **2005**, *78*, 73.

(39) Kuzminykh, Y.; Dabirian, A.; Reinke, M.; Hoffmann, P. *Surf. Coat. Technol.* **2013**, *230*, 13.

(40) Reinke, M.; Kuzminykh, Y.; Hoffmann, P. *Chemistry of Materials* **2015**, *27*, 1604.

(41) Jensen, L. O.; Ristau, D., 2012; p 853013.

(42) Grove, W. R. *Philosophical Transactions of the Royal Society of London* **1852**, *142*, 87.

(43) Brinker, C. J.; Frye, G. C.; Hurd, A. J.; Ashley, C. S. *Thin Solid Films* **1991**, *201*, 97.

(44) Innocenzi, P.; Zub, I. U. L.; Kessler, V. G. *Sol-gel Methods for Materials Processing: Focusing on Materials for Pollution Control, Water Purification, and Soil Remediation ; [proceedings of the NATO Advanced Research Workshop on Sol-Gel Approaches to Materials for Pollution Control, Water Purification and Soil Remediation, Kyiv, Ukraine, 25 - 27 October 2007]*; Springer Science+Business Media B.V., 2008.

(45) Brinker, C. J.; Scherer, G. W. *Sol-gel science : The Physics and Chemistry of Sol-Gel Processing*; Academic Press, Inc. : San Diego, 1990.

(46) Barhoum, M.; *Manipulation and characterization of thin-film interfacial chemistry: sol-gel deposition and single molecule tracking experiments*; University of Utah, 2012.

(47) Kim, Y.-H.; Heo, J.-S.; Kim, T.-H.; Park, S.; Yoon, M.-H.; Kim, J.; Oh, M. S.; Yi, G.-R.; Noh, Y.-Y.; Park, S. K. *Nature* **2012**, *489*, 128.

(48) Biteau, J.; Chaput, F.; Lahlil, K.; Boilot, J.-P.; Tsivgoulis, G. M.; Lehn, J.-M.; Darracq, B.; Marois, C.; Lévy, Y. *Chemistry of Materials* **1998**, *10*, 1945.

(49) Schüler, A.; Dutta, D.; de Chambrier, E.; Roecker, C.; De Temmerman, G.; Oelhafen, P.; Scartezzini, J.-L. *Solar Energy Materials and Solar Cells* **2006**, *90*, 2894.

(50) Rabaste, S.; Bellessa, J.; Brioude, A.; Bovier, C.; Plenet, J. C.; Brenier, R.; Marty, O.; Mugnier, J.; Dumas, J. *Thin Solid Films* **2002**, *416*, 242.

(51) Kozuka, H.; Takenaka, S.; Tokita, H.; Hirano, T.; Higashi, Y.; Hamatani, T. *Journal of Sol-Gel Science and Technology* **2003**, *26*, 681.

(52) Kohoutek, T.; Orava, J.; Wagner, T.; Hrdlicka, M.; Vlcek, M.; Frumar, M. *J. Phys. Chem. Solids* **2008**, *69*, 2070.

(53) Barhoum, M.; Morrill, J. M.; Riassetto, D.; Bartl, M. H. *Chemistry of Materials* **2011**, *23*, 5177.

(54) Azenha, M. A.; Nogueira, P. J.; Silva, A. F. *Anal. Chem.* **2006**, *78*, 2071.

(55) Orefice, R. L.; Hench, L. L.; Clark, A. E.; Brennan, A. B. *J Biomed Mater Res* **2001**, *55*, 460.

(56) Peltola, T.; Jokinen, M.; Veittola, S.; Rahiala, H.; Yli-Urpo, A. *Biomaterials* **2001**, *22*, 589.

(57) Wang, Z.; Xiao, C.; Wu, C.; Han, H. *J. Chromatogr. A* **2000**, *893*, 157.

(58) Zhou, Z. P.; Wang, Z. Y.; Wu, C. Y.; Zhan, W.; Xu, Y. *Anal. Lett.* **1999**, *32*, 1675.

(59) Aguilar, D. H.; Torres-Gonzalez, L. C.; Torres-Martinez, L. M.; Lopez, T.; Quintana, P. *Journal of Solid State Chemistry* **2001**, *158*, 349.

(60) Jorand, Y.; Taha, M.; Missiaen, J. M.; Montanaro, L. *Journal of the European Ceramic Society* **1995**, *15*, 469.

(61) Hüsing, N.; Schubert, U. *Angewandte Chemie International Edition* **1998**, *37*, 22.

(62) Schneider, M.; Baiker, A. *Catalysis Today* **1997**, *35*, 339.

(63) Pajonk, G. M. *Journal of Non-Crystalline Solids* **1998**, *225*, 307.

(64) Komarneni, S. *J. Sol-Gel Sci. Technol.* **1996**, *6*, 127.

(65) Livage, J.; Henry, M.; Sanchez, C. *Prog. Solid State Chem.* **1988**, *18*, 259.

(66) Baes, C. F.; Mesmer, R. E. *The hydrolysis of cations*; Wiley, 1976.

(67) Livage, J.; Henry, M.; Sanchez, C. *Progress in Solid State Chemistry* **1988**, *18*, 259.

(68) Stöber, W.; Fink, A.; Bohn, E. *Journal of Colloid and Interface Science* **1968**, *26*, 62.

(69) Bartl, M. H.; Boettcher, S. W.; Frindell, K. L.; Stucky, G. D. *Acc. Chem. Res.* **2005**, *38*, 263.

(70) Klein, L. C. *Sol-Gel technology for thin films, fibers, preforms, electronics, and specialty shapes*; Noyes Publications: Park Ridge, NJ, 1988.

(71) Cammarata, R. C. *Prog. Surf. Sci.* **1994**, *46*, 1.

(72) Cammarata, R. C.; Trimble, T. M.; Srolovitz, D. J. *J. Mater. Res.* **2000**, *15*, 2468.

(73) Spaepen, F. *Acta Materialia* **2000**, *48*, 31.

(74) Sheppard, C. J. R. *Pure and Applied Optics: Journal of the European Optical Society Part A* **1995**, *4*, 665.

(75) Wood, R. M. *Laser-Induced Damage of Optical Materials*; CRC Press, 2003.

(76) Yablonovitch, E. *Phys. Rev. Lett.* **1987**, *58*, 2059.

(77) John, S. *Physical Review Letters* **1987**, *58*, 2486.

(78) Joannopoulos, J. D.; Villeneuve, P. R.; Fan, S. *Nature (London)* **1997**, *386*, 143.

(79) Yablonovitch, E. *Sci Am* **2001**, *285*, 47.

(80) Soukoulis, C. M. *Physica Scripta* **1996**, *1996*, 146.

(81) Kittel, C. *Introduction to Solid State Physics*; Wiley, 2004.

(82) Jorgensen, M. R.; Galusha, J. W.; Bartl, M. H. *Phys. Rev. Lett.* **2011**, *107*, 143902/1.

(83) Edrington, A. C.; Urbas, A. M.; DeRege, P.; Chen, C. X.; Swager, T. M.; Hadjichristidis, N.; Xenidou, M.; Fetters, L. J.; Joannopoulos, J. D.; Fink, Y.; Thomas, E. L. *Adv. Mater. (Weinheim, Ger.)* **2001**, *13*, 421.

(84) Ge, J.; Yin, Y. *Angew. Chem., Int. Ed.* **2011**, *50*, 1492.

(85) Joannopoulos, J. D.; Villeneuve, P. R.; Fan, S. *Solid State Commun.* **1997**, *102*, 165.

(86) Jorgensen, M. R.; Bartl, M. H. *J. Mater. Chem.* **2011**, *21*, 10583.

(87) Lim, T. *Proc. SPIE-Int. Soc. Opt. Eng.* **1999**, *3791*, 104.

(88) Okamoto, S. *Nippon Gomu Kyokaishi* **2013**, *86*, 315.

(89) Eichenfield, M.; Chan, J.; Camacho, R. M.; Vahala, K. J.; Painter, O. *Nature* **2009**, *462*, 78.

(90) Kushwaha, M. S.; Halevi, P.; Martinez, G.; Dobrzynski, L.; Djafari-Rouhani, B. *Phys. Rev. B: Condens. Matter* **1994**, *49*, 2313.

(91) Lu, M. H.; Feng, L.; Chen, Y.-F. *Mater. Today (Oxford, U. K.)* **2009**, *12*, 34.

(92) Aravantinos-Zafiris, N.; Sigalas, M. M.; Kafesaki, M.; Economou, E. N. *AIP Adv.* **2014**, *4*, 124203/1.

(93) Fok, L.; Ambati, M.; Zhang, X. *MRS Bull.* **2008**, *33*, 931.

(94) Olsson, R. H., III; El-Kady, I. *Meas. Sci. Technol.* **2009**, *20*, 012002/1.

(95) Pennec, Y.; Vasseur, J. O.; Djafari-Rouhani, B.; Dobrzynski, L.; Deymier, P. A. *Surf. Sci. Rep.* **2010**, *65*, 229.

(96) Chumak, A. V.; Pirro, P.; Serga, A. A.; Kostylev, M. P.; Stamps, R. L.; Schultheiss, H.; Vogt, K.; Hermsdoerfer, S. J.; Laegel, B.; Beck, P. A.; Hillebrands, B. *Appl. Phys. Lett.* **2009**, *95*, 262508/1.

(97) Chumak, A. V.; Serga, A. A.; Wolff, S.; Hillebrands, B.; Kostylev, M. P. *J. Appl. Phys.* **2009**, *105*, 083906/1.

(98) Kostylev, M.; Schrader, P.; Stamps, R. L.; Gubbiotti, G.; Carlotti, G.; Adeyeye, A. O.; Goolaup, S.; Singh, N. *Appl. Phys. Lett.* **2008**, *92*, 132504/1.

(99) Krawczyk, M.; Grundler, D. *J. Phys.: Condens. Matter* **2014**, *26*, 123202/1.

(100) Krawczyk, M.; Puszkarski, H. *Phys. Rev. B: Condens. Matter Mater. Phys.* **2008**, *77*, 054437/1.

(101) Kruglyak, V. V.; Hicken, R. J. *J. Magn. Magn. Mater.* **2006**, *306*, 191.

(102) Kruglyak, V. V.; Kuchko, A. N. *J. Magn. Magn. Mater.* **2004**, *272-276*, 302.

(103) Mruczkiewicz, M.; Krawczyk, M.; Sakharov, V. K.; Khivintsev, Y. V.; Filimonov, Y. A.; Nikitov, S. A. *J. Appl. Phys. (Melville, NY, U. S.)* **2013**, *113*, 093908/1.

(104) Wang, Z. K.; Zhang, V. L.; Lim, H. S.; Ng, S. C.; Kuok, M. H.; Jain, S.; Adeyeye, A. O. *ACS Nano* **2010**, *4*, 643.

(105) Meade, R. D.; Rappe, A. M.; Brommer, K. D.; Joannopoulos, J. D. *J. Opt. Soc. Am. B: Opt. Phys.* **1993**, *10*, 328.

(106) Joannopoulos, J. D.; Johnson, S. G.; Winn, J. N.; Meade, R. D. *Photonic Crystals: Molding the Flow of Light (Second Edition)*; Princeton University Press, 2011.

(107) Serga, A. A.; Chumak, A. V.; Hillebrands, B. *J. Phys. D: Appl. Phys.* **2010**, *43*, 264002/1.

(108) Dionne, G. F. *Magnetic Oxides*; Springer US, 2010.

(109) Wang, Z. K.; Zhang, V. L.; Lim, H. S.; Ng, S. C.; Kuok, M. H.; Jain, S.; Adeyeye, A. O. *Appl. Phys. Lett.* **2009**, *94*, 083112/1.

(110) Kajiwara, Y.; Harii, K.; Takahashi, S.; Ohe, J.; Uchida, K.; Mizuguchi, M.; Umezawa, H.; Kawai, H.; Ando, K.; Takanashi, K.; Maekawa, S.; Saitoh, E. *Nature* **2010**, *464*, 262.

CHAPTER 2

SYNTHESIS OF DIELECTRIC MULTILAYER BRAGG STACKS

Adapted with permission from: Michael R. Dahlby, Moussa Barhoum, and Michael H. Bartl, *Sol-gel-derived thin-film stacks with high radiation stability*, Thin Solid Films, **2014**, 562, pp 435-439, Elsevier.

Introduction

Sol-gel chemistry is an attractive, fast, and inexpensive alternative to vapor-deposition methods for fabricating metal oxide thin films and multilayer stacks[1-3]. However, for sol-gel methods to produce high-quality optical and electronic thin-film materials with properties rivaling those of structures produced by vapor deposition, careful tuning of the synthesis and processing conditions is required. The foremost challenge of sol-gel methods is to avoid crack formation during multilayer stack fabrication[4-7]. Successful methods for formation of crack-free films are spin-coating from metal-peroxo solutions[8], high temperature firing processes (900-1000 °C)[9-10], and the flash-heating/shock-cooling procedure of sol-gel dip-coated films developed in the Bartl lab[11-12]. Typically, the final step of solution-based film fabrication is thermal annealing of the samples at elevated temperatures (300-1000 °C). This step is thought to densify the

condensed metal oxide framework, convert remaining hydroxyl groups into bridging bonds, and, in certain metal oxides such as titania, induce crystallization[13-15].

Due to the concurrent events of solution drainage, solvent evaporation, precursor condensation, and pore collapse, cracking of the forming thin film is a major hurdle to using sol-gel processing at a large scale and can occur at multiple stages of the process, including the drying, annealing, and cooling steps[4,6,16]. Previous work in the Bartl lab was successful in introducing a procedure for overcoming this challenge for the deposition of sol-gel thin films. The key to the procedure is incorporating a very rapid "shock" cooling step after annealing the film. This reduces the time required for annealing and cooling steps, thus decreasing the overall time necessary for depositing multilayer films.

In this chapter, parameters for optimizing each step of the shock-cooling method for thin film deposition are examined, as well as the effects of thermal annealing on structural and optical properties of silica-titania multilayer thin-film Bragg stacks. We show thermal annealing has a positive effect on intra-layer properties, including oxide network densification and higher degree of crystallinity for titania layers.

Experimental Section

Materials

Tetraethylorthosilicate (TEOS) and titanium (IV) isopropoxide were purchased from Sigma and used without further preparation. Silicon (University Wafer) and quartz substrates (Chemglass) were cut to the desired size, cleaned with isopropanol and dried with a stream of air prior to film deposition.

Solution Preparation

Silica precursor stock solutions were prepared by mixing 105 mL of TEOS with 12.3 mL of deionized water, 76 mL of absolute ethanol (EtOH), and 6.3 mL of 0.1 M hydrochloric acid. The homogenized solution was aged at 60 °C for two days and then stored at room temperature. The stock titania precursor solution was prepared by adding 60 mL of titanium (IV) isopropoxide (98%) and 65 mL of absolute ethanol under stirring. Once the exothermic reaction cooled to room temperature, a pre-mixed solution of 18.3 mL deionized water, 3.79 L absolute ethanol, and 35.1 mL concentrated (12.1 M) hydrochloric acid was added. Prior to dip-coating the viscosity of both stock solutions can be adjusted by dilution with absolute ethanol to tune the thickness of the deposited layers.

Film Deposition / Annealing

Thin-films were formed by dip-coating from diluted precursor solutions. For this, cleaned substrates (silicon wafers or quartz slides) were immersed into the precursor solution and withdrawn at a constant speed of 12.6 cm/min. Following dip-coating, a hot air gun was used to rapidly evaporate solvent. The sample was then placed onto an aluminum block in a pre-heated muffle furnace at 450 °C for 20 seconds. Heating was immediately followed by a shock-cooling step. This was done by placing the hot samples onto another aluminum block kept at room temperature. For films deposited onto a thicker quartz substrate, it was necessary to place the sample into a pool of cooling solution (3:1 isopropanol/water) located on top of the aluminum block and/or spraying coolant solution onto the film. These four steps (dip-coating, evaporating, heating, and shock-cooling) were repeated alternately for silica and titania to form an optical Bragg stack of 12 alternating

layers. To test the effect of thermal annealing on sample properties, three Bragg stacks were prepared under identical conditions. One of the samples was left at room temperature, while the other two were annealed for three hours each, one at 400 °C and the other at 700 °C. In both cases the heating rate for annealing was set at 5 °C/min.

X-Ray Diffraction

The crystallinity of the titania layers was analyzed by X-ray diffraction (XRD) using a Philips X-pert diffractometer with CuKα radiation. Diffraction peak positions were referenced against JCPDS reference cards.

Scanning Electron Microscopy

Scanning electron microscopy (SEM) analysis was performed using a FEI NovaNano 630 microscope. A thin layer of gold was sputtered onto the samples when necessary to reduce charging effects. Cross-section images were obtained by splitting the substrate perpendicular to the deposited film direction. The sample was then mounted onto a vertical sample holder with the split surface facing the electron beam.

Optical Reflectance Spectroscopy

Scanning optical micro-reflection spectra were recorded on a modified optical microscope (Nikon ME600). White light from a halogen bulb in a Nikon LHS-H100P-2 lamp house was focused onto the sample by a 20x objective (0.45 NA) and the reflected light collected by the same objective was fiber-coupled into an Ocean Optics USB-4000 UV-VIS spectrometer. A broadband mirror ($R > 0.98$) was used as reference.

Spectral Modeling

Modeling of the reflectance spectra was performed using the transfer-matrix method in OpenFilters, an open-source software with a built-in graphical interface (available under the GNU General Public License)[17].

Results and Discussion

Solution Preparation

The kinetics of silica and titania condensation must be controlled in order to synthesize high-quality thin films. For silica, this is done by adjusting the pH of the solution so that it is near the isolectric point of silica, which is in the pH range of 1-3. This significantly increases the gel time, meaning that the rate of condensation in solution is slowed. This allows for the increased rate of condensation responsible for film formation to be driven by solvent evaporation during the dip-coating withdrawal process. The solution is then aged at elevated temperature to initiate the cross-linking process. Once cooled to room temperature, the sol may be used to synthesize high-quality silica films for up to four weeks.

Titania sols display much different behavior than their silica counterparts due to the high reactivity of titanium (IV) species. Unlike silicon precursors, which undergo rather slow hydrolysis and condensation processes leading to branched gel networks, titanium precursors undergo vigorous and strongly exothermic hydrolysis and condensation reactions leading to dense precipitates rather than gels. This makes stabilization of the sol much more important and challenging in order to synthesize high-quality films. Highly acidic conditions have been shown to stabilize Ti(IV) species in solution, but in some cases

this stabilization precludes condensation from occurring at all and may require gentle heating or a catalyst to initiate the process. In addition, TiO_2 can precipitate in the presence of excess water, oxygen, and light. Therefore, additional considerations are required regarding the manner in which the sol is prepared and subsequently stored. First, the reaction vessel was rinsed with alcohol and then dried and flushed with a stream of nitrogen. Prior to the addition of the reactants, the container was wrapped with foil to prevent photocatalysis. Finally, the storage container was flushed with a gentle stream of nitrogen after every use and stored in a purge box when not in use. With proper preparation and storage, a titania sol prepared in this manner may be used to synthesize high-quality films for up to several weeks.

From these solutions, high-quality Bragg stacks can be prepared by the 4-step dip-coating process described in this chapter. **Figure 2.1** shows a photograph of a 12-layer Bragg stack illustrating the visible homogeneity of a typical stack obtained by this method and an SEM cross-section image showing the quality of each individual layer. Prior to dip-coating, aliquots of the stock precursor solutions were diluted volumetrically with absolute ethanol to adjust the viscosity of the precursor solution. This allows for a method of tuning the thickness of the deposited layer. In this way, large volumes of stock precursor solution may conveniently prepared beforehand and diluted down the yield a film of desired thickness. This tunability allows for preparation of Bragg stacks with reflection bands anywhere in the visible range (**Figure 2.2**) that are stable over long periods of time.

Dip-coating Process

The dip-coating process is performed by lowering a substrate vertically into a precursor solution and withdrawing it at a constant rate. As the substrate is withdrawn, a small portion of the solution rises with it. As the solvent evaporates from this portion, the concentration of precursors increases, resulting in particulate aggregation and cross-linking until a film is formed. The thickness of the deposited film is dependent on several factors, including the rate of withdrawal and the viscosity of the solution. While solvent evaporation has a minimal effect on the viscosity of the bulk solution in the amount of time it takes to dip-coat, the evaporation of volatile solvents such as ethanol have a large effect on the viscosity of the small portion of solution that rises with the substrate. Therefore, an inconsistent rate of evaporation across the area of the developing film will result in an inconsistent thickness profile.

The most ideal method for mitigating this issue is to perform the dip-coating process in a closed environment free from drafts and other factors that can cause inconsistent vapor diffusion away from the film. However, bench-top synthesis is a major advantage of this technique and obtaining an enclosure large enough to contain all the necessary equipment is not always possible. Therefore, certain measures were taken in an attempt to maximize area of homogeneity, or "sweet spot," of the deposited film. First, the volume of precursor solution was reduced (and reactant ratios scaled accordingly), maximizing the distance between the substrate-solution interface and the top of the solution container where the partial pressure gradient is the greatest. Second, the solution container was placed into a taller secondary beaker that was then partially-filled with ethanol. The taller beaker further protects the substrate-solution interface and the addition of ethanol

helps to saturate the environment, promoting a more uniform partial pressure gradient and consistent vapor diffusion. The effect of these adjustments on thickness homogeneity are shown in a series of photographs in **Figure 2.4**. From left to right, the middle area of each of films contains a larger area of consistent color, suggesting a more homogeneous thickness profile.

Another potential challenge in thin-film deposition by dip-coating in a simple benchtop setting is the inclusion of air-born dust particles. Such particles can cause inclusion defects within any given layer, which affects not only the composition of the layer in that particular spot but also the thickness profile of the surrounding area. **Figure 2.5a** shows a cross-section SEM image of such an inclusion defect, illustrating how the thickness of successive layers is decreased in the vicinity of the defect in order to maintain a consistent overall film thickness. The result of this variation is a rainbow-like coloration in the area surrounding the defect (**Figure 2.5b**). Such variation in thickness strongly impacts the optical properties of multi-layer film stacks. More importantly, however, such inclusion defects severely inhibit the capability of these multi-layer Bragg stacks to effectively reflect high-intensity laser light (see following chapter for details). While inclusion of dust particles can never be completely eliminated when working in open air on a bench-top, precautions were undertaken to limit the number of these inclusions. Blowing a stream of air over the film after each deposition cycle as well as handling the substrate so the film was always facing down while transporting it between steps significantly reduced the frequency and number of inclusion defects from dust particles.

Evaporation

During the substrate withdrawal step of the dip-coating process, it is imperative to maintain a constant environment to promote uniform deposition. However, once the substrate has been removed from the solution it is beneficial to evaporate excess solvent as quickly as possible. This was done by blowing a stream of hot air provided by an industrial strength hot air gun. This step helped to minimize evaporation-induced inconsistencies in the forming films. For example, if the substrate was left hanging vertically without dry-blowing, gravitational draining will continue to occur, causing an evaporation line to progress down the newly formed film along with uncondensed precursors. Whenever the excess solvent finally evaporates, these precursors will condense causing a visible streak across the newly formed film as a result of increased layer thickness. Similar drying-defects occurred on films kept in a horizontally position after dip-coating; without dry-blowing the occurrence of ring-patterns can be observed.

Flash-heating and Shock-cooling

After excess solvent has been evaporated by dry-blowing, the film requires a brief, high-temperature heating period in order to induce condensation and promote adhesion to the previous layer or substrate. Furthermore, in the case of titania thin films this step also nucleates small crystallites of anatase. A period of 20 seconds at 450 °C was found to be sufficient for multilayer Bragg stacks of up to a micron in total thickness. It should be emphasized that finding the right temperature and time of heat-treatment is crucial for the deposition of crack-free films. In addition, inadequate temperatures or insufficient time for this step can also lead to delamination of the newly formed film due to increasing interlayer

surface tensions between different layers (for example, silica and titania), or between the film and the substrate.

Figure 2.6 (a & b) shows photographs of two cases where such effects have severely marred the quality and optical reflectance properties of a silica-titania Bragg stack. Top-down and cross-section SEM images in

Figure 2.6 (c & d) show the effects of surface tension in improperly deposited films leading to delamination.

Immediately after this heating period, films were shock-cooled by placing the substrate onto a block of aluminum kept at room temperature. This acts as a thermal quenching mechanism. It rapidly reduces the amount of thermal energy and stress within the film, which would otherwise be dissipated through the formation of cracks. In this interpretation, the proposed mechanism consists of conductive heat transfer from the film, through the substrate, and into the cooling block.

The effectiveness of this method is governed by the rate of heat transfer as described by Fourier's law (Equation 2.1).

$$q = \frac{k\ A\ dT}{s} \tag{2.1}$$

Here, q is the rate of transfer, k is the thermal conductivity of the material (not to be confused with the wavevector **k** in the previous chapter), A is the area through which transfer occurs, dT is the temperature gradient, and s is the material thickness. While heat transfer through a multi-component system is more complicated, this equation qualitatively illustrates various pathways for improving the performance of the shock-cooling technique,

as well as defining its limits. Most importantly, thicker substrates and thicker films impede the effectiveness of heat dissipation and require additional steps to improve heat transfer.

These limitations can be overcome by increasing the rate of heat transfer through the use of cooling materials or substrates with higher transfer coefficients or increasing the temperature gradient during cooling. For example, replacing the aluminum blocks with copper allows for high-quality films to be synthesized while reducing the required heating temperature to as low as 300 °C. Alternatively, increasing the temperature gradient by cooling the aluminum block with dry ice or storing in a freezer while not in use can increase the allowed thickness of films before cracking occurs.

Annealing

The sol-gel process typically yields materials that are amorphous in nature. Some applications, however, including semiconductor devices and magnetic storage materials, require atomic-scale crystallinity in order to function properly. Therefore, many sol-gel synthetic processes utilize a final, post-synthetic annealing process in order to induce crystallization. While silica typically does not exhibit any crystalline phases, titania exhibits three polymorphs at atmospheric pressure including anatase, rutile, and brookite – the former two being far easier to obtain and therefore of greater technological interest. Although anatase is considered to be metastable, it is often the first crystalline phase obtained upon annealing amorphous titania[15]. Rutile, despite being the more thermodynamically stable phase, is only obtained at higher temperatures. The anatase to rutile transformation temperature is dependent on many factors including the method of

preparation, surface area, atmosphere, and heating rate and has been reported to vary from 400 – 1000 °C [14,18].

To test for crystallinity in the titania layers, diffraction spectra were recorded and are presented in **Figure 2.7**. Three observations are noteworthy: First, all three samples, including the as-prepared samples (no thermal annealing), exhibit diffraction peaks typical of polycrystalline anatase titania. This confirms the brief heating step during the layer deposition process (450 °C for 20 seconds) is sufficient to induce crystallization. Second, as expected, thermal annealing increases crystallinity, evidenced by stronger and better-defined reflections, and an increase of the anatase crystallite size from 26 to 34 nanometers as determined using the Scherrer equation (Equation 2.2).

$$x = \frac{K\,\lambda}{b\cos\theta} \tag{2.2}$$

Here, X is the average crystallite size, K is the unit-less Scherrer constant, λ is the wavelength of incident radiation, b is the line broadening expressed as the full-width-at-half-maximum (FWHM) of the reflection peak in radians, and θ is the Bragg angle of the reflection peak in radians. The value of the Scherrer constant is dependent on the shape of the crystallite, the reflection peak used for analysis, and the method of determining the line broadening. This value can vary from 0.75 to 2.1 but is typically considered to be close to unity[19]. For crystallite size determination of anatase, the 101 reflection peak and a Scherrer constant value of 0.9 are sufficient for analysis.

Third, no diffraction features of other phases of titania were detected despite rutile being thermodynamically more stable at elevated temperatures. This indicates a kinetic arrestment of the anatase phase, a property of interest for photocatalytic applications[20-21].

Optical Properties and Modeling

As mentioned above, Bragg stacks obtained via sol-gel dip-coating feature a "sweet spot" where thickness homogeneity is quite excellent and yields a consistent color when viewed by the naked eye. This sweet spot gives way to areas of varying thickness and visible color variation toward the edges of the film. These edge effects are inherent to the sol-gel process and compose a very small portion of the deposited area. Therefore, these areas were not taken into account when analyzing optical reflection properties. Reflectance spectra were always obtained from the middle of the sweet spot in order to achieve the most representative depiction of the optical properties for each film.

While thermal annealing had only a small effect on the crystallinity, the optical properties of the multilayer Bragg stacks were strongly impacted. Visibly, samples that underwent annealing treatment had stronger blue-shifted reflection colors. This observation can be quantified by optical reflection spectroscopy. A comparison of the reflection spectra is given in **Figure 2.8** and shows all three samples displayed excellent Bragg-type optical features with a broad and well-defined main reflection band of > 99 percent reflectivity. While the spectral features look similar for all three samples, the center position of the main Bragg reflection band systematically shifted to shorter wavelengths with increased annealing temperature. Additionally, heat treatment led to a broadening of the reflection band, expressed as an increase in the full-width-half-maximum (FWHM)

values from 5830 cm^{-1} for the non-annealed sample to 5860 and 6290 cm^{-1} for samples annealed at 400 and 700 °C, respectively.

Increasing the crystallinity of titania from amorphous to anatase to rutile should result in an increase in refractive index as well as a densification of the crystal structure. However, subjecting films to intense heat can cause shrinkage of the layers due to further condensing of the network. To ascertain the main cause of this shift, the OpenFilters[17] program was used to construct a model Bragg stack. Parameters (refractive indices and layer thicknesses) were varied to match the optical reflection profile of the non-annealed sample. Then, the refractive index of the titania layers as well as the thickness of both titania and silica layers were systematically altered to predict the effect of each of these properties on the position and shape of the main reflection peak.

The results of this modeling approach showed that shrinkage of titania layers has the largest effect on the change in optical properties. Increasing the overall refractive index contrast of the model Bragg stack by increasing the value for titania layers from 2.3 to 2.4 to 2.5 expectedly led to an increase in the FWHM of the main reflection band. The magnitude of these increases, consisting of 169 and 125 cm^{-1}, respectively, compare somewhat reasonably to the observed experimental increases of 14 cm^{-1} after annealing at 400 °C and 288 cm^{-1} after annealing at 700 °C. However, the position of the reflection band underwent a systematic red shift, which is in direct contrast with the observed blue shift. Adjusting the layer thicknesses, on the other hand, lead to changes more consistent with the observed shifts. Decreasing the silica layer by factors of 10 and 20 % led to FWHM increases of 21 and 7 cm^{-1}, respectively, while decreasing the titania layer thickness by the same factors led to increases of 535 and 563 cm^{-1}, respectively. Both silica and titania layer

shrinkage led to the expected blue shifts of the reflection band position, consistent with the observed results. However, the much larger magnitude of the shift due to decreasing titania layer thickness implies that this is the primary mechanism responsible for the observed changes in the optical reflection properties as a result of thermal annealing.

Conclusions

High-quality dielectric thin films were successfully deposited via a 4-step process consisting of 1) dip-coating 2) rapid solvent evaporation 3) brief thermal treatment and 4) shock-cooling. Each step of this process and its overall impact affecting the deposition of films was described in detail. Bragg stacks consisting of alternating silica and titania layers were prepared and the versatility of the process was exhibited by preparing samples with varying layer thickness, resulting in a series of samples with reflection bands spanning the entire visible range. Post-synthetic thermal annealing was found to increase the crystallinity of the titania films while resulting in a blue-shift of the main reflection peak. Results obtained from modeling the effects of increased refractive index contrast and decreased layer thickness on the reflection properties of the Bragg stacks suggest that this shift is primarily the result of titania layer shrinkage.

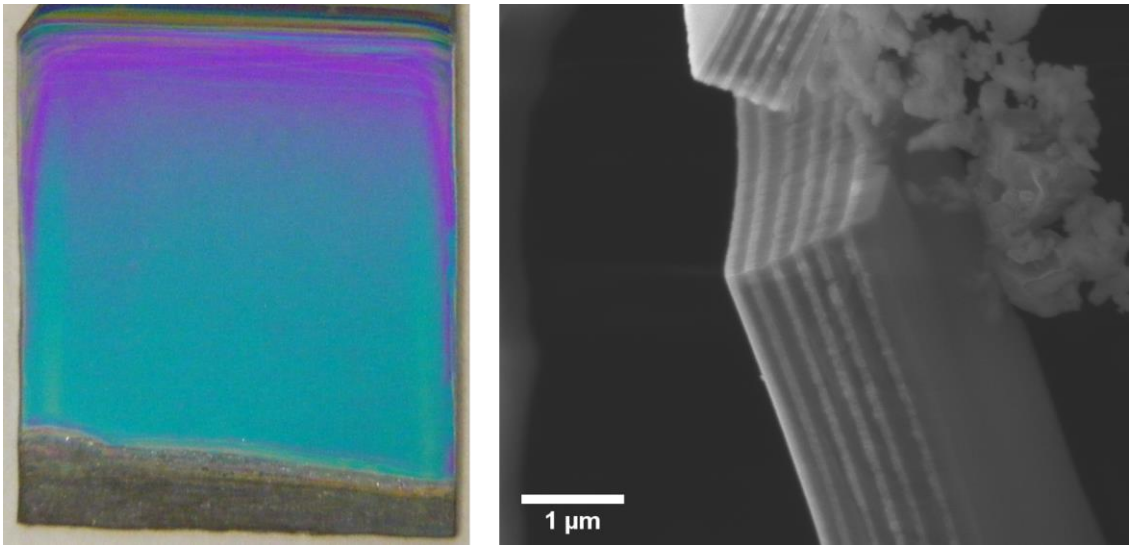

Figure 2.1 Photograph (left) of a 12-layer Bragg stack deposited on a pre-cut silicon substrate approximately 1" wide and a cross-section SEM image (right) showing 12 alternating layers of silica (dark layers) and titania (bright layers).

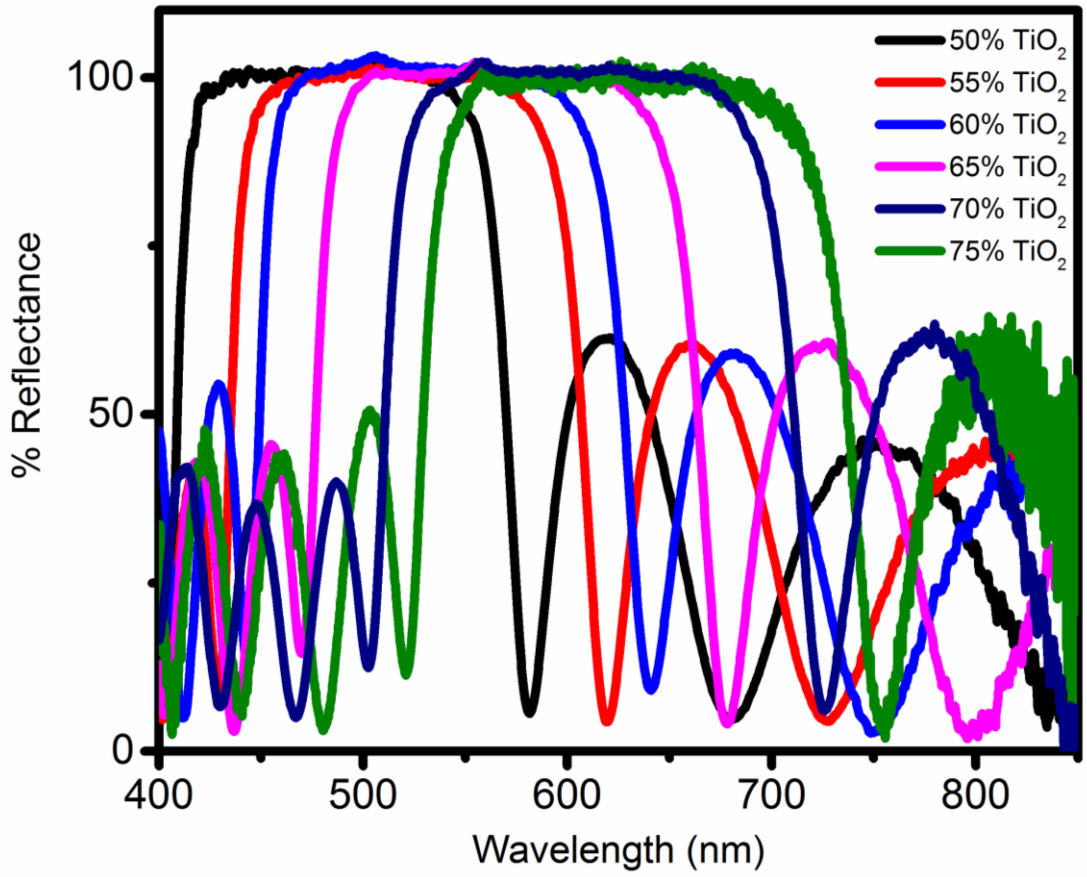

Figure 2.2 Reflectance spectra of a series of Bragg stacks fabricated by varying the dilution ratio (v:v) of titania precursor solution with ethanol. All films were fabricated with the same thickness of silica layers prepared by a 25% (v:v) ratio with ethanol.

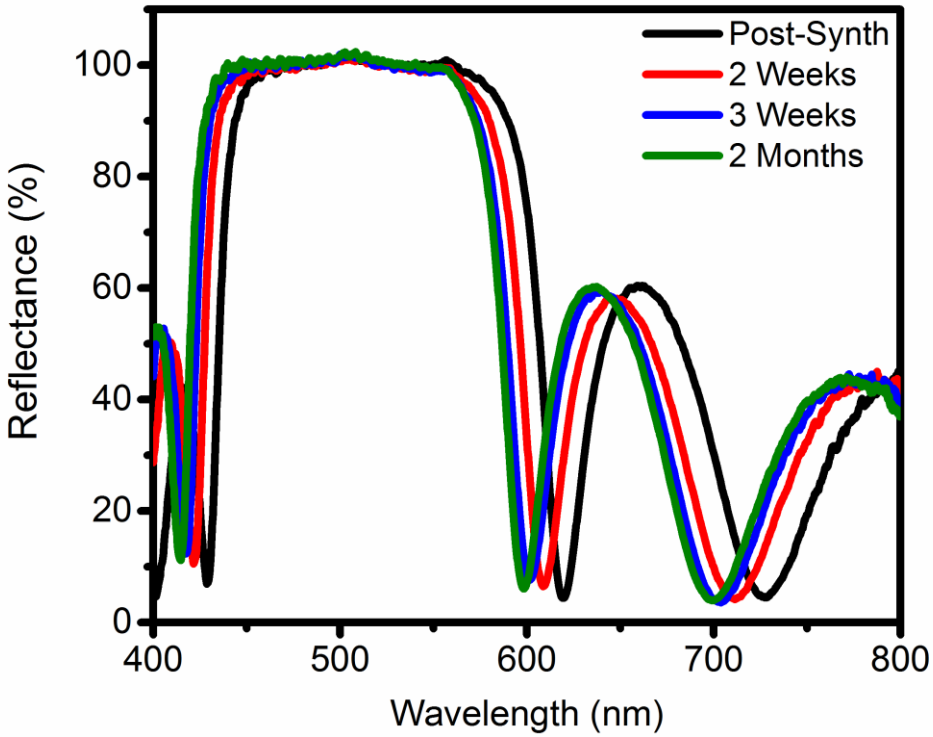

Figure 2.3 Reflectance spectra of a 12-layer Bragg stack over long periods of time.

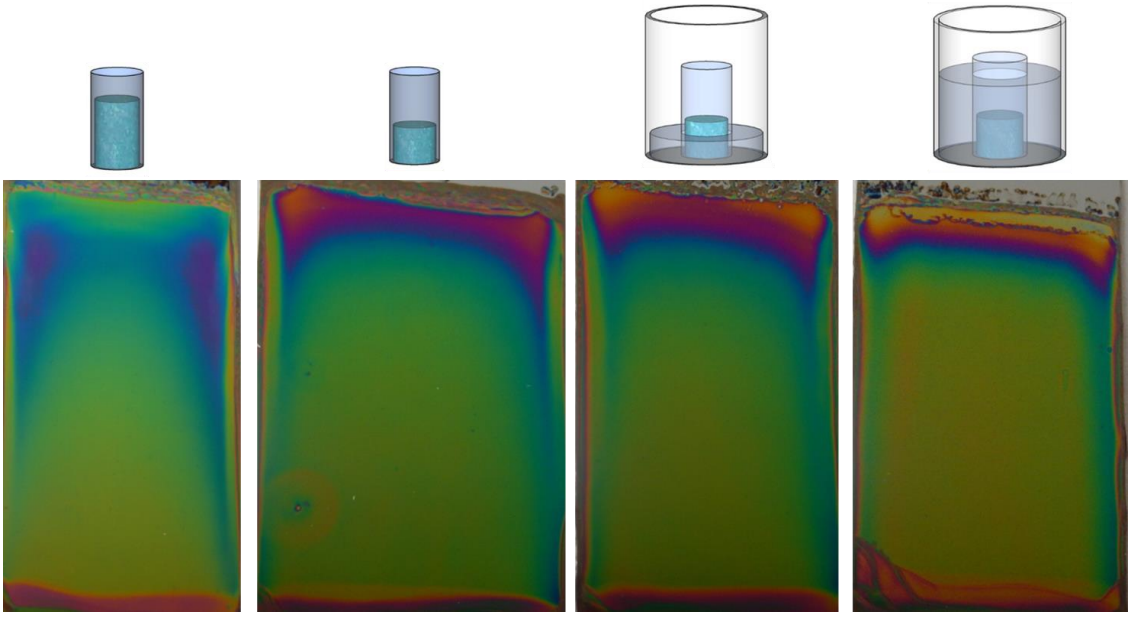

Figure 2.4 Photographs of films prepared from different saturation environments. Note the upper-left and upper-right areas of the film and the blue-colored areas along the side of the films that shrink in size from left to right, resulting in increased thickness homogeneity.

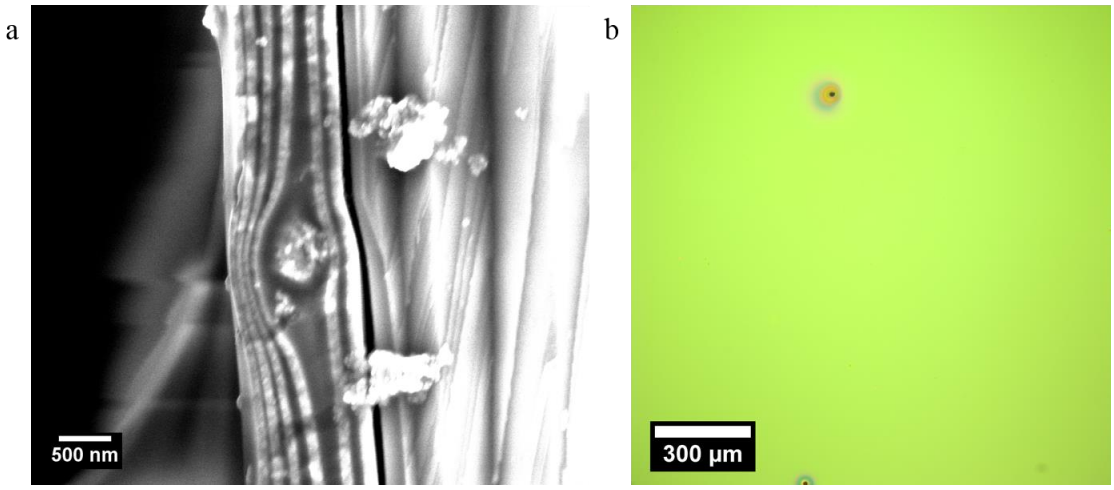

Figure 2.5 Cross-section SEM image (a) showing an inclusion defect in a Bragg stack within a silica layer and (b) an optical micrograph of color variations due to thickness inhomogeneity surrounding a defect.

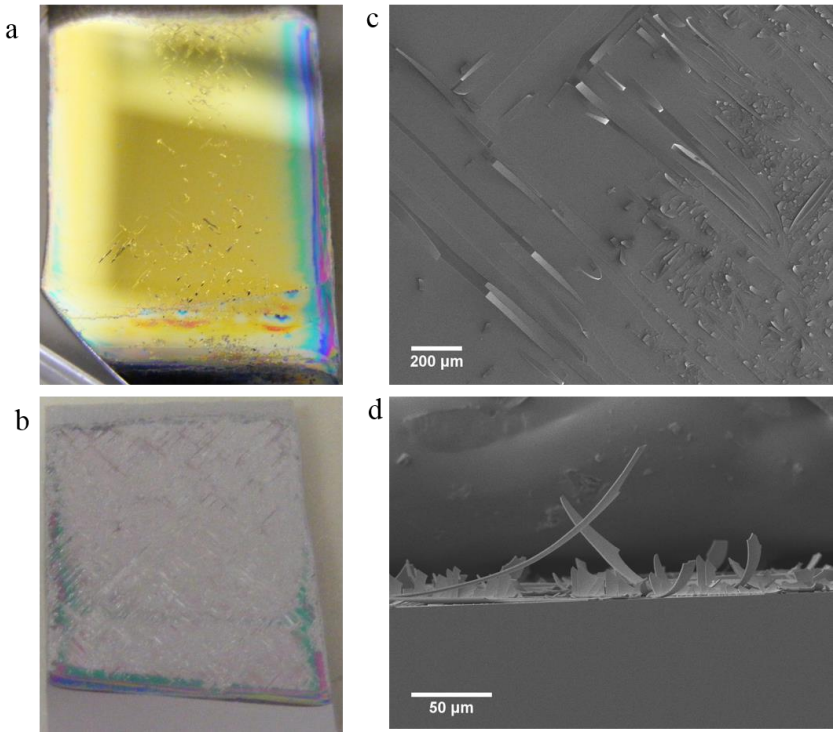

Figure 2.6 Photographs (a&b) of Bragg stacks on approximately one-inch-wide silicon substrates that were not properly flash-heated and shock-cooled. Note in b) that the extent of damage is so severe there is no visible reflection. c) top-down and d) cross-section SEM images showing strips of material completely delaminated from the substrate due to surface tension.

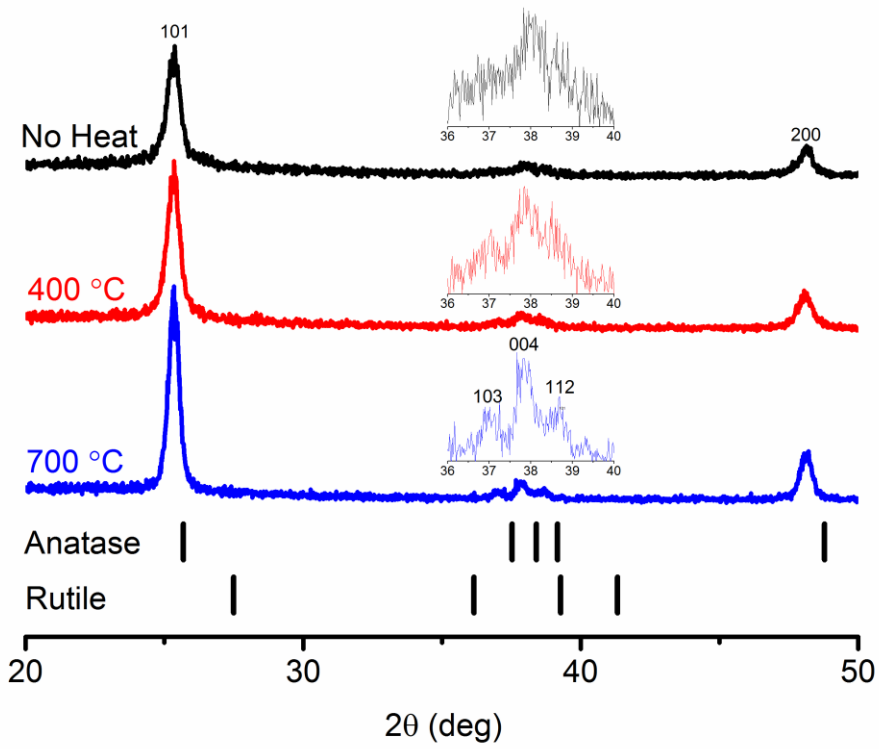

Figure 2.7 XRD patterns of films annealed at 400 °C, 700 °C, and no heat. Insets are expanded ranges from 36 to 40 degrees. Bottom dash patterns represent reflection peak positions for for Anatase (JCPDS 75-1537) and Rutile (JCPDS 87-0710) phases of titania.

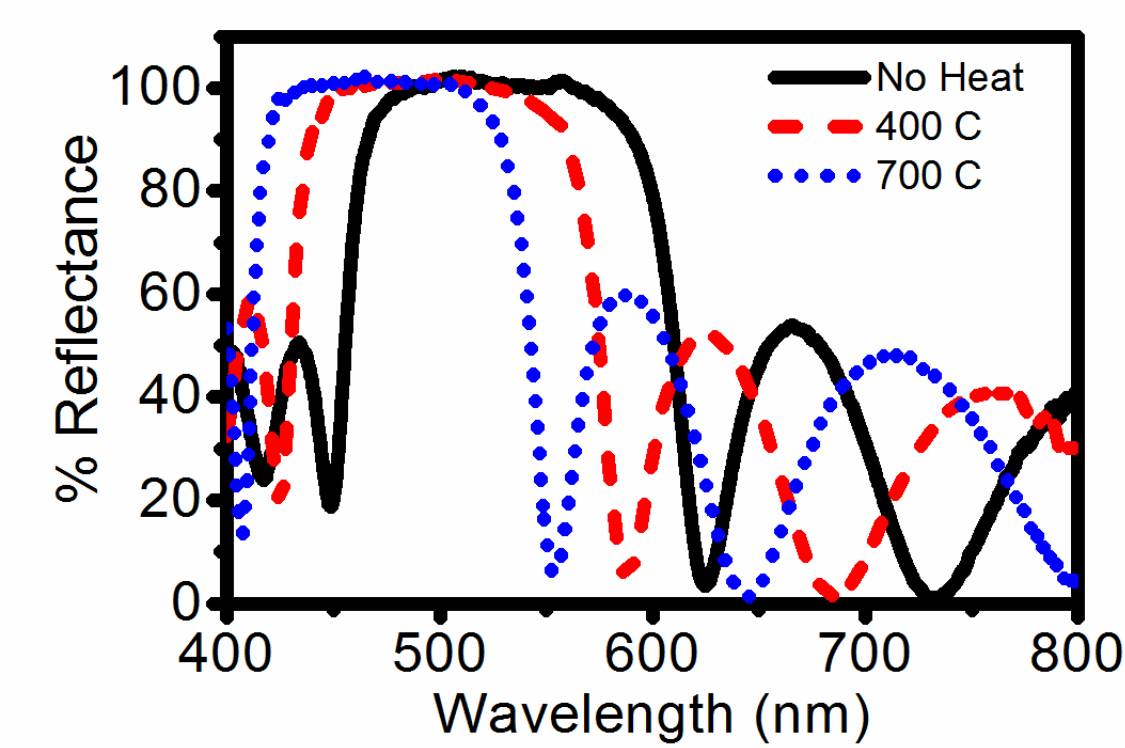

Figure 2.8 Reflectance spectra of three films with initially similar reflectance spectra after annealing at 400 °C, 700 °C, and no heat.

References

(1) Innocenzi, P.; Zub, I. U. L.; Kessler, V. G. *Sol-gel Methods for Materials Processing: Focusing on Materials for Pollution Control, Water Purification, and Soil Remediation ; [proceedings of the NATO Advanced Research Workshop on Sol-Gel Approaches to Materials for Pollution Control, Water Purification and Soil Remediation, Kyiv, Ukraine, 25 - 27 October 2007]*; Springer Science+Business Media B.V., 2008.

(2) Klein, L. C. *Sol-Gel technology for thin films, fibers, preforms, electronics, and specialty shapes*; Noyes Publications: Park Ridge, NJ, 1988.

(3) Ramanathan, S. *Thin Film Metal-Oxides: Fundamentals and Applications In Electronics and Energy*; Springer US, 2010.

(4) Cammarata, R. C. *Prog. Surf. Sci.* **1994**, *46*, 1.

(5) Cammarata, R. C.; Trimble, T. M.; Srolovitz, D. J. *J. Mater. Res.* **2000**, *15*, 2468.

(6) Kozuka, H.; Takenaka, S.; Tokita, H.; Hirano, T.; Higashi, Y.; Hamatani, T. *Journal of Sol-Gel Science and Technology* **2003**, *26*, 681.

(7) Sanchez, C.; Boissiere, C.; Grosso, D.; Laberty, C.; Nicole, L. *Chem. Mater.* **2008**, *20*, 682.

(8) Jiang, K.; Zakutayev, A.; Stowers, J.; Anderson, M. D.; Tate, J.; McIntyre, D. H.; Johnson, D. C.; Keszler, D. A. *Solid State Sciences* **2009**, *11*, 1692.

(9) Bockmeyer, M.; Löbmann, P. *Chemistry of Materials* **2006**, *18*, 4478.

(10) Rabaste, S.; Bellessa, J.; Brioude, A.; Bovier, C.; Plenet, J. C.; Brenier, R.; Marty, O.; Mugnier, J.; Dumas, J. *Thin Solid Films* **2002**, *416*, 242.

(11) Barhoum, M.; Morrill, J. M.; Riassetto, D.; Bartl, M. H. *Chemistry of Materials* **2011**, *23*, 5177.

(12) Barhoum, M., University of Utah, 2012.

(13) Brinker, C. J.; Scherer, G. W. *Sol-gel science : The Physics and Chemistry of Sol-Gel Processing*; Academic Press, Inc. : San Diego, 1990.

(14) Hanaor, D. H.; Sorrell, C. *J Mater Sci* **2011**, *46*, 855.

(15) Shannon, R. D. P., Joseph A. *Journal of the American Ceramic Society* **1965**, *48*, 391.

(16) Spaepen, F. *Acta Materialia* **2000**, *48*, 31.

(17) Larouche, S.; Martinu, L. *Appl. Opt.* **2008**, *47*, C219.

(18) Zhang, H.; Banfield, J. F. *J. Phys. Chem. B* **2000**, *104*, 3481.

(19) Langford, J. I.; Wilson, A. J. C. *J. Appl. Crystallogr.* **1978**, *11*, 102.

(20) Bartl, M. H.; Boettcher, S. W.; Frindell, K. L.; Stucky, G. D. *Acc. Chem. Res.* **2005**, *38*, 263.

(21) O'Regan, B.; Graetzel, M. *Nature (London)* **1991**, *353*, 737.

CHAPTER 3

EFFECT OF THERMAL ANNEALING ON STRUCTURE AND PHOTO-STABILITY OF BRAGG STACKS

Adapted with permission from: Michael R. Dahlby, Moussa Barhoum, and Michael H. Bartl, *Sol-gel-derived thin-film stacks with high radiation stability*, Thin Solid Films, **2014**, 562, pp 435-439, Elsevier.

Introduction

Bragg stacks are multilayer films consisting of alternating layers of dielectric materials with contrasting refractive indices[1-5]. They are commonly used as reflectors in optical setups due to their ability to withstand the high-energies of coherent laser output. Analysis of laser-induced damage threshold studies provides excellent insight into the stability, homogeneity, and overall quality of Bragg stacks[6-7]. Interest in these types of studies began in the 1960's with the invention of the ruby laser. It quickly became apparent that increasingly powerful laser output would require optical components capable of withstanding very high energies. In order for powerful laser systems to be useful, optical components capable of manipulating the beam are necessary[8-11]. Knowledge of damage initiation and propagation mechanisms is crucial to understanding how to design and fabricate components that prevent such damage from occurring[12-14]. Because this

information is vital for improving and developing new materials, and for meeting the demands of increasingly high-intensity laser output, laser-induced damage studies are of great interest[15-22].

Since laser radiation can be incredibly powerful, it is important to understand how light propagates and interacts with a Bragg stack. As light passes through the film, interference effects caused by partial reflections at the many interfaces create a standing wave that decays exponentially deeper within the stack[23]. In a quarter-wave Bragg stack this wave is most intense at the surface of the stack and at the interfacial areas of high and low dielectric layers[7]. These areas are therefore the most susceptible to laser-induced damage and are weakened by intrinsic (i.e. inherent to the process by which the material is formed) interfacial defects, surface stresses, and microcrystalline mismatches. In addition, extrinsic defects (e.g. contamination) embedded within the film can also enhance this standing wave, leading to localized heating and stress. The magnitude of enhancement is proportional to the diameter of the point defect.[6] Thus, larger defects lead to more catastrophic damage, especially when embedded deeper within the stack. Micro-cracks and pores can also enhance the standing wave[24], and therefore Bragg stacks consisting of more dense, crystalline materials are of greater interest for coatings.

The two main causes of laser-induced damage are dielectric breakdown, where exposure to an intense electrical field leads to the formation of electrically conducting regions within the insulating material (akin to a lightning strike traveling through air), and absorption in the form of heat. Both of these can be further attributed to several mechanisms as a result of intrinsic and extrinsic defects within the film. Dielectric breakdown mechanisms are enhanced by cracks, voids, particles, scattering, and surface effects

whereas thermal absorption damage mechanisms can occur through local, conduction, and transient absorption processes leading to melting, warping, thermal expansion, and cracking. Catastrophic damage to the film can be caused by any single one of these effects but is most often the result of a combination of them, adding to the difficulty of interpreting laser-induced damage mechanisms.

These damage mechanisms manifest in four main types of morphologies: nodular ejection pits, flat-bottom pits, delamination, and plasma scalding[6-7,25-33]. Both types of pit damages result from defects. Nodular ejection pits are formed when larger, micron-sized extrinsic defects are heated until ejection. The form of damage from ejection pits is characterized by deep, sometimes irregular-shaped pits that can extend into the substrate. Flat-bottom pits, on the other hand, are wide and shallow, appearing toward the surface of the stack and are the result of interfacial, nanoscale defects that are heated to a plasma state by the standing wave. Plasma scalding occurs when a plasma created by defects, contamination, or air breakdown interacts with the stack surface, and delamination occurs when outer layers of the stack is completely ablated from the surface.

While various methodologies exist to construct a statistical understanding of laser-induced damage thresholds, the goal of this chapter is to experimentally investigate the change in stability of sol-gel films due to post-synthetic annealing in a step-by-step comparative manner. As discussed above, the sol-gel process is a simple, inexpensive and versatile alternative synthesis route for thin films. However, sol-gel fabrication mechanisms of thin films are also radically different than the programmable physical vapor deposition methods. It is therefore imperative to gain in-depth knowledge of each sol-gel deposition and processing step and its impact on thin-film and multilayer stack stability.

This chapter provides such an in-depth study and will show that increasing the microstructural properties and density of the titania layers has a negative effect on interfacial properties. Network reorganization during heat treatment reduces titania-silica interlayer bonding and causes delamination and loss of reflectivity under high-power laser irradiation.

Methods

Film Preparation

Thin silica and titania films and alternating silica-titania multilayer Bragg stacks were fabricated by the 4-step method as described in Chapter 2. Prior to film deposition by dip-coating the viscosity of both the titania and silica stock solutions was adjusted by dilution with absolute ethanol to tune the thickness of the deposited layers. In detail, 5 mL of silica solution stock solution was diluted with 15 mL of ethanol (25% v/v stock SiO2, 1:1.9:25:0.004 molar ratio of TEOS:H_2O:EtOH:HCl). This dilution was kept the same for all samples. For the titania dip-coating solution three different dilutions of the stock solution were prepared. For non-annealed samples, 11 mL of titania stock solution was diluted with 9 mL of absolute ethanol (55% v/v stock TiO2, 1:0.42:33:0.097 molar ratio of Ti(O-i-Pr)4:H2O:EtOH:HCl). For samples annealed at 400 °C, 13 mL of titania stock solution was diluted with 7 mL of absolute ethanol (65% v/v stock TiO2, 1:0.42:27:0.097 molar ratio of Ti(O-i-Pr)4:H2O:EtOH:HCl). For samples annealed at 700 °C, 15 mL of titania stock solution was diluted with 5 mL of absolute ethanol (75% v/v stock TiO2, 1:0.42:23:0.097 molar ratio of Ti(O-i-Pr)4:H2O:EtOH:HCl)

Laser Irradiation

Samples were subjected to the 532 nm wavelength output of a Q-switched Continuum Surelite II-10 Nd:YAG laser. Samples were placed in a vertical sample holder in the beam path and subjected to pulses with an average radiant energy of 0.21 J at a 5 ns pulse width and a 6 mm beam diameter, resulting in maximum power density of 0.13 GW/cm^2. Initial results were obtained by subjecting Bragg stacks to a single pulse. Further stability tests were performed by subjecting each sample to 50 single-shot pulses spaced approximately one second apart. The evolution of damage morphologies was examined by subjecting samples to the same power output with a 10 Hz repetition rate for 5-second intervals. Between each interval, the sample was removed from the sample holder and investigated by optical microscopy and reflection spectroscopy. The position of the substrate in the sample holder was marked to ensure the same area of the Bragg stack would be exposed to the beam throughout the entire experiment.

Optical Microscopy and Spectroscopy

Optical reflection spectra were measured with a modified optical microscope (Nikon ME600). White light from a xenon bulb in a Nikon LHS-H100P-2 housing attachment was focused onto the sample by a 20x objective (0.45 NA) and the reflected light, collected by the same objective, was fiber-coupled into an Ocean Optics USB-4000 UV-VIS spectrometer. A broadband mirror ($R > 0.98$) was used as reflectance reference. Small-area spectra were obtained by placing an iris diaphragm in the image plane and letting only selected areas of the image pass to the entrance of the fiber couple. All spectra were referenced accordingly prior to data collection. True-color images were obtained by

removing the magnetically-mounted beam optics and inserting a SPOT Insight CCD camera into the optical path at the image plane.

Scanning Electron Microscopy

Scanning electron microscopy (SEM) analysis was performed using a FEI NovaNano 630 microscope. A thin layer of gold was sputtered onto the samples when necessary to reduce charging effects. Cross-section images were obtained by splitting the substrate perpendicular to the deposited film direction and mounting the sample onto a vertical holder with the split surface facing the electron beam.

Spectral Modeling

Modeling of the optical reflectance spectra was performed using the transfer-matrix method in OpenFilters, an open-source software with a built-in graphical interface (available under the GNU General Public License)[34].

Results and Discussion

Sample Preparation and Characterization

The effect of thermal annealing on the properties of sol-gel derived Bragg stacks was discussed in detail in the previous chapter. Briefly, thermal annealing improved crystallinity but also shifted the wavelength position of the main optical reflection band. The shift is caused by changes in the layer thickness and the dielectric properties of the silica and titania layers; with the former having a larger effect. Consequently, testing all samples with the 532 nm laser line would lead to unreliable results since the laser line

would overlap with different parts of the Bragg mirrors' reflection bands; namely, the high-wavelength edge for the non-annealed sample, and the center position and low-wavelength edge for samples annealed at 400 °C and 700 °C, respectively (see **Figure 2.8**, page 51).

Therefore, to eliminate the differences in the reflection band position between annealed (400 °C and 700 °C) and non-annealed Bragg stacks, the dilution factor of stock precursor solutions was adjusted to fabricate samples with initially thicker layers. The dilution factor was tuned (by trial and error) so that the film shrinkage due to thermal annealing was compensated and all Bragg stacks, non-annealed, annealed at 400 °C, and 700 °C, ended up having the exact same silica and titania film thicknesses at the end of the fabrication process.

An example set of samples is given in **Figure 3.1** and shows that final samples displayed near-identical optical properties with reflection bands of at least 99 percent reflectivity centered around 532 nm. The observed reflection properties indicate excellent structural quality of the Bragg stacks. Indeed, optical microscopy imaging in reflection mode revealed all samples were crack-free even at the micrometer scale. Furthermore, the uniform coloration over large areas indicates exceptional thin-film homogeneity. In fact, the only observed defects were local discoloration effects caused by the inclusion of dust particles during the dip-coating process.

Laser-Induced Damage of Bragg Stacks

To investigate the mechanisms of various damage morphologies, annealed and non-annealed samples were subjected to laser irradiation in two different modes: 1) a single laser pulse and 2) 50 consecutive laser pulses at a repetition rate of approximately 1 Hz.

After exposure all samples were examined by optical microscopy, reflection spectroscopy, and SEM imaging.

In the case of mode 1 exposure (single laser pulse at 532 nm), none of the samples displayed any observable damage in optical and electron microscopy investigations. This indicates the exposure to a single laser shot with a power density of 0.13 GW/cm^2 was not sufficient to initiate structural damage in the Bragg stack layers. In addition, the optical reflectance properties of each stack very closely matched the reflectance spectra of the samples prior to laser exposure, confirming that the optical properties of the annealed and non-annealed samples prepared in this way are indeed very similar. However, under mode 2 laser irradiation (exposing films to 50 consecutive pulses at a repetition rate of approximately 1 Hz) vastly different results were obtained.

Figure 3.2 shows optical micrographs of results obtained from a non-annealed sample (a) and samples annealed at 400 and 700 °C (b and c, respectively). In general, all of the samples showed two different types of damage: 1) Black dots surrounded by areas of discoloration and 2) dark rings consisting of micropits and "bubbling" effects, characteristic of plasma scalding. Surprisingly, however, it was found that both the sample annealed at 400 °C (**Figure 3.2b**) and 700 °C (**Figure 3.2c**) displayed much higher degree of damage than the non-annealed sample. This observation is counterintuitive and contradicts the "general rule" that thermal annealing strengthens sol-gel derived thin films and stacks. In the following, the types of damages are discussed in more detail and a proposed mechanism of damage formation with respect to thermal annealing is presented.

Types of Laser Damage Morphologies

The first type of damage morphology consists of black dots surrounded by areas of discoloration. In general, most of these damage spots are small but there is larger spots intermixed (see, for example, the large spot toward the middle-right section of the micrograph in **Figure 3.2a**). At higher magnification it becomes apparent that this particular spot has brightly-colored areas found within the circle of damage. Spectroscopic analysis of similar morphologies show that these brightly colored areas consist of intact Bragg stack remaining after the damage has occurred. **Figure 3.3** shows that reflectance properties taken of the bulk film, an area at the edge of the damage spot, and the area in the middle of the damage spot all show similar spectral features. However, the area at the edge of the spot, where there is more black color, shows lower overall reflectance than the area in the middle that is brighter. This confirms that the structure of the film, while diminished in integrity, remains intact in the middle of the spot.

SEM imaging reveals that the black spots are exposed substrate (**Figure 3.4**). This is most likely due to a damage mechanism where a pinhole defect or large inclusion defect embedded within the film causes varying layer thickness in the immediate vicinity of the defect. This changes the optical reflection properties of the surrounding area and allows the laser light to penetrate to the absorbing substrate, causeing catastrophic heating and warping of the substrate surface and resulting in a partial breakdown of the film. However, this damage morphology ends abruptly when the thickness profile returns to normal and does not extend underneath the stack beyond the immediate area of impact (**Figure 3.4b**), suggesting that the heat caused by absorption dissipates quickly and the substrate damage is localized to the area of the original defect.

The second type of damage morphology manifests as dark rings when observed at low magnification. In some cases, these rings encompass the black spots of exposed substrate described above but in other cases they appear independently. Analysis of these rings by SEM imaging reveals a high number of micropits and "bubbling" effects at the surface of the stack (**Figure 3.5**), characteristic of plasma scalding. These scalds were sometimes accompanied by nodular ejections pits found randomly within of the scald (**Figure 3.6**). Like the first damage morphology, these ejection pits also lead to exposed substrate but are much smaller and therefore less detrimental to the overall quality of the Bragg stack.

Damage Propagation

To further investigate this interesting observation of "reversed radiation stability" (i.e. reduction in radiation stability with increasing annealing temperature), and to investigate the nature of damage propagation, a new set of experiments was conducted. For this, fresh samples were subjected to 5-second intervals of continuous pulsing at a rate of 10 Hz using the same laser setting as described above. This process was conducted for a total of 30 seconds. At the end of each 5-second interval optical micrographs of the irradiated area were collected. These results are shown in **Figure 3.7**, **Figure 3.8**, and **Figure 3.9** for a non-annealed sample and samples annealed at 400 and 700 °C, respectively.

Comparison of the optical micrographs demonstrates the enormous impact high-power irradiation had on the structural and optical properties of annealed samples. In contrast, the non-annealed sample retained its homogeneous reflection color. The only

significant damage in this sample was the substrate exposure at the pre-existing inclusion defect and there is a minimal amount of plasma scalding. The annealed samples, on the other hand, show high defect densities that increase with higher annealing temperatures. The film damage is also expressed in a decrease of the optical reflectivity and a change in the main Bragg reflection band shape (**Figure 3.10**). Measured optical reflection spectra were compared to modeled spectra. The comparison reveals that good agreement in terms of spectral shape and reflectivity can only be obtained if spectra for samples annealed at 400 and 700 °C are modeled with an 11-layer and 7-layer Bragg stack, respectively. This confirms layer delamination and further illustrates the extent of damage incurred in samples annealed at higher temperatures.

Finally, to eliminate the possibility that the observed decrease in stability of thermally annealed Bragg stacks is due to any sort of substrate effect, the same experiment was performed with samples prepared on quartz substrates. These results were consistent with those obtained for stacks deposited onto silicon substrates. While the substrate-warping defects were no longer present and plasma scalding morphologies were less prominent, it was obvious that layer delamination was again much stronger for annealed samples, following the same trend as observed for stacks deposited on silicon substrates.

Proposed Radiation Damage Mechanism

In contrast to the expected structural and optical changes as a result of thermal annealing, a surprising trend was observed in the radiation stability of the samples. From the combined characterization results the following mechanism of radiation damage in thermally annealed multilayer thin-film stacks is proposed. XRD and optical reflection

spectroscopy revealed annealing facilitates densification of the individual titania and silica layers, and increases crystallinity of the titania layers. Both of these factors should result in higher radiation stability of individual layers. However, high-power laser irradiation studies showed the damage is mostly the result of plasma scalding and layer delamination, indicating the assumed higher stability within individual layers is offset by a weakening of interfacial titania-silica bonding interactions.

It is proposed this weakening is caused by increased dissimilarity of the silica and titania layers due to thermal annealing at elevated temperatures for several hours. The non-annealed (only flash-heated) titania layers have lower crystallinity than the annealed samples as indicated by XRD. While some anatase crystallites have already formed in as-deposited layers, they are surrounded by amorphous titania, and are therefore more similar to the amorphous silica layers. Thermal annealing promotes further crystallization of anatase from the amorphous titania which is accompanied by atomic rearrangement of the oxide framework. While this process increases the strength of individual titania layers, the reorganization of the metal oxide network most likely strains and breaks initially formed Si-O-Ti bonds between the silica and titania layers and induces interfacial stresses. This leads to the observed increase in observed plasma scalding and layer delamination under high-power laser irradiation.

Conclusions

The photo-stability of Bragg stacks synthesized by the 4-step sol-gel deposition procedure described in Chapter 2 was investigated by laser-induced damage threshold studies. Results obtained by optical microscopy, reflectance spectroscopy, and SEM

imaging show that Bragg stacks annealed at higher temperatures exhibit a decrease in damage threshold as a result of increased interlayer stress. These results suggest that interfacial properties rather than the quality of individual layers are more important for determining stability of Bragg stacks under intense laser irradiation. This is an important result, as it shows that it is beneficial to forego the final thermal annealing step often employed when fabricating Bragg stacks, leading to a decrease in overall energy cost and an increase in throughput for the synthesis of Bragg-type optical components such as dielectric mirrors, filters, and Fabry-Perot microcavities.

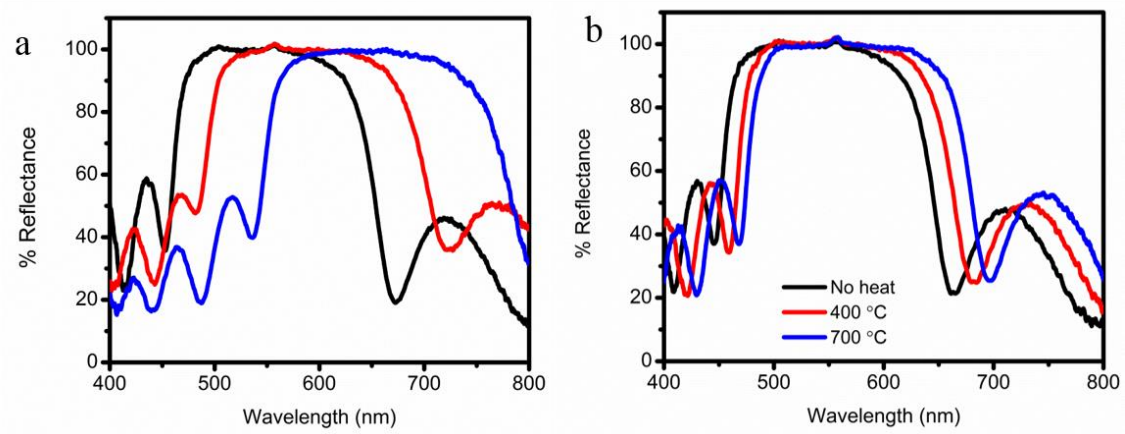

Figure 3.1 Reflection spectra of Bragg stacks with increasing titania layer thickness before (a) and after (b) undergoing annealing at room temperature, 400 °C, and 700 °C.

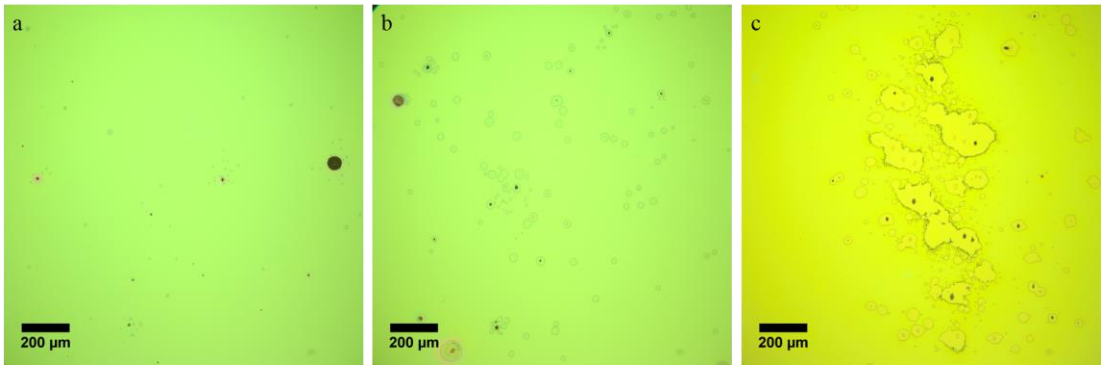

Figure 3.2 Optical micrographs of Bragg stacks as fabricated (a) and annealed at 400 °C (b) and 700 °C (c) after being subjected to 50 shots.

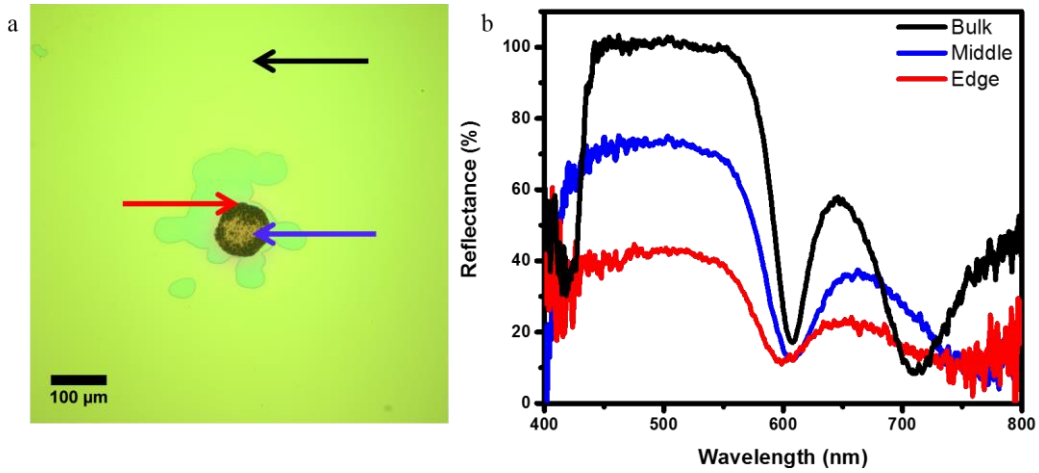

Figure 3.3 Optical micrograph of a damage spot (a) and the reflection spectra (b) corresponding to areas overlapping undamaged spots (black), the center of the damage spot (blue), and the edge of the damage spot (red).

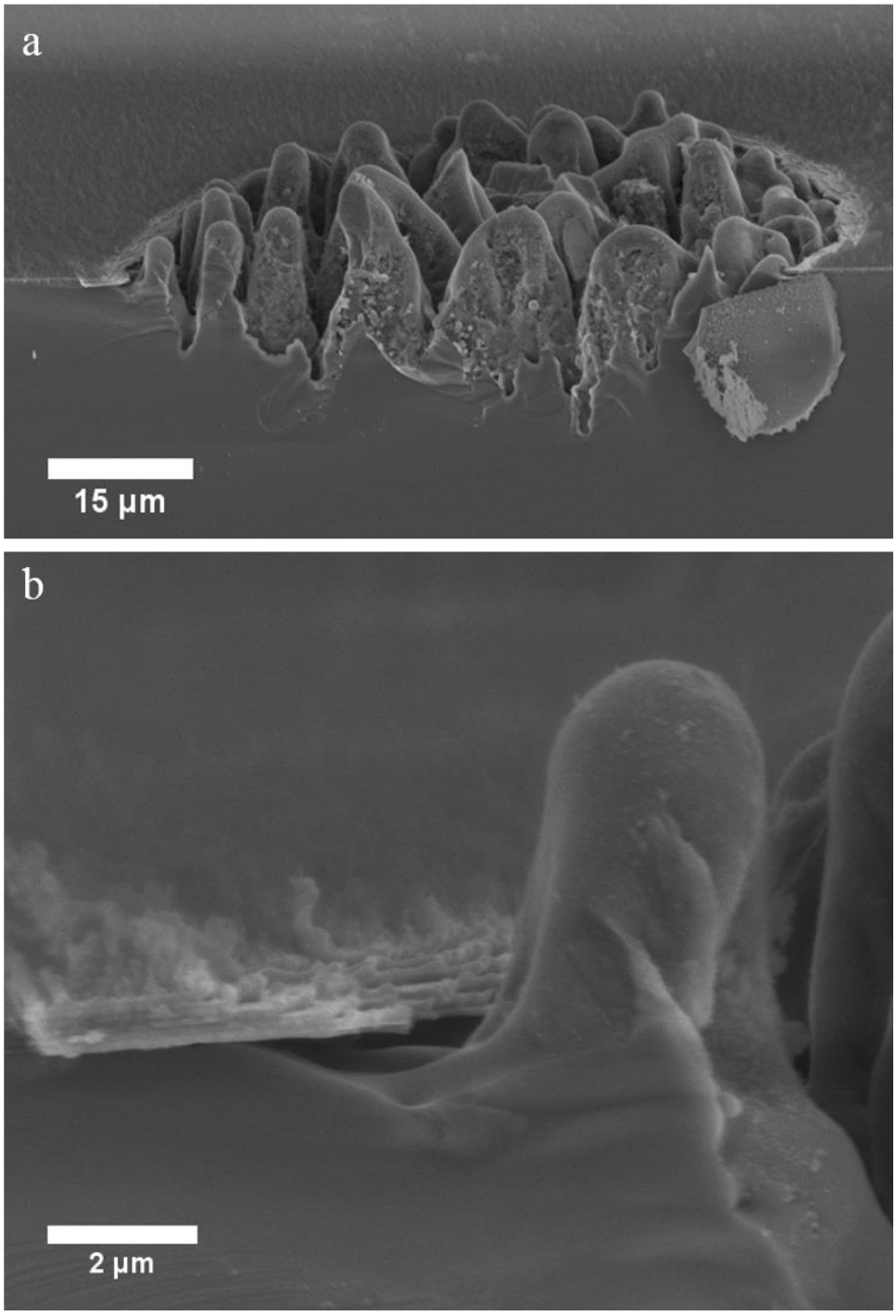

Figure 3.4 Cross-section SEM image of damage to exposed substrate (a) and close-up of the left edge of the damage spot (b).

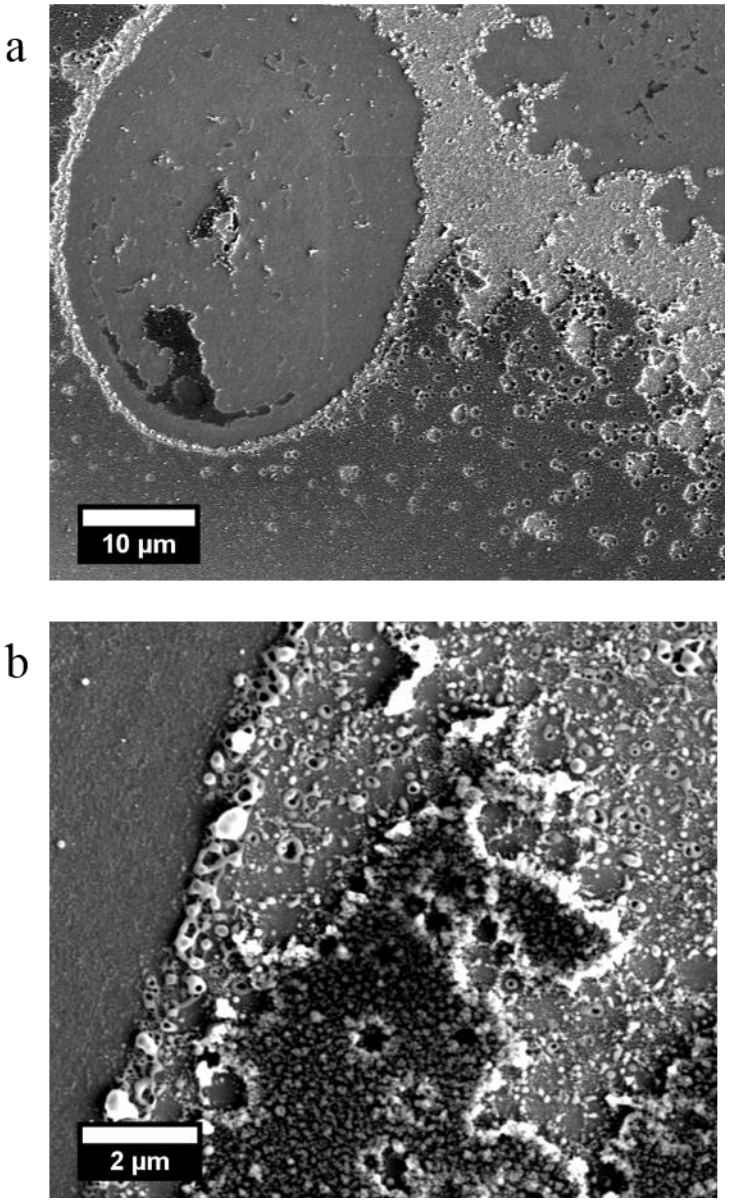

Figure 3.5 Top-down SEM images of plasma scalding morphologies. A larger flat-bottom pit is seen in (a) and the zoomed-in image (b) shows the bubbling effects at the edge of the damage spot.

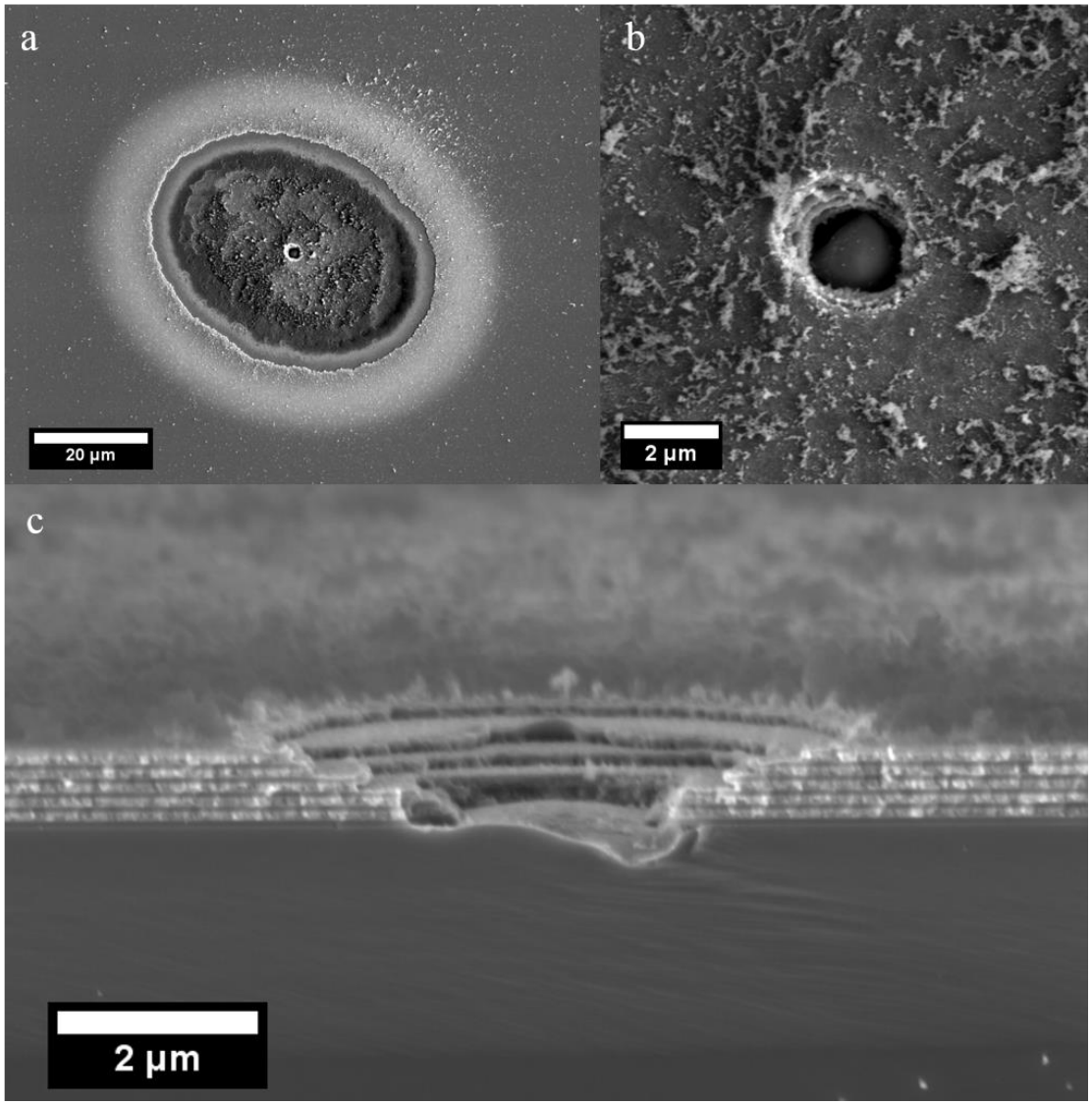

Figure 3.6 SEM images of ejection pit damage morphologies. (a) Top-down image showing an ejection pit within a plasma scald. (b) Close-up image of the ejection pit that appears to extend to the substrate (note the ridges along the inside from the individual layers that comprise the stack). (c) Cross-section image of an ejection pit and the immediately surrounding collateral damage.

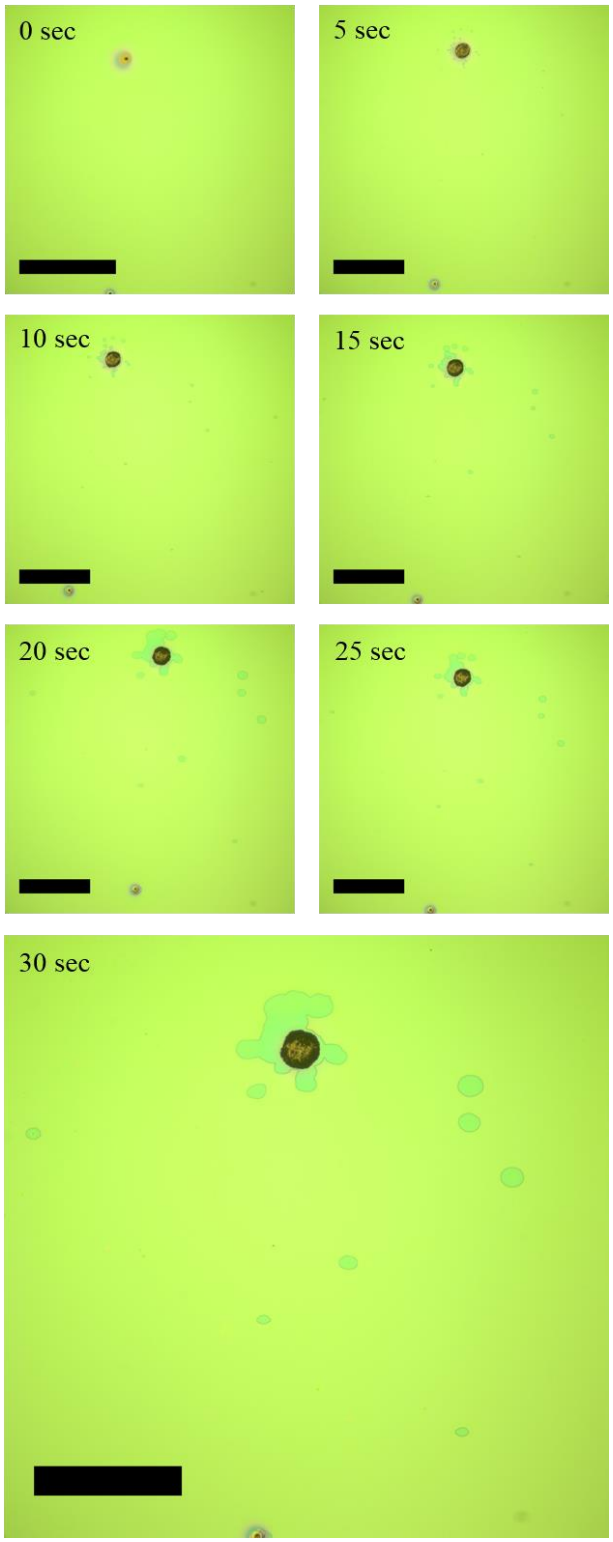

Figure 3.7 Optical micrographs showing evolution of laser-induced damage of non-annealed Bragg stack in 5 second intervals for total of 30 seconds. Scale bars are equal to 0.5 mm.

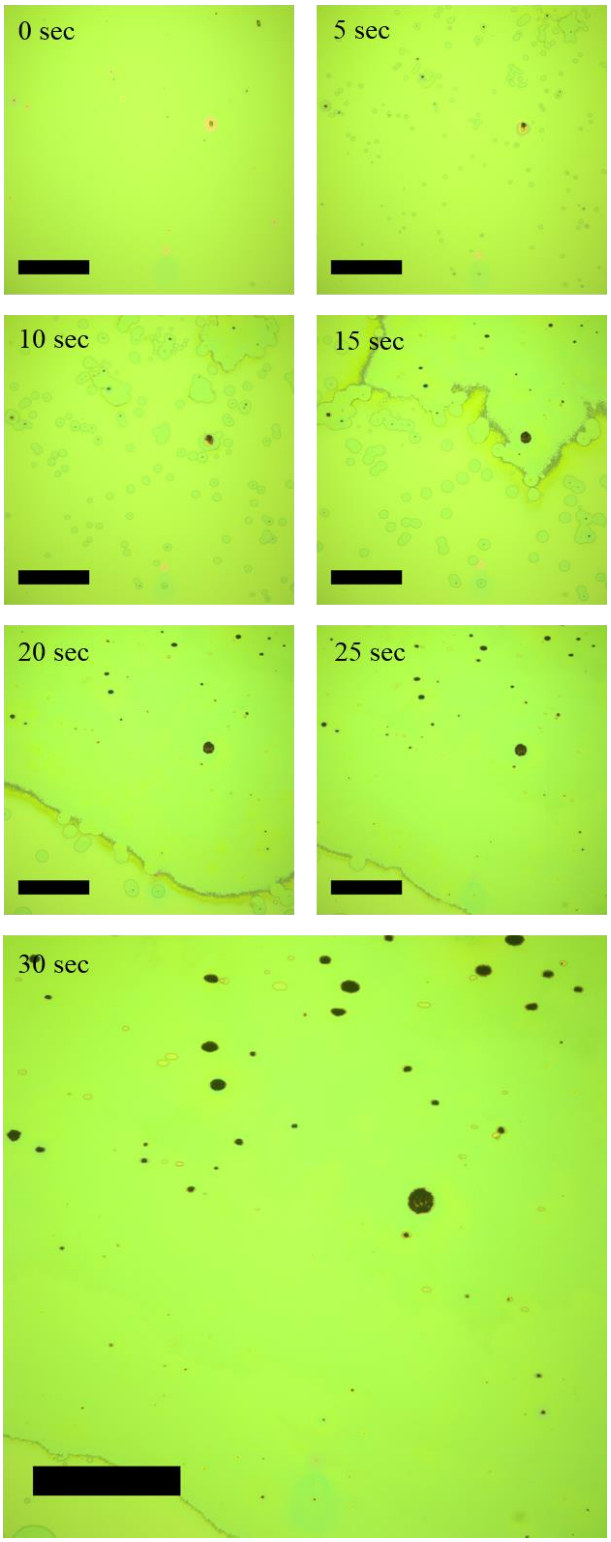

Figure 3.8 Optical micrographs showing evolution of laser-induced damage in 5 second intervals for a total of 30 seconds of Bragg stack annealed at 400 °C. Scale bars are equal to 0.5 mm.

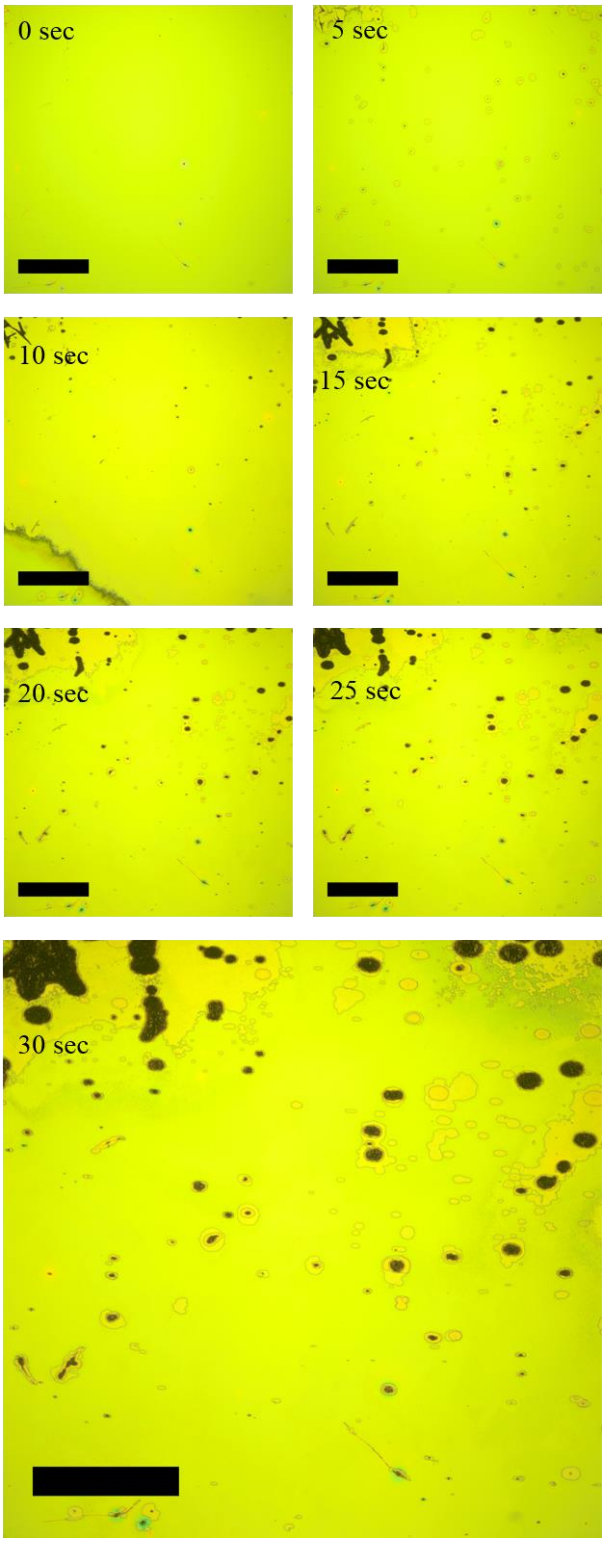

Figure 3.9 Optical micrographs showing evolution of laser-induced damage in 5 second intervals for a total of 30 seconds of Bragg stack annealed at 700 °C. Scale bars are equal to 0.5 mm.

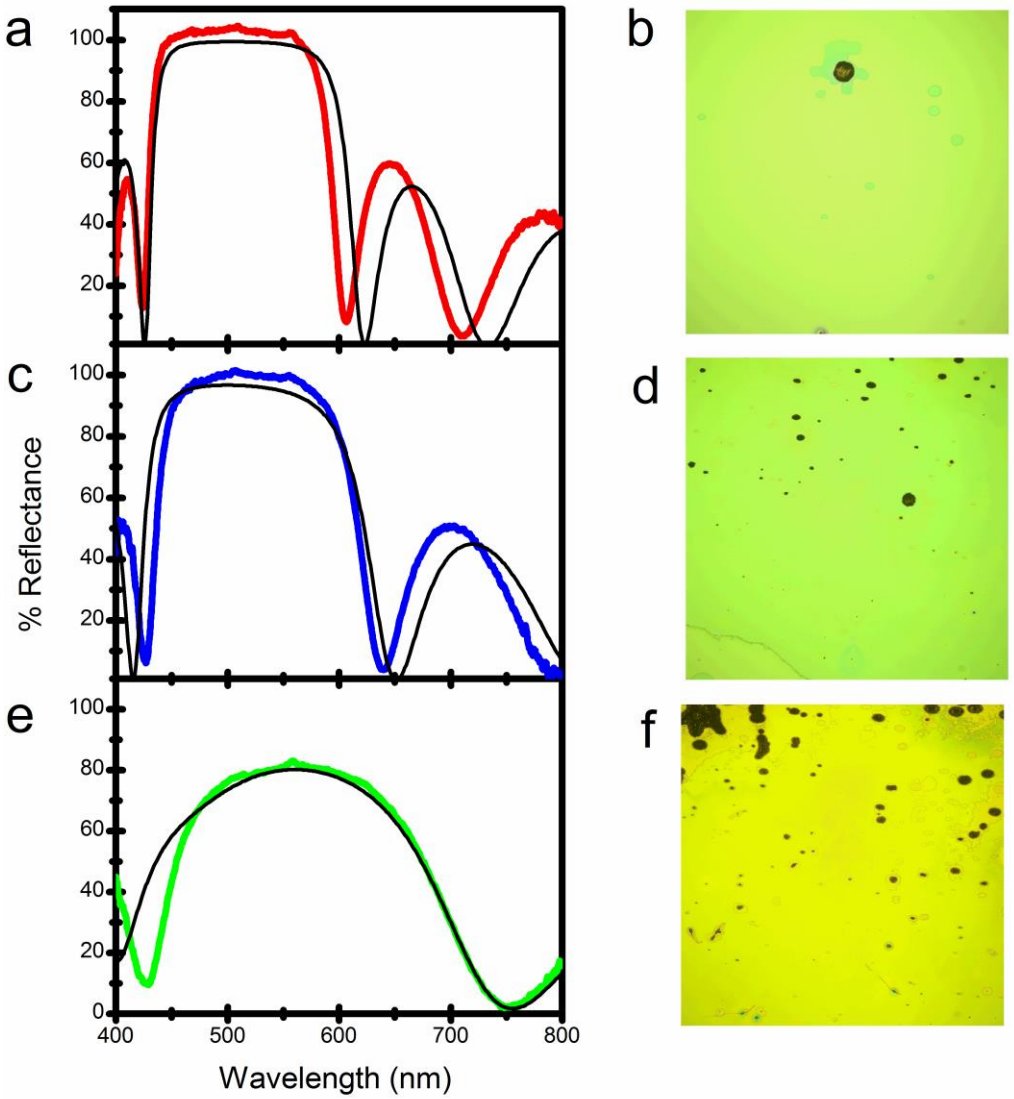

Figure 3.10 Optical reflection spectra (left) and corresponding optical micrographs (right) of annealed and non-annealed 12-layer Bragg stacks. Samples that were not annealed (a,b), annealed at 400 °C (c,d), and annealed at 700 °C (e,f) were exposed to high-power laser pulses at a wavelength of 532 nm (0.13 GW/cm^2 per pulse, with 10 Hz repetition rate) for 30 seconds. Calculated optical reflection spectra are given as black lines.

References

(1) Karaman, M.; Kooi, S. E.; Gleason, K. K. *Chemistry of Materials* **2008**, *20*, 2262.

(2) Kobler, J.; Lotsch, B. V.; Ozin, G. A.; Bein, T. *ACS Nano* **2009**, *3*, 1669.

(3) Kohoutek, T.; Orava, J.; Wagner, T.; Hrdlicka, M.; Vlcek, M.; Frumar, M. *J. Phys. Chem. Solids* **2008**, *69*, 2070.

(4) Pavlichenko, I.; Exner, A. T.; Guehl, M.; Lugli, P.; Scarpa, G.; Lotsch, B. V. *The Journal of Physical Chemistry C* **2011**, *116*, 298.

(5) Rabaste, S.; Bellessa, J.; Brioude, A.; Bovier, C.; Plenet, J. C.; Brenier, R.; Marty, O.; Mugnier, J.; Dumas, J. *Thin Solid Films* **2002**, *416*, 242.

(6) Kaiser, N.; Pulker, H. K. *Optical Interference Coatings*; Springer Berlin Heidelberg, 2010.

(7) Wood, R. M. *Laser-Induced Damage of Optical Materials*; CRC Press, 2003.

(8) Jee, Y.; Becker, M. F.; Walser, R. M. *J. Opt. Soc. Am. B: Opt. Phys.* **1988**, *5*, 648.

(9) Natoli, J.-Y.; Gallais, L.; Akhouayri, H.; Amra, C. *Appl. Opt.* **2002**, *41*, 3156.

(10) Stuart, B. C.; Feit, M. D.; Herman, S.; Rubenchik, A. M.; Shore, B. W.; Perry, M. D. *Phys. Rev. B: Condens. Matter* **1996**, *53*, 1749.

(11) Stuart, B. C.; Feit, M. D.; Rubenchik, A. M.; Shore, B. W.; Perry, M. D. *Phys. Rev. Lett.* **1995**, *74*, 2248.

(12) Manenkov, A. A. *Proc. SPIE* **2013**, *8786*, 87861I/1.

(13) Papernov, S.; Schmid, A. W. *Proc. SPIE* **2008**, *7132*, 71321J/1.

(14) Yu, J.; Xiang, X.; He, S.; Yuan, X.; Zheng, W.; Lu, H.; Zu, X. *Adv. Condens. Matter Phys.* **2014**, 364627/1.

(15) Candel, J. J.; Jimenez, J. A.; Franconetti, P.; Amigo, V. *J. Mater. Process. Technol* **2014**, *214*, 2325.

(16) Li, Z.; Wang, X.; Shen, Z.; Lu, J.; Ni, X. *Appl. Opt.* **2015**, *54*, 378.

(17) Louchev, O. A.; Hatano, H.; Saito, N.; Wada, S.; Kitamura, K. *J. Appl. Phys. (Melville, NY, U. S.)* **2013**, *114*, 203101/1.

(18) Ma, B.; Ma, H.; Jiao, H.; Cheng, X.; Wang, Z. *Opt. Laser Technol.* **2014**, *57*, 136.

(19) Mann, G.; Jurke, M.; Zoheidi, M.; Krueger, J. *Appl. Surf. Sci.* **2012**, *258*, 9153.

(20) Mikami, K.; Motokoshi, S.; Fujita, M.; Jitsuno, T.; Tanaka, K. A. *Proc. SPIE* **2011**, *8190*, 81900A/1.

(21) Wagner, F. R.; Gouldieff, C.; Natoli, J.-Y.; Commandre, M. *Thin Solid Films* **2015**, Ahead of Print.

(22) Zhang, C.; Liao, W.; Zhang, L.; Ye, Y.; Chen, J.; Wang, H.; Luan, X.; Yuan, X. *Adv. Condens. Matter Phys.* **2014**, 638045/1.

(23) Yablonovitch, E. *Sci Am* **2001**, *285*, 47.

(24) Bloembergen, N. *Appl. Opt.* **1973**, *12*, 661.

(25) Liu, X.; Zhao, Y. a.; Li, D.; Hu, G.; Gao, Y.; Fan, Z.; Shao, J. *Appl. Opt.* **2011**, *50*, 4226.

(26) Genin, F. Y.; Stolz, C. J. *Proc. SPIE-Int. Soc. Opt. Eng.* **1996**, *2870*, 439.

(27) Liu, X.; Li, D.; Zhao, Y. a.; Li, X.; Shao, J. *Appl. Surf. Sci.* **2010**, *256*, 3783.

(28) Stolz, C. J.; Genin, F. Y.; Reitter, T. A.; Molau, N.; Bevis, R. P.; Von Gunten, M. K.; Smith, D. J.; Anzellotti, J. F. *Proc. SPIE-Int. Soc. Opt. Eng.* **1997**, *2966*, 265.

(29) Stolz, C. J.; Genin, F. Y. *Springer Ser. Opt. Sci.* **2003**, *88*, 309.

(30) Fedorov, A.; De Hosson, J. T. M. *J. Appl. Phys.* **2005**, *97*, 123510/1.

(31) Fedorov, A. V.; van Tijum, R.; Vellinga, W. P.; De Hosson, J. T. M. *Prog. Org. Coat.* **2007**, *58*, 180.

(32) Kmetec, B.; Kovacic, D.; Mozina, J.; Podobnik, B. *Appl. Surf. Sci.* **2009**, *255*, 8598.

(33) McDonald, J. P.; Thouless, M. D.; Yalisove, S. M. *J. Mater. Res.* **2010**, *25*, 1087.

(34) Larouche, S.; Martinu, L. *Appl. Opt.* **2008**, *47*, C219.

CHAPTER 4

ADDITIVE-FREE SOL-GEL SYNTHESIS OF FERRITE AND YTTRIUM IRON GARNET FILMS

Introduction

An interesting class of magnetic oxide materials are the ferrites. These are typically defined as mixed metal oxides with Fe^{3+} as the main component[1]. Ferrites are employed in many applications due to, among other things, their chemical stability and magneto-optical properties[2-5]. Some applications include magnetic imaging pigments, microwave devices[6-7], memory storage[8-9], and sensors[10-12].

Ferrites are unique in that they combine the electrically insulating properties of antiferromagnetic compounds and the magnetic properties of ferromagnetic metals[13-14]. The magnetic properties of ferrites arise from the unequal composition of magnetic ions between the two sublattices. These differences may be due to the occupation of interstitial sites by unequal populations of ions with the same spin, ions with different spins, or both. Each sublattice exhibits inter-sublattice coupling which, due to the oxide nature of the material, is usually antiparallel and occurs via a superexchange mechanism through the oxygen anion. The overall magnetic behavior, however, is due to the difference in magnitudes between the two sublattices.

Ferrites can be found in spinel, garnet, and magnetoplumbite (hexagonal)

crystalstructures[1,15]. The spinel ferrites consist of the formula MFe_2O_4 where iron is present in the trivalent state and M is any number of divalent cations. The most well-known example is magnetite, where M is Fe^{2+}. The spinel unit cell consists of eight formula units. The 32 oxygen atoms in the unit cell are arranged in a face centered cubic lattice while the 8 divalent and 16 Fe^{3+} ions are distributed across two sublattices with either tetrahedral (A site) or octahedral (B site) coordination geometries (**Figure 4.1**). The distribution of ions across these two sites determine whether the spinel is considered normal or inverse. Normal spinels have the trivalent iron filling ½ of the B sites and the divalent ion filling $^1/_8$ of the A sites, while inverse spinels have the trivalent iron filling $^1/_8$ of the A sites and the divalent ion filling ¼ of each the A sites and B sites. Spinels with cation distributions falling between these ratios are simply referred to as mixed spinels.

The iron garnets consist of the formula $M_3Fe_5O_{12}$ where again iron is in the trivalent state and M corresponds to a different trivalent metal ion. The most common examples of this type include yttrium iron garnet (YIG) and the rare earth garnets. The unit cell for the garnets also consists of 8 formula units with 16 octahedral, 24 tetrahedral, and 24 dodecahedral interstitial sites. For YIG, the Fe^{3+} ions are distributed across the octahedral and tetrahedral sites in a 2 : 3 ratio and the Y^{3+} ions are found in the dodecahedral sites. In this case, the net magnetic moment stems from the uneven distribution of Fe^{3+} ions between the octahedral and tetrahedral sublattices.

Several physical deposition methods for forming ferrite thin films exist, including chemical vapor deposition[16-17], molecular beam epitaxy[3,18], and pulsed laser deposition[16-17,19-20]. However, these require extreme synthetic atmospheres (e.g. high vacuum, high-heat, etc.), are cumbersome, and expensive. Sol-gel processing, on the other hand, is

amenable to very mild synthetic conditions, requires less-sophisticated equipment, is fast, and is a more cost-effective alternative.

Some existing strategies for preparing precursor solutions for sol-gel deposition of iron oxide-based films include the use of iron alkoxide precursors[21], epoxide-catalysis of aqueous metal salts[22], and the addition of chelating and polymerization agents such as citric acid and ethylene glycol[9,23-27]. While these techniques have been shown to form films with useful applications, they are not without drawbacks. Alkoxide precursors are air-sensitive compounds and require refluxing in an inert atmosphere, while the epoxide-approach relies on a complicated, non-generalizable reaction scheme. The combustion of organic components within a film fabricated with chelating and polymerizing agents can degrade the integrity of the film during thermal annealing processes required to induce crystallization.

The technique presented in this chapter offers a much simpler reaction scheme that minimizes the number of reactants and utilizes favorable experimental conditions to prepare precursor solutions for depositing a variety of iron-based magnetic oxide materials. It relies on careful tuning of the reactant concentrations to control the hydrolysis and condensation of iron salts to synthesize a homogeneous iron oxide sol. Additional organic components are avoided, therefore increasing the homogeneity and mechanical stability of the obtained films. Deposition of high-quality films was achieved by the 4-step process presented in Chapter 2 followed by a thermal annealing period. The technique will be demonstrated first for the fabrication of α-Fe_2O_3 and then expanded by adding secondary ions to the precursor solution, allowing for the deposition of mixed-metal oxide films including yttrium iron garnet (YIG), cobalt ferrite ($CoFe_2O_4$), and nickel ferrite ($NiFe_2O_4$).

The microstructure of the films is characterized by X-ray diffraction (XRD), thickness is determined by scanning electron microscopy (SEM) analysis, composition is confirmed by X-ray photoelectron spectroscopy (XPS), and the magnetic properties determined by vibrating sample magnetometry (VSM).

Materials and Methods

Materials

$Fe(NO_3)_3 \cdot 9H_2O$ (≥99.999 %), $Co(NO_3)_2 \cdot 6H_2O$ (99.999 %), $Ni(NO_3)_2 \cdot 6H_2O$ (99.999 %), and $FeCl_2 \cdot 4H_2O$ (≥99.0 %) were purchased from Sigma Aldrich. $Y(NO_3)_3 \cdot 6H_2O$ (99.999 %) and $MnCl_2 \cdot 4H_2O$ (99.995 %) were purchased from Strem. Solutions were prepared using absolute ethanol and ultrapure water with a resistance of 18 MΩ. Quartz slides were purchased from Chemglass and silicon wafers purchased from University Wafer.

Solution Preparation

Iron oxide films were prepared from a solution containing a 1 : 4 : 0.33 molar ratio of Fe^{3+} : H_2O : HCl. The components were added to a straight-walled scintillation vial containing a magnetic stir bar and stirred on a 50 °C hot plate for approximately 30 minutes until the solution turned a translucent red color. The solution was then removed from the hot plate and stirred without heat until cooled to room temperature before dip-coating.

Yttrium iron garnet (YIG) films were prepared from a solution containing the same Fe^{3+} : H_2O : 6M HCl ratio above and a 3:5 Y^{3+} : Fe^{3+} ratio necessary to achieve the stoichiometric ratio $Y_3Fe_5O_{12}$. Single phase films were achieved by first dissolving

$Y(NO_3)_3 \cdot 6H_2O$ in the appropriate amount of ethanol and 6M HCl prior to adding the Fe^{3+} and H_2O and following the same stirring / heating protocol as for the iron oxide solutions.

Cobalt and nickel ferrite films were prepared by dissolving cobalt or nickel salts with iron to give a 1:2 M^{2+} : Fe^{3+} ratio for stoichiometric MFe_2O_4 in ethanol prior to adding the corresponding amount of Fe^{3+}, H_2O, and 6 M HCl. The same stirring / heating procedure for iron oxide solutions was applied.

Film Deposition / Annealing

Films were deposited on silicon or quartz substrates after cleaning with isopropanol and blowing dry with a stream of air. Substrates were suspended vertically by a pair of locking forceps, lowered into the prepared solution, and withdrawn at a constant speed of 12.6 cm/min. Upon withdrawal, the newly-formed film was placed in front of a stream of hot air supplied by an industrial strength hot air gun. The film was then placed onto a block of aluminum inside a pre-heated muffle furnace set to 450 °C for 5 seconds and then immediately placed onto a second block of aluminum kept at room temperature. For multilayer films, this procedure was repeated for each desired layer. After the last deposition cycle, the entire film was annealed in a furnace to induce crystallization.

X-Ray Diffraction

Phase characterization was performed using a Bruker D8 diffractometer using Cu Kα(1.54 Å) radiation. Scherrer analysis was performed to qualitatively compare average crystallite sizes within the same sample set. A value of 0.9 was used as the Scherrer constant.

Scanning Electron Microscopy

SEM analysis was performed using a FEI NovaNano 630 microscope. Due to the insulating nature of the films, a thin layer of gold was sputtered onto the samples when necessary due reduce charging artifacts. Thickness measurements were performed by depositing 5-, 10-, and 15-layer films onto silicon substrates. After annealing, the substrates were split perpendicular to the deposited film and mounted onto a vertical sample holder. Cross-section images were collected and the film thickness measured multiple times per image at various locations throughout the width of the film.

X-Ray Photoelectron Spectroscopy

XPS spectra were recorded with a Kratos Axis Ultra DLD spectrometer equipped with a monochromatic Al Kα source and calibrated using the C 1s peak. Fits obtained using the CasaXPS software were obtained using parameters from the literature and compared to known compounds[28-29].

Vibrating Sample Magnetometry

Magnetic hysteresis loops were obtained using a MicroSense EZ7 magnetometer. Quartz substrates were cut prior to deposition to a width compatible with the spacing between the magnetic poles. In-plane measurements were recorded at room temperature in transverse geometry.

Results and Discussion

Sol-gel Chemistry of Aqueous Metal Salts

Many transition metal ions readily undergo hydrolysis in aqueous solutions. The first step is coordination of water molecules to the metal ion, forming an aquo complex. This coordination occurs through charge transfer from the oxygen atom, thus increasing the acidity of the water molecule which promotes dissociation of a proton. This yields the second product, a hydroxo complex. The last step is dissociation of the remaining proton, leading to the formation of an oxo complex.

Each of these ligands alters the reactivity of the complex. For example, the water ligand of the aquo complex is an excellent leaving group and more labile, opening the possibility for ligand substitution reactions. The oxo ligand, on the other hand, is a very poor leaving group but a good nucleophile, thus favoring nucleophilic substitution reactions. The hydroxo ligand is both a good nucleophile and a stable leaving group and is therefore capable of undergoing both ligand and nucleophilic substitution reactions. Therefore, a higher concentration of hydroxo complexes allows for a higher degree of reactivity and more diverse reaction pathways to occur.

Polymer and particle growth occurs through the formation of hydroxy or oxo bridges as the result of olation or oxolation reactions, respectively. Both of these reactions occur through a two-step nucleophilic substitution if both complexes involved are coordinatively saturated, requiring the presence of both a good nucleophile and a sufficiently-stable leaving group. Therefore, olation and oxolation ligands are much more likely to occur when complexes with hydroxo ligands are present in solution.

While the solution equilibria in water are well understood, water is a poor choice

of solvent for film formation due to its low rate of evaporation, high surface tension, etc. Volatile solvents such as ethanol are much more amenable to the film formation process. Since ethanol is polar, weakly coordinating, and promotes hydrolysis of iron salts, it is reasonable to expect that equilibria similar to that of aqueous solutions will occur[30]. Therefore, the strategy employed in this study was to develop an ethanol-based system to allow film formation using a rapid dip-coating process by: 1) Optimizing the solution parameters to slow the kinetics of iron oxide particle growth in ethanol 2) Determining the conditions necessary for deposition of high-quality films 3) Incorporating secondary metal ions to form mixed metal oxide films 4) Annealing the films to induce crystallinity and obtain magnetic properties.

Optimizing the Solution Parameters

Film formation occurs during the dip-coating process when colloidal particles aggregate and condense together as the substrate is withdrawn from the solution. The sizes and shapes of these particles have a large effect on the porosity, coverage, and surface properties of the film. Therefore, larger and more polydisperse particles can lead to an increased surface roughness which is detrimental to the overall quality of the film. Because of this, fabricating films from colloidal solutions requires precise tuning of the reactant conditions to control the size and homogeneity of the particles.

Growth of iron oxide particles proceeds by the mechanism described above. As the reaction proceeds, protons are released resulting in a decrease in solution pH. The presence of base in the reaction solution neutralizes the released protons, pushing the reaction to the right and favoring particle growth and precipitation. Acid, on the other hand, pushes the

reaction to the left and inhibits particle growth, instead favoring lower-weight particles and clusters. In fact, under very acidic conditions, particle growth is completely inhibited and the solution will remain stable to precipitation indefinitely whereas sufficiently basic solutions will yield precipitate immediately. Given this very broad range of reactivity, finding the proper conditions to control the kinetics is a difficult task but paramount to achieving the optimal particle distribution for film formation.

In order to achieve this, a systematic investigation of the behavior of Fe^{3+} in ethanol solution was first carried out by preparing a series of solutions containing incremental volumes of 1M HCl. Samples consisting of 0.1 g $FeCl_3$•$6H_2O$ and 2 mL ethanol (1 : 90 Fe^{3+} : EtOH) were prepared and 100-500 μL of 1M HCl were added and stirred until mixed. The samples were then left at room temperature and observed over the course of several days. Solutions with higher concentrations of acid were bright yellow in color and translucent while solutions with lower acid concentrations were more orange. Over time, all solutions that initially appeared orange in color turned opaque and then proceeded to precipitate (**Figure 4.2**) while those that were initially yellow remained that way, indicating that hydrolysis did not proceed at any appreciable rate. A ratio of 1 : 0.33 Fe^{3+} : HCl prevented precipitation for at least a day and therefore was chosen as an acceptable concentration for future studies as this would give more than a sufficient time window for dip-coating.

Determining the Conditions Necessary for Deposition of High-quality Films

The same 4-step deposition procedure described in Chapter 2 was used here for film formation. In short, this consists of withdrawing either a silicon or quartz substrate at

a constant rate of 12.6 cm/min, rapidly evaporating the solvent with a stream of hot air supplied by an industrial-strength hot air blower, placing the substrate onto a block of aluminum metal inside a pre-heated muffle furnace at 450 °C for 5 seconds, and then shock-cooling the substrate by placing it immediately onto a second block of aluminum kept at room temperature.

Films prepared from the 1 : 0.33 Fe^{3+}: HCl solutions described above consistently featured a high number of large pinhole effects and in some cases incomplete coverage of the substrate, suggesting that the equilibrium was too far to either the right or left to allow condensation to occur to a sufficient extent. To determine whether the solution equilibria had shifted too far to the right, films were prepared from solutions containing the same volume but higher concentrations of HCl. These films indeed contained fewer pinhole defects, but instead featured large areas of inhomogeneity and surface roughness that exhibited greater effect with higher acid concentration. This suggested that the initial 1 : 0.33 Fe^{3+} solution ratio was not yielding a sufficient number of hydroxy complexes and further condensation would be necessary.

Two strategies could be used to increase the amount of condensation: 1) decreasing the amount of acid and 2) increasing the amount of water. However, changing the acid concentration has a double effect on the reaction because Cl^- ligands can compete with water molecules for coordination to the iron. Therefore, the second strategy was chosen and additional aliquots of water were added during future solution preparation. A 1 : 4 : 0.33 molar ratio of Fe^{3+} : H_2O : HCl was found to consistently yield high-quality films (see, for example, YIG films in **Figure 4.3**).

High-quality films were also prepared using $Fe(NO_3)_3$-$9H_2O$ following the same

procedure. However, nitrate solutions consistently yielded films that visibly appeared more homogeneous. This is probably due a combination of the slightly higher mean electronegativity of the nitrate ion (2.76 vs 2.40)[31], which promotes hydrolysis over ionic dissociation, as wells as a slightly higher number of associated water molecules from the crystal lattice of the metal salt and the higher lability of the nitrate ion.

Various solution heating periods were also performed in order to decrease the aging time necessary to reach adequate hydrolysis. Some techniques in the literature utilize temperatures as high as 90 °C in 2-methoxyethanol[11]. For the preparation reported here, this temperature was too high and caused solutions to quickly change from translucent to opaque orange, indicating a rapid increase in particle size. At lower temperatures, solutions tended to transform from translucent orange to translucent red prior to becoming opaque. This color change is consistent with the evolution of red polymeric cations of iron[32-33]. Stirring solutions for approximately 30 minutes on a hot plate set to 50 °C and cooling to room temperature before dip-coating was found to significantly reduce the aging time necessary for film formation.

Incorporating Secondary Metal Ions to Form Mixed Metal Oxide Films

Not only were the concentration, precursor ratios, and aging time crucial for successful film deposition, but the order in which the components were added had a substantial effect on the phase purity of mixed oxide films after the final annealing period as discussed below. Because the kinetics of iron hydrolysis are fast, single-phase mixed-oxide films could only be obtained by dissolving the secondary metal salt in solution prior to the addition of iron salt. This ensured that the secondary ions were fully interspersed

throughout the solution prior to iron nucleation and growth, leading to homogeneous single-phase films. However, the solubility of the salts must be taken into account and therefore each material required slightly different solution preparations.

In order to achieve homogeneous YIG films by this route, the yttrium salt must first be dissolved in the appropriate amount of ethanol and HCl prior to adding the iron salt and water. Simply adding the yttrium and iron salts to the reaction vial concurrently did not yield single-phase films. This is due to the difference in yttrium solubility between acidic and neutral pH. If the acid was not added within a sufficient amount of time, iron particle growth would begin before the ytrrium salt was fully dissolved, thus leading to mixed-phase films. This was especially important when stirring the solution at elevated temperature.

For cobalt ferrite, single-phase films were obtained by first dissolving the cobalt salt in ethanol, stirring until fully dissolved, and then adding the iron salt, water, and acid. Nickel ferrite films were obtained by simply adding the nickel salt at the beginning of the solution preparation. Single-phase films were also obtained following all procedures described above for iron oxide.

Successful film synthesis via this technique is dependent on the stability of the metal ion in acidic solution. Trivalent iron and yttrium, as well as divalent cobalt and nickel, are all stable to oxidation. Divalent iron and manganese, on the other hand, readily oxidize and therefore prohibit the synthesis of films requiring these metals in the +2 oxidation state. Attempts to synthesize magnetite (Fe_3O_4) by various procedures always yielded Fe_2O_3 as a result of Fe^{2+} oxidizing to Fe^{3+} and attempts to synthesize manganese ferrite yielded $MnFeO_3$ as a result of Mn^{2+} oxidizing to Mn^{3+}.

Annealing the Films to Induce Crystallinity and Obtain Magnetic Properties

One major advantage of the sol-gel process is the speed with which materials can be synthesized. However, most sol-gel processes yield amorphous products which require an additional high-temperature annealing period to induce crystallinity in the final material. This is a nontrivial task, as it introduces another source of potential stress that can induce cracking, flaking, and delamination of the film[34-36]. In addition, as was seen in Chapter 3, even when these effects are not present, thermal annealing can still increase the overall stress of a film that can lead to severe damage when exposed to sources of high energy. However, using the shock-cooling technique after the annealing period again led to high-quality crack-free films. Unlike in the case of titania in Chapter 2, none of the films in this chapter exhibited reflection peaks in XRD patterns prior to undergoing the thermal annealing process. The full results of this study are discussed in detail below for each type of film and the results for YIG, $CoFe_2O_4$, and $NiFe_2O_4$ are summarized in **Table 4.1**.

Hematite

Films prepared from solutions containing only iron salts started to yield peaks in the XRD pattern after annealing at 500 °C (**Figure 4.4a**). Peak positions were consistent with those of rhombohedral α-Fe_2O_3 (JCPD card 87-116). The large number of reflections present indicates that the film has a high degree of crystallinity. These results suggest that solution conditions favor oxolation reactions over olation, since the formation of hydroxy bridges should lead to the formation of goethite FeO(OH) rather than Fe_2O_3. The presence of the highest-intensity reflection at 33.3 degrees in other XRD patterns was used to determine the phase purity of those films (i.e. presence of unwanted Fe_2O_3).

Hematite typically exhibits weak ferromagnetic behavior[37-39]. However, hysteresis curves of single-layer hematite films prepared by this method resembled a diamagnetic response (**Figure 4.4b**). This is likely due to the diamagnetic response of the comparatively much thicker quartz substrate masking the weak response of the film.

Magnetite

Synthesis of magnetite (Fe_3O_4) films by this technique were not successful. All attempts to add stoichiometric amounts of Fe^{2+} salt to the precursor solution always yielded pure Fe_2O_3 as the final crystalline product, suggesting that Fe^{2+} had been oxidized to Fe^{3+}. To investigate the possibility that thermal annealing in air was the cause of this oxidation, samples were also annealed in a reducing H_2 / argon atmosphere. However, these films also crystallized as Fe_2O_3, confirming that Fe^{2+} oxidation occurred in solution, thus preventing the synthesis of magnetite.

Yttrium Iron Garnet

The formation of YIG films required an annealing temperature of 800 °C before exhibiting XRD peaks (**Figure 4.5a**), indicating a higher energy requirement necessary for crystallization compared to Fe_2O_3. The number of observed reflections corresponded well to reference patterns (JCPDS 77-1998), indicating a high degree of crystallinity. Analysis of films annealed at 900 °C did not indicate the presence of additional reflections. Scherrer analysis of the main 420 reflection using a constant value of 0.9 showed the average crystallite size increased from 50.9 nm to 59.7 nm, consistent with the observed peak narrowing in the XRD pattern.

Single-phase YIG films annealed at 700 °C, despite showing no discernible XRD reflections, exhibited a very minor amount of hysteresis behavior (**Figure 4.5b**), with a coercivity of 0.003 Oe and squareness value of 0.29, suggesting the presence of very small areas of local ordering dispersed throughout the film. Increasing the annealing temperature to 800 °C resulted in a large increase in both coercivity and squareness with values of 43.3 Oe and 0.55, respectively, consistent with the emergence of reflection peaks in the XRD pattern. Annealing at 900 °C led to minor increases of average crystallite size, coercivity, and squareness, with values of 59.7 nm, 46.2 Oe, and 0.63, respectively, indicating that the increased temperature did not lead to significant improvements in the crystallinity.

Cobalt Ferrite

For single-phase $CoFe_2O_4$, films annealed at 700, 800, and 900 °C all exhibited reflections consistent with cubic $CoFe_2O_4$ (JCPDS 22-1086), indicating a very high degree of crystallinity (**Figure 4.6a**). Scherrer analysis of the major 311 peak indicated only a slight increase in average crystallite size from 58.3, 60.0, and 61.1 nm at these temperatures, respectively. Films annealed at 700 and 800 °C exhibited a drop in coercivity from 3130 Oe to 2580 Oe, respectively, indicating lower anisotropy (**Figure 4.6b**). Annealing at 900 °C did not lead to further improvement.

Nickel Ferrite

Single-phase nickel ferrite films showed excellent agreement with the XRD reflection peak positions of cubic $NiFe_2O_4$ (JCPDS 74-2081). These peaks were all present in films annealed at 700, 800, and 900 °C (**Figure 4.7a**). Scherrer analysis yielded average

crystallite sizes of 51.2, 58.2, and 59.8 nm at these temperatures, respectively. The hysteresis parameters showed a similar trend to the cobalt ferrite samples, with a coercivity of 265 Oe when annealed at 700 °C dropping to 226 Oe and 224 Oe when annealed at 800 °C and 900 °C, respectively (**Figure 4.7b**). Squareness values were all very similar, with values of 0.35, 0.34, and 0.29 with increasing temperature.

Manganese Ferrite

Attempts to synthesize manganese ferrite usually resulted in some oxidation of Mn^{2+} to Mn^{3+}, with the exact crystalline material depending on the manner of solution preparation. From solutions prepared by dissolving the iron and manganese salts separately, various combinations of peaks corresponding to $MnFe_2O_4$, Mn_2O_3, and Fe_2O_3 were obtained, depending on the ramp rate. Films prepared by first dissolving the manganese salt in ethanol prior to the addition of iron and acid, however, exhibited XRD reflections (**Figure 4.8**) consistent with single-phase $MnFeO_3$ (JCPDS 76-0076).

Film Thickness

To demonstrate the thickness tunability of this technique, YIG films of 5, 10, and 15 layers were prepared from solutions consisting of various ethanol : Fe^{3+} ratios and the corresponding ratio of Fe^{3+} : H_2O : HCl. The thicknesses of these films were then measured from cross-sectional SEM images and plotted against the number of deposited layers in **Figure 4.9**. The number of layers chosen for this study were chosen to facilitate the determination of thickness as measurements of single layer films can be difficult to ascertain due to charging effects.

Least-squares analysis of these plots yielded linear curves, which allows for accurate determination of solution concentration and number of layers necessary to prepare a film of desired thickness. The slope values of the 50 : 1 and 75 : 1 curves differ from the 100 : 1, 150 : 1, and 300 : 1 curves due to method of preparation. The former were prepared by stirring the precursor solution at 50 °C for 30 minutes while the latter were prepared by stirring at room temperature overnight. This illustrates the impact that the kinetics of hydrolysis and condensation have on the thickness of the deposited film. From the chosen range of concentrations, films ranging from approximately 15 nm (single-layer 300 : 1) to 820 nm (15 layers 50 : 1) in thickness were obtained. This is an impressive range and demonstrates the power and tunability of our sol-gel technique.

Composition

X-ray photoelectron spectrometry was performed on the final single-phase films to confirm the oxidation states and atomic ratios of metal ions (**Figure 4.10**) after fitting the obtained spectra to deconvolution parameters from the literature[40-41]. The $2p_{3/2}$ peak was used to analyze the iron, nickel, and cobalt content and the $3d_{5/2}$ peak was used to analyze yttrium content. The peak shape for iron matched very closely with trivalent iron in all samples. YIG films exhibited yttrium $3d_{5/2}$ peaks matching Y^{3+} while cobalt and nickel ferrite films both exhibited $2p_{3/2}$ line shapes corresponding to the divalent state.

While precise quantification is difficult to achieve since the intensity of peaks depends on a number of factors including source electron emission, detector sensitivity, and background treatment, good agreement was obtained between percentage atomic concentrations and expected stoichiometric ratios. Shirley backgrounds were subtracted

from all spectra prior to analysis. A ratio of 0.82 Y^{3+} / Fe^{3+} was obtained from YIG, which is slightly higher than the expected 0.67 stoichiometric ratio. Ratios of M^{2+} / Fe^{3+} equal to 0.58 and 0.56 were obtained for $CoFe_2O_4$ and $NiFe_2O_4$, respectively. These values are in excellent agreement with the expected ratio of 0.5.

In addition, the manganese-iron films were examined. The $2p_{3/2}$ shape corresponded to the trivalent state, further suggesting the formation of $MnFeO_3$.Manganese films yielded a Mn^{3+} / Fe^{3+} ratio of 0.51, which is in excellent agreement with the 1 : 2 ratio used to prepare the precursor solution but at odds with the 1 : 1 ratio expected from the observed $MnFeO_3$ XRD results. It is possible that the excess manganese ions are interspersed amorphously throughout the film.

Conclusions

A new additive-free sol-gel technique featuring simple reactants and reactant conditions was developed to deposit various iron-based oxide films were on silicon and quartz substrates. The reactant concentrations were carefully tuned to control the hydrolysis and condensation rates of iron salts to synthesize a homogeneous iron oxide sol. Single-phase films including α-Fe_2O_3, YIG, $CoFe_2O_4$, and $NiFe_2O_4$ were obtained after thermal annealing and exhibited a high level of crystallinity by XRD analysis. The magnetic properties were investigated by VSM and showed very good magnetic ordering, as well as a range of properties obtained by simply replacing metal salts during solution preparation. The thickness of the deposited films was tuned by adjusting the precursor and reactant concentrations as well as repeating the deposition cycle using the same solution. Composition analysis was performed by XPS and confirmed the oxidation states and ratios

of ions present in the films were in excellent agreement with the expected results. These high-quality films show promise for use in applications such as components in microwave devices and magnonic crystal materials.

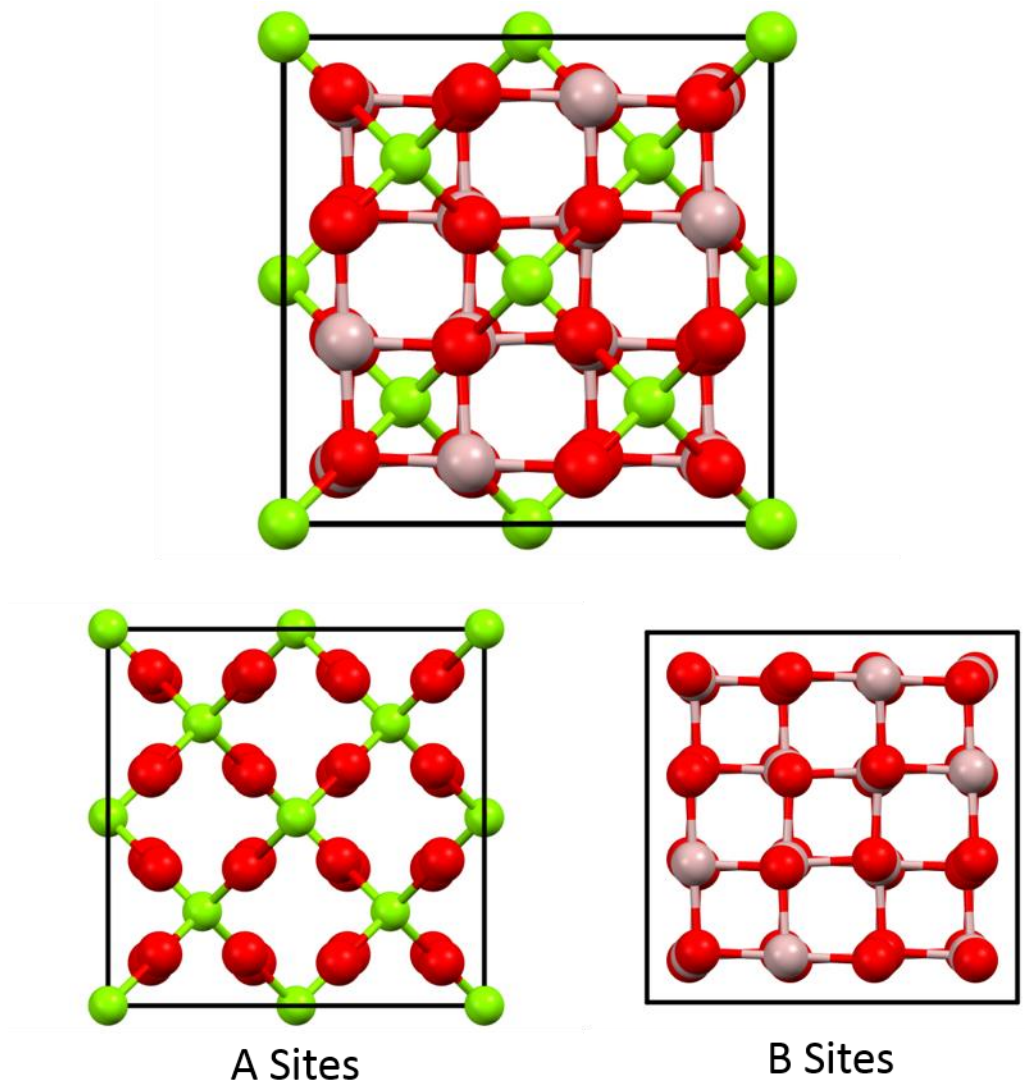

Figure 4.1 General picture of the spinel structure, illustrating the interspersed sublattices. Oxygen atoms are red, interstitial A sites with tetrahedral geometry are green, and interstitial B sites with octahedral geometry are grey.

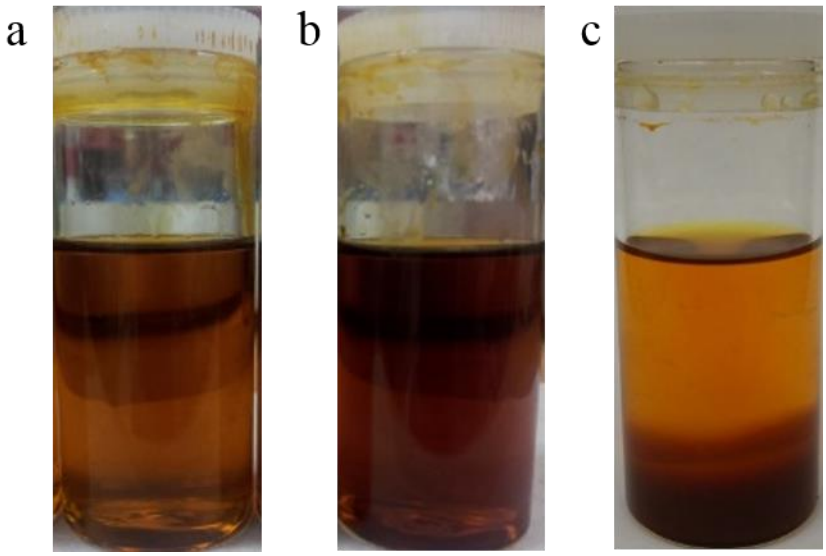

Figure 4.2 Photographs of iron oxide solutions in ethanol showing the three stages of particle growth. Hydrolyzed ions appear bright orange and translucent (a), medium-weight polymeric species appear darker red (b), and large-weight species produce a gelatinous, dark orange precipitate (c).

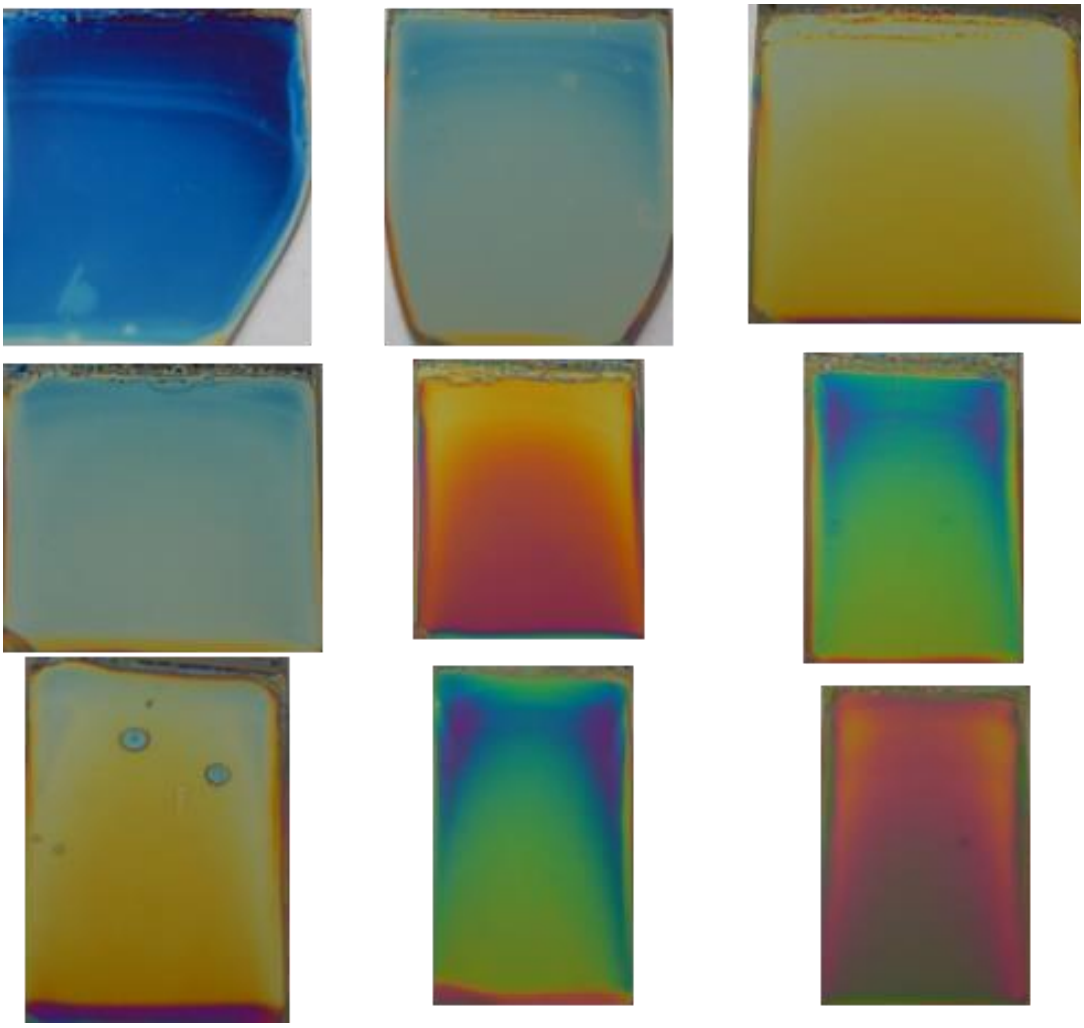

Figure 4.3 Photographs of yttrium iron garnet (YIG) films prepared from various concentrations of precursor solution and deposited on approximately one-inch-wide silicon substrates.

Table 4.1 Average crystalite sizes from Scherrer analysis of major reflection peaks in XRD patterns, magnetic coercivities (H_c), and squareness values (S) of the associated hysteresis curves for samples annealed at various temperatures. Errors for crystallite size pertain to the peak fitting.

	Annealing Temp. (° C)	Avg. Crystallite Size (nm)	H_c (Oe)	S
YIG	700	-	0.003	0.3
	800	50.9 ± 0.3	43	0.55
	900	59.7 ± 0.2	46	0.63
$CoFe_2O_4$	700	58.3 ± 0.6	3130	0.83
	800	60.0 ± 0.4	2580	0.72
	900	61.1 ± 0.5	2530	0.76
$NiFe_2O_4$	700	51.2 ± 0.5	265	0.35
	800	58.2 ± 0.4	226	0.34
	900	59.8 ± 0.5	224	0.29

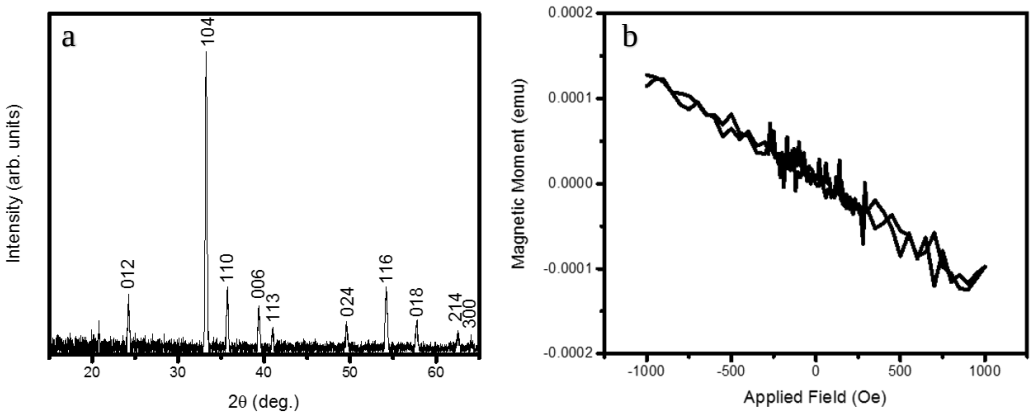

Figure 4.4 X-ray diffraction pattern (a) and hysteresis curve (b) for α-Fe_2O_3 (hematite) annealed at 500 °C. XRD pattern is referenced against JCPDS card 87-1166.

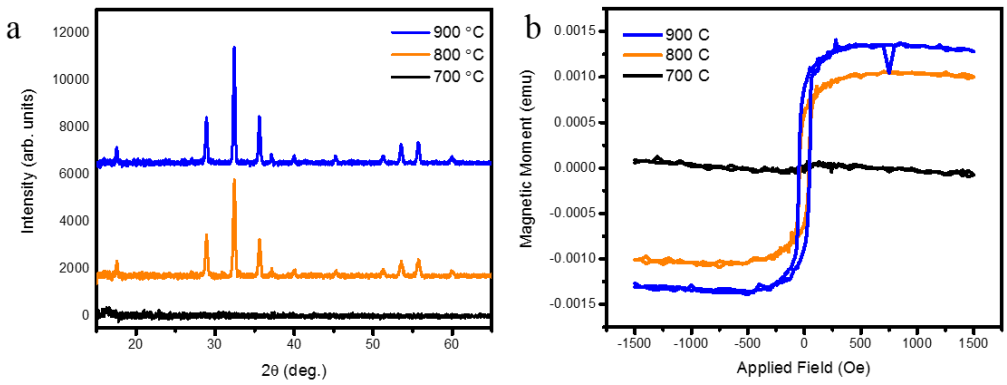

Figure 4.5 X-ray diffraction patterns (a) and hysteresis curves (b) for yttrium iron garnet (YIG) samples annealed at various temperatures. XRD pattern is referenced against JCPDS card 77-1998. Hysteresis curves were left un-normalized to illustrate the weak response of the sample annealed at 700 °C.

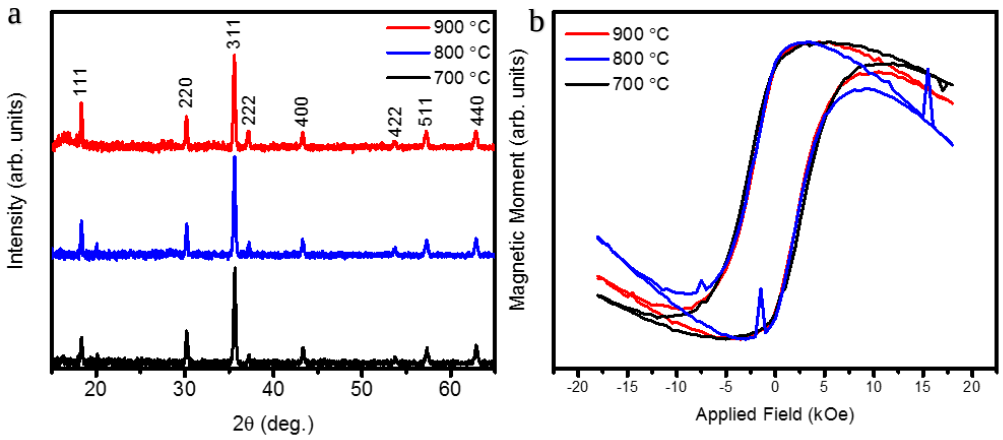

Figure 4.6 X-ray diffraction patterns (a) and normalized hysteresis curves (b) for cobalt ferrite ($CoFe_2O_4$) samples annealed at various temperatures. XRD pattern is referenced against JCPDS card 22-1086.

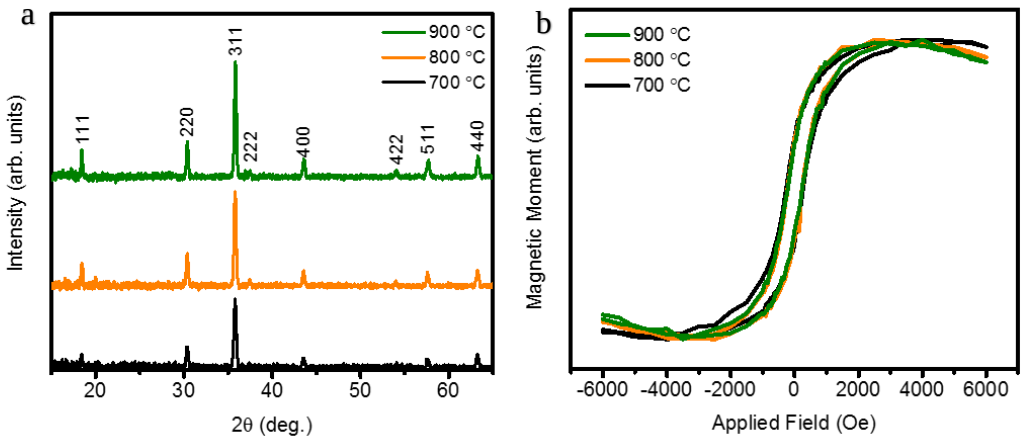

Figure 4.7 X-ray diffraction patterns (a) and normalized hysteresis curves (b) for nickel ferrite ($NiFe_2O_4$) samples annealed at various temperatures. XRD pattern is referenced against JCPDS card 74-2081.

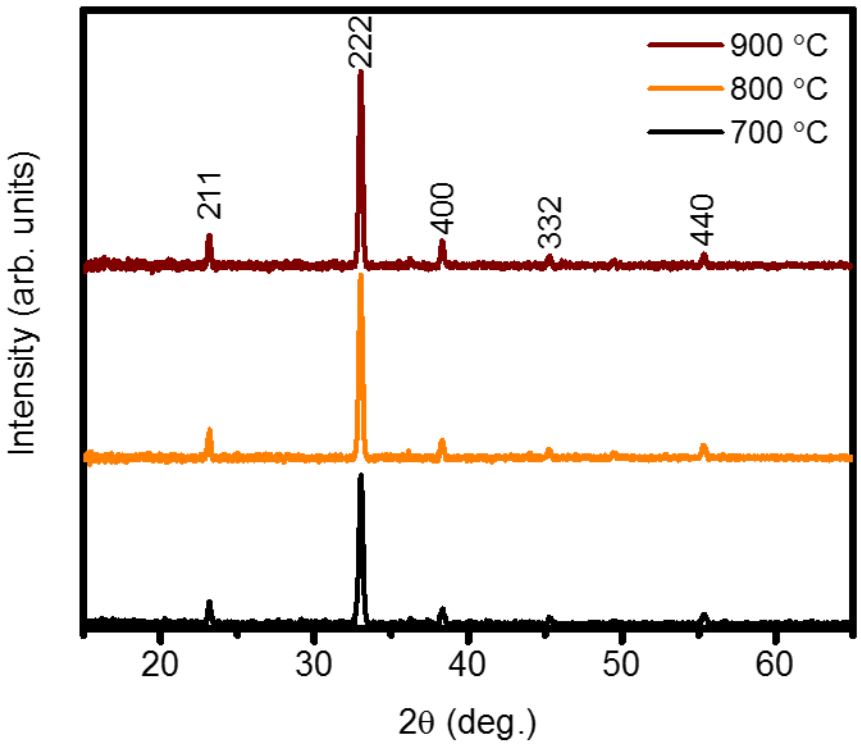

Figure 4.8 X-ray diffraction patterns for manganese-iron samples ferrite annealed at various temperatures. XRD pattern is referenced against JCPDS card 76-0076 for $MnFeO_3$.

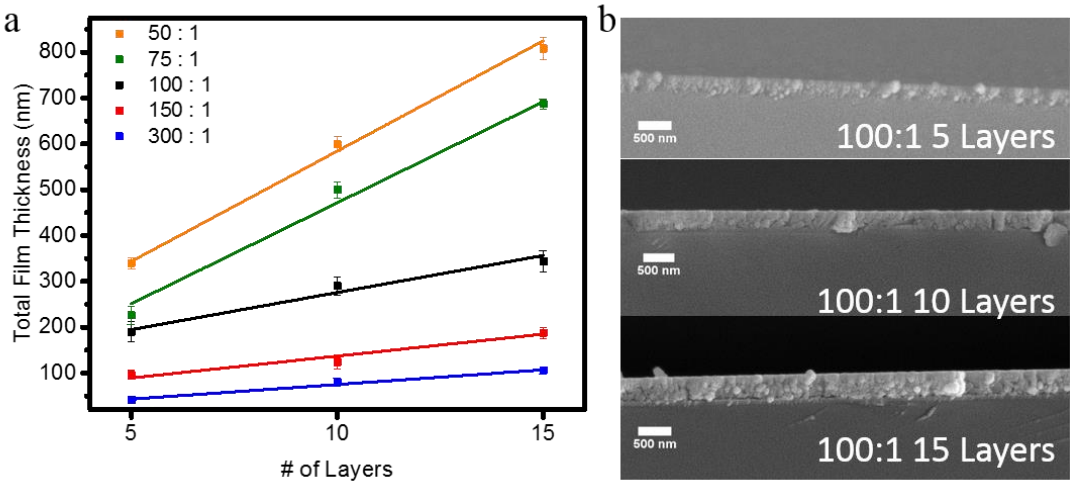

Figure 4.9 Thickness of films (a) prepared with varying concentrations of Fe^{3+} : Ethanol plotted against the number of layers deposited. Values were obtained from cross-section SEM images. Error bars correspond to the standard deviation of measurements made across the width of the sample. (b) Representative cross-section SEM images used to measure thickness.

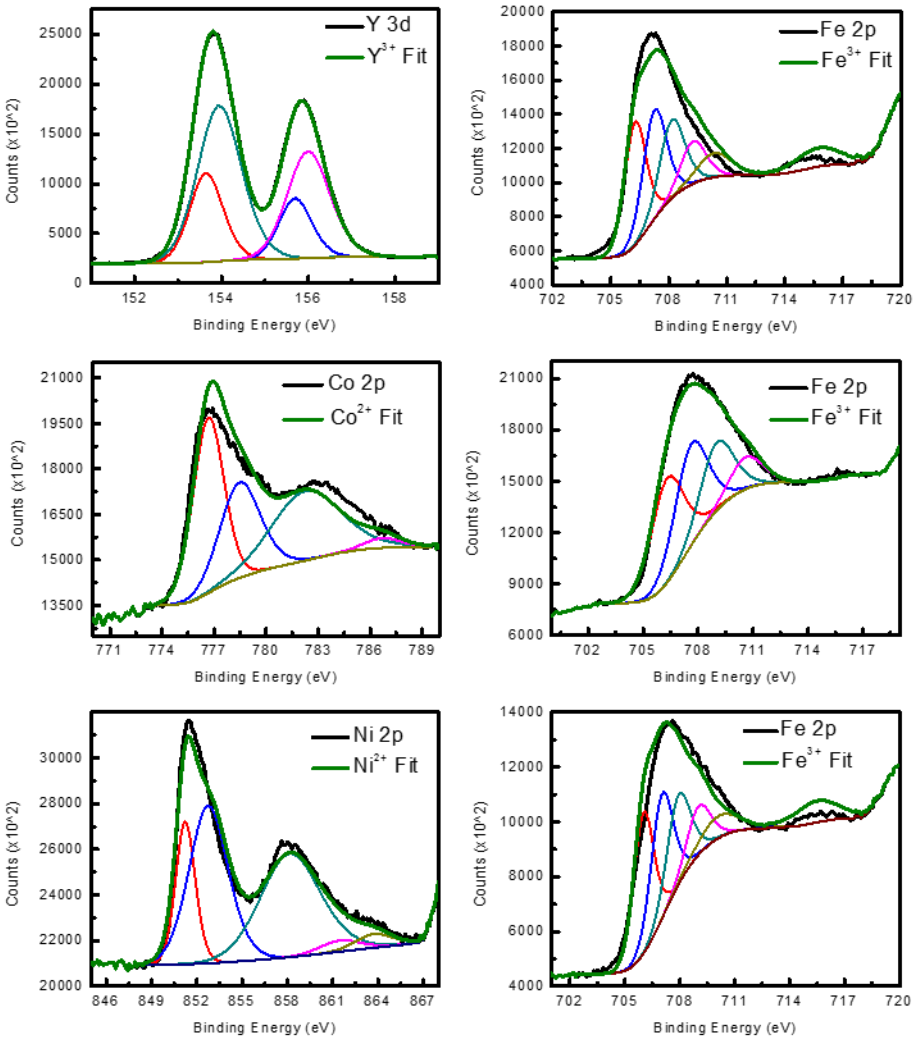

Figure 4.10 X-ray photoelectron spectra for the secondary ion (left) and the associated iron ion (right) for YIG (top), cobalt ferrite (middle), and nickel ferrite (bottom). Black curves are actual data and green curves are the fits corresponding to the multicolored deconvolution curves.

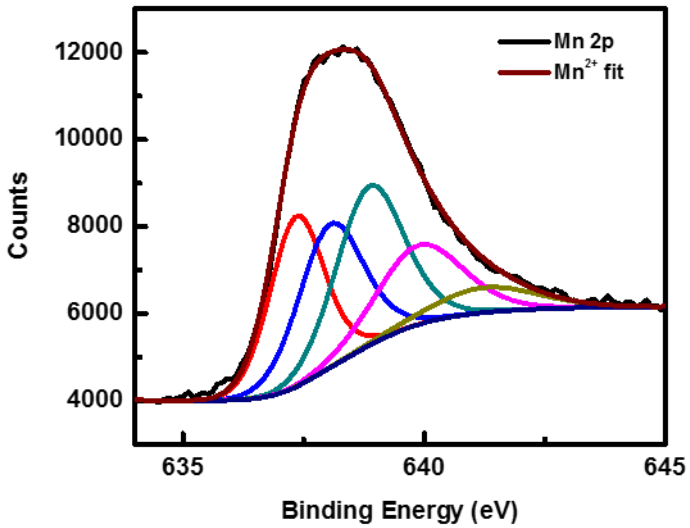

Figure 4.11 X-Ray photoelectron spectrum of manganese-iron sample exhibiting crystal structure corresponding to $MnFeO_3$. Black curve is the actual data and the brown curve is the fit corresponding to the multicolored deconvolution curves.

References

(1) Viswanathan, B.; Murthy, V. R. K. *Ferrite Materials: Science and Technology*; Narosa Publishing House, 1990.

(2) Fontijn, W. F. J.; van der Zaag, P. J.; Feiner, L. F.; Metselaar, R.; Devillers, M. A. C. *Journal of Applied Physics* **1999**, *85*, 5100.

(3) Himcinschi, C.; Vrejoiu, I.; Salvan, G.; Fronk, M.; Talkenberger, A.; Zahn, D. R. T.; Rafaja, D.; Kortus, J. *Journal of Applied Physics* **2013**, *113*, 084101.

(4) Tachiki, M. *Prog. Theor. Phys.* **1960**, *23*, 1055.

(5) Schnittger, S.; Jooss, C.; Sievers, S. *J. Phys.: Conf. Ser.* **2010**, *200*, No pp. given.

(6) Gupta, N.; Verma, A.; Kashyap, S. C.; Dube, D. C. *J. Magn. Magn. Mater.* **2007**, *308*, 137.

(7) Zaquine, I.; Benazizi, H.; Mage, J. C. *J. Appl. Phys.* **1988**, *64*, 5822.

(8) Matsumoto, M.; Morisako, A.; Takei, S. *J. Alloys Compd.* **2001**, *326*, 215.

(9) Cheng, F.; Peng, Z.; Liao, C.; Xu, Z.; Gao, S.; Yan, C.; Wang, D.; Wang, J. *Solid State Commun.* **1998**, *107*, 471.

(10) Sandu, I.; Presmanes, L.; Alphonse, P.; Tailhades, P. *Thin Solid Films* **2005**, *495*, 130.

(11) Tongpool, R.; Jindasuwan, S. *Sens. Actuators, B* **2005**, *106*, 523.

(12) Rao, P.; Godbole, R. V.; Phase, D. M.; Chikate, R. C.; Bhagwat, S. *Materials Chemistry and Physics* **2015**, *149–150*, 333.

(13) Snelling, E. C.; Giles, A. D. *Ferrites for Inductors and Transformers*; Research Studies Press, 1983.

(14) Goldman, A. *Modern Ferrite Technology*; Springer US, 2006.

(15) P., K. S. N. In *Ferromagnetic Materials*; Wohlfarth, E. P., Ed.; North-Holland Publishing Company, 1982; Vol. 3.

(16) Dhakal, T.; Mukherjee, D.; Hyde, R.; Mukherjee, P.; Phan, M. H.; Srikanth, H.; Witanachchi, S. *J. Appl. Phys.* **2010**, *107*, 053914/1.

(17) Yang, A.; Zuo, X.; Chen, L.; Chen, Z.; Vittoria, C.; Harris, V. G. *J. Appl. Phys.* **2005**, *97*, 10G107/1.

(18) Suzuki, Y. *Annu. Rev. Mater. Res.* **2001**, *31*, 265.

(19) Williams, C. M.; Chrisey, D. B.; Lubitz, P.; Grabowski, K. S.; Cotell, C. M. *J. Appl. Phys.* **1994**, *75*, 1676.

(20) Carosella, C. A.; Chrisey, D. B., 1994; p 509.

(21) Ryder, D. F., Jr.; Fenstermacher, J. H. *J. Am. Ceram. Soc.* **1990**, *73*, 282.

(22) Park, C.-d.; Walker, J.; Tannenbaum, R.; Stiegman, A. E.; Frydrych, J.; Machala, L. *ACS Appl. Mater. Interfaces* **2009**, *1*, 1843.

(23) Uekawa, N.; Kaneko, K. *J. Phys. Chem. B* **1998**, *102*, 8719.

(24) Baythoun, M. S. G.; Sale, F. R. *J. Mater. Sci.* **1982**, *17*, 2757.

(25) Tai, L. W.; Lessing, P. A. *J. Mater. Res.* **1992**, *7*, 511.

(26) Takahashi, N.; Kakuta, N.; Ueno, A.; Yamaguchi, K.; Fujii, T.; Mizushima, T.; Udagawa, Y. *J. Mater. Sci.* **1991**, *26*, 497.

(27) Naseri, M. G.; Saion, E. B.; Kamali, A. *ISRN Nanotechnol.* **2012**, 604241.

(28) McIntyre, N. S.; Zetaruk, D. G. *Anal. Chem.* **1977**, *49*, 1521.

(29) Biesinger, M. C.; Payne, B. P.; Grosvenor, A. P.; Lau, L. W. M.; Gerson, A. R.; Smart, R. S. C. *Appl. Surf. Sci.* **2011**, *257*, 2717.

(30) Niederberger, M. *Acc. Chem. Res.* **2007**, *40*, 793.

(31) Brinker, C. J.; Scherer, G. W. *Sol-gel science : The Physics and Chemistry of Sol-Gel Processing*; Academic Press, Inc. : San Diego, 1990.

(32) Flynn, C. M., Jr. *Chem. Rev.* **1984**, *84*, 31.

(33) Spiro, T. G.; Allerton, S. E.; Renner, J.; Terzis, A.; Bils, R.; Saltman, P. *J. Am. Chem. Soc.* **1966**, *88*, 2721.

(34) Cammarata, R. C. *Prog. Surf. Sci.* **1994**, *46*, 1.

(35) Kozuka, H.; Takenaka, S.; Tokita, H.; Hirano, T.; Higashi, Y.; Hamatani, T. *Journal of Sol-Gel Science and Technology* **2003**, *26*, 681.

(36) Spaepen, F. *Acta Materialia* **2000**, *48*, 31.

(37) Dou, Z.-F.; Wan, G.-P.; Bao, L.-F.; Cao, C.-Y. *J. Nanosci. Nanotechnol.* **2014**, *14*, 5587.

(38) Roeder, L.; Bender, P.; Tschoepe, A.; Birringer, R.; Schmidt, A. M. *J. Polym. Sci., Part B: Polym. Phys.* **2012**, *50*, 1772.

(39) Uribe, J. D.; Osorio, J.; Barrero, C. A.; Giratá, D.; Morales, A. L.; Hoffmann, A. *Microelectronics Journal* **2008**, *39*, 1391.

(40) Stuber, M.; Leiste, H.; Ulrich, S.; Holleck, H.; Schild, D. *Surf. Coat. Technol.* **2002**, *150*, 218.

(41) Zubillaga, O.; Cano, F. J.; Azkarate, I.; Molchan, I. S.; Thompson, G. E.; Cabral, A. M.; Morais, P. J. *Surf. Coat. Technol.* **2008**, *202*, 5936.

CHAPTER 5

OUTLOOK AND SUMMARY

Introduction

This dissertation has presented the scientific community with a simple, versatile technique for depositing high-quality dielectric films, Bragg stacks, and magnetic oxide films. It is quite remarkable that such mild synthetic conditions can be used to fabricate materials that will aid future research in areas such as spintronics and magnonics that have the potential to change technology as we know it.

Toward Magnonic Crystals

The results presented in this dissertation show excellent potential for the fabrication of various magnonic crystal architectures through the fabrication of either 1D multilayer films or 2D and 3D structures when combined with other fabrication techniques.

Preliminary results showing the feasibility of 1D MCs were obtained by fabricating single-component 1- and 2-layer films as well as composite bilayer films and comparing the hysteresis loops obtained by VSM. **Figure 5.1** shows the single-component hysteresis loops for 1- and 2-layer films of cobalt ferrite. In both cases, the shape and coercive field are very similar for both films, the only difference being the magnitude of the magnetic moment as a result of increased mass of the 2-layer film. This suggests that dip-coating the

substrate into the same solution twice yields a two-layer film that acts as a single, thicker film. As was seen in Chapter 4, this technique allows for a very wide range of thicknesses, resulting in an impressive degree of tunability that will yield corresponding magnetic properties.

Figure 5.2 shows the hysteresis loops obtained for bilayer composite films consisting of one layer each of YIG and cobalt ferrite. Here, it is quite obvious that each layer maintains its inherent magnetization properties and the overall shape of the curve is a summation of the contributions from each individual layer. Interestingly, the coercivities have each bilayer film are different, which may warrant future investigation.

These results suggest that 1) high-quality, homogeneous films may be obtained by dip-coating in the same solution more than once while maintaining similar magnetic properties, and 2) dip-coating in alternating solutions allows for the fabrication of layers with discrete magnetic properties, showing great promise for the fabrication of 1D magnonic crystals.

Other strategies for fabricating a magnonic crystal would necessitate the use of other structures and material syntheses. Specifically, dipcoating films of synthetic opal structures could lead to 3D inverse magnetic structures. Similar examples have been shown for electrodepositing metal films in the airspaces between the spheres[1]. Titania inverse structures can readily be made using this technique and a similar procedure of dip-coating opals into magnetic oxide solutions could very well could facilitate efforts to fabricating a 3D MC.

Synthesis of Other Ferrites

Outside of the divalent ions used to synthesize ferrite films in Chapter 4, other common ions found in spinel ferrites include divalent copper, cadmium, zinc, magnesium, and lithium[2-3]. While some of these ions are not paramagnetic and therefore cannot contribute to the magnetic moment of either sublattice, their inclusion can induce disproportionation between the iron ions and yield an overall net moment. Lithium is a monovalent ion and therefore can only replace one half of the stoichiometric equivalent divalent ions in order to remain charge neutral; the other half can be accounted for with excess iron or other trivalent ions. In addition, methods for stabilizing the divalent iron and manganese ions in solution could lead to the preparation of these films by the technique presented here. One such strategy would would be to adjust the pH level of the solution.

The synthesis of mixed ferrites also offers a means of tuning the magnetic properties. Synthesis of these types of films should be relatively simple and would involve changing the stoichiometric amount of ions added to the precursor solution.

Dissertation Summary

Chapter 1 presented a background discussion of all the topics necessary to understand the work presented in this dissertation, including thin films and physical deposition techniques, the underpinnings of sol-gel chemistry and thin film formation from a sol, the quantum and classical physics of 1D PCs, and the foundations of magnetism in magnetic oxide materials.

Chapter 2 presented an in-depth analysis of the 4-step sol-gel deposition process of thin films developed and perfected in the Bartl lab. High-quality dielectric thin films were

successfully deposited via a 4-step process consisting of 1) dip-coating 2) rapid solvent evaporation 3) brief thermal treatment and 4) shock-cooling. Each step of this process and its overall impact affecting the deposition of films was described in detail. Bragg stacks consisting of alternating silica and titania layers were prepared and the versatility of the process was exhibited by preparing samples with varying layer thickness, resulting in a series of samples with reflection bands spanning the entire visible range. Post-synthetic thermal annealing was found to increase the crystallinity of the titania films while resulting in a blue-shift of the main reflection peak. Results obtained from modeling the effects of increased refractive index contrast and decreased layer thickness on the reflection properties of the Bragg stacks suggest that this shift is primarily the result of titania layer shrinkage.

The photo-stability of these Bragg stacks was investigated in Chapter 3 by laser-induced damage threshold studies. Results obtained by optical microscopy, reflectance spectroscopy, and SEM imaging showed that Bragg stacks annealed at higher temperatures exhibit a decrease in damage threshold as a result of increased interlayer stress. These results suggest that interfacial properties rather than the quality of individual layers are more important for determining stability of Bragg stacks under intense laser irradiation. This is an important result, as it shows that it is beneficial to forego the final thermal annealing step often employed when fabricating Bragg stacks, which would lead to a decrease in overall energy cost and an increase in throughput for the synthesis of Bragg-type optical components such as dielectric mirrors, filters, and Fabry-Perot microcavities.

Chapter 4 introduced a new additive-free sol-gel technique featuring simple reactants and reactant conditions was developed to deposit various iron-based oxide films were on

silicon and quartz substrates. The reactant concentrations were carefully tuned to control the hydrolysis and condensation rates of iron salts to synthesize a homogeneous iron oxide sol. Single-phase films including α-Fe_2O_3, YIG, $CoFe_2O_4$, and $NiFe_2O_4$ were obtained after thermal annealing and exhibited a high level of crystallinity by XRD analysis. The magnetic properties were investigated by VSM and showed very good magnetic ordering, as well as a range of properties obtained by simply replacing metal salts during solution preparation. The thickness of the deposited films was tuned by adjusting the precursor and reactant concentrations as well as repeating the deposition cycle using the same solution. Composition analysis was performed by XPS and confirmed the oxidation states and ratios of ions present in the films were in excellent agreement with the expected results.

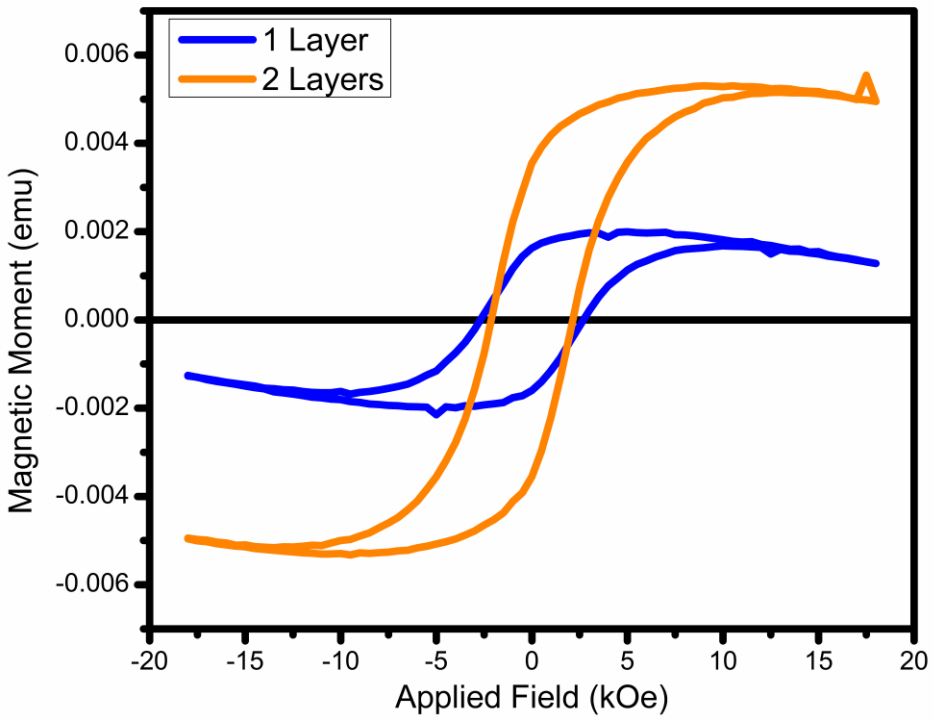

Figure 5.1 Hysteresis curves of films containing 1-layer and 2-layers of cobalt ferrite.

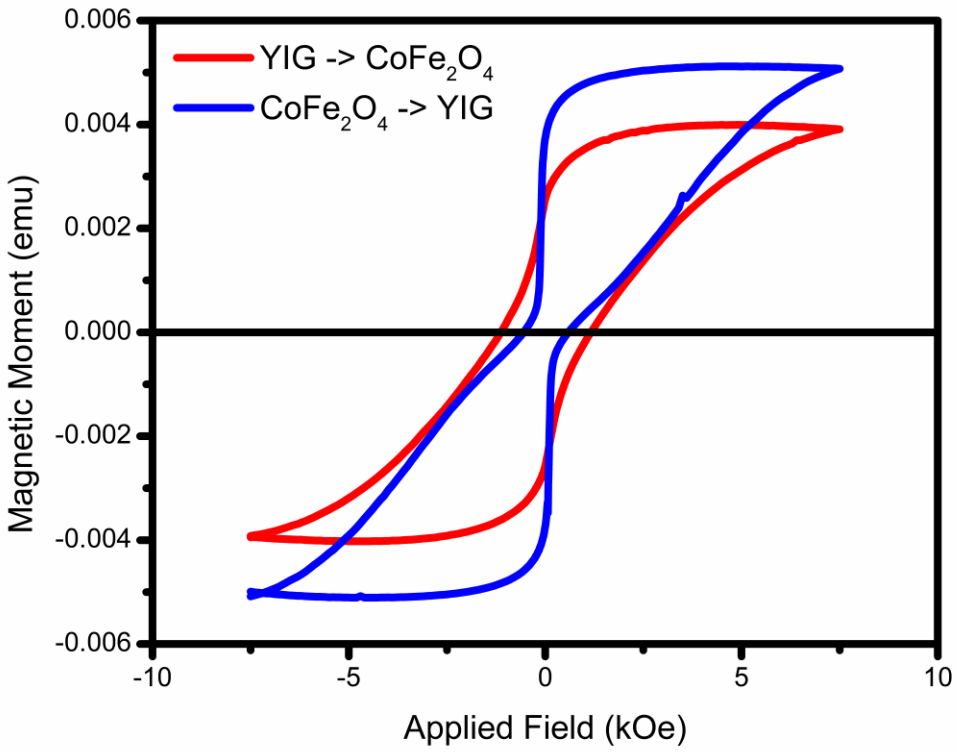

Figure 5.2 Hysteresis curves of films consisting of 1-layer each of YIG and cobalt ferrite. The red curve is for the case of cobalt ferrite deposited on top of YIG and the blue curve is for the opposite case.

References

(1) Hukic-Markosian, G.; Zhai, Y.; Montanari, D. E.; Ott, S.; Braun, A.; Sun, D.; Vardeny, Z. V.; Bartl, M. H. *J. Appl. Phys. (Melville, NY, U. S.)* **2014**, *116*, 013906/1.

(2) Goldman, A. *Modern Ferrite Technology*; Springer US, 2006.

(3) Viswanathan, B.; Murthy, V. R. K. *Ferrite Materials: Science and Technology*; Narosa Publishing House, 1990.